STUDIES ON Li^+ IONIC CONDUCTING SOLID ELECTROLYTE COMPOSED OF NASICON-TYPE STRUCTURE

1994

HIROMICHI AONO

STUDIES ON Li^+ IONIC CONDUCTING SOLID ELECTROLYTE COMPOSED OF NASICON-TYPE STRUCTURE

(NASICON型構造を有するリチウムイオン導電性固体電解質に関する研究)

1994

HIROMICHI AONO

Preface

The work described in this doctoral thesis was carried out under the guidance from Professor Dr. Gin-ya Adachi at Department of Applied Chemistry, Faculty of Engineering, Osaka University.

The object of this thesis is preparation of the high Li^+ ion conductive ceramic electrolytes. The excellent Li^+ conductive solid electrolytes were obtained as a result of this experiment. The author hopes that the materials obtained in this thesis would contribute to some applications.

Hiromichi Aono

January 1994

CONTENTS

Chapter 1

General Introduction

Solid electrolytes are ionic materials with a high ionic conductivity comparable to those of molten and aqueous electrolytes. The liquid electrolyte has various kind of carrier ions (cations and anions), since ions easily migrate in liquid. On the other hand, in general, a solid electrolyte has only one carrier ion because the other constituent elements are necessary to maintain the rigid skeleton. The ion migration in solid is a peculiar behavior and the solid electrolytes have unique crystal structures. Before the 1960's, only stabilized zirconia and α-AgI have been known to show high O^{2-} and Ag^{+} ionic conductivities, respectively.[1-5] In the stabilized cubic zirconia, the tetra-valent Zr sites in ZrO_2 are partially substituted for di- or tri-valent cations such as Ca(II) or Y(III) ion. This partial substitution makes oxygen vacancies produce in the cubic phase. The O^{2-} ions easily migrate in the oxygen vacancies and the conductivity at 1073 K is ca. $1x10^{-2}$ S$\cdot$cm^{-1}. Although β-type structure is stable for AgI at room temperature, the conductivity increases more than three orders of magnitude by the phase transition from β to α-type structure at 323 K. The high conductivity of α-AgI is obtained by the fact that two Ag^{+} ions are statistically distributed over 42 Ag^{+} vacant sites to occupy around I^{-} constituent ions per an unit cell. This α-form is a "liquid-like" solid. Reuter et al. reported in 1961 that Ag_3SI shows a high silver ionic conductivity of 10^{-2} S$\cdot$cm^{-1} even at room temperature.[6] Then, many

of high Ag^+ conducting materials based on AgI have been found.[7,8]

In the middle of the 1960's, β-alumina ($Na_2O \cdot 11Al_2O_3$) was prepared as a fast Na^+ ion conductor.[9,10] β-alumina has a layered structure and Na^+ ion migrates two dimensional Na^+ conductive planes between the Al_2O_3 spinel blocks. In 1977, Goodenough and Hong designed a three dimensional network structure which has a suitable tunnel size for Na^+ migration, and named the $Na_{1+x}Zr_2Si_xP_{3-x}O_{12}$ material as a Na$^+$ super ionic conductor (NASICON).[11,12] Since then, a lot of ionic conductors have been discovered and numerous applications have been found.

One of the representative applications is a gas sensor. The O_2 gas sensor using the stabilized zirconia has already been commercialized for the control of the air/fuel ratio in the automobile's engine introducing gases. Recently, the gas sensors using solid electrolytes have been proposed for the detection of various gas species such as SO_x[13-15], NO_x[16], CO_2[17-20], Cl_2[21-23], etc.

The most important application of Li^+ conducting solid electrolytes is the material for all solid lithium battery, owing to its light weight and high electrochemical potential. The energy density ($W \cdot h \cdot kg^{-1}$) of the lithium battery is about 10-fold higher than that of the nickel-cadmium rechargeable battery. The commercialized lithium batteries utilize some organic solvents as the electrolyte. However, there is some fears about the leakage of the organic electrolyte or the firing at relatively high temperature. From these points of view, lithium solid electrolytes based on an inorganic material have been strongly desired and extensively investigated for the application to rechargeable batteries with a high-energy density and long-life.

In particular, the electrolyte which shows high Li^+ conducting properties at room temperature is a promising material. Up to now, the highest Li^+ ionic conductors reported were Li_3N single crystal and glasses based on Li_2S ($1x10^{-3}$~$2x10^{-3}$ $S \cdot cm^{-1}$ at room temperature).[24-29] Li_3N has a two dimensional structure, and the conductivity of the single crystal at 300 K is as high as $1.2x10^{-3}$ $S \cdot cm^{-1}$.[24] For glasses based on Li_2S, the high conductivity of around $1x10^{-3}$ $S \cdot cm^{-1}$ at room temperature was reported for the Li_2S-P_2S_5-LiI system and the Li_2S-B_2S_3-LiI system.[26,27] This high conductivity ascribes to the smaller bonding energy of Li^+-S or Li^+-I than that of Li^+-O and the larger tunnel size in glass materials for Li^+ migration than the crystallized solid. Recently, the Li_2S-SiS_2 system and the Li_2S-SiS_2-Li_3PO_4 system have been investigated.[28,29] The Li_3PO_4 doping with Li_2S-SiS_2 increases the number of carrier Li^+ ions and improves the stability toward lithium metal as an electrode material. On the other hand, the attempt to obtain a high Li^+ ionic conducting electrolyte has been made on the crystalline electrolyte. Kanno et al. has designed the spinel-type electrolytes based on the $Li_{2-2x}M_{1+x}Cl_4$ (M=Mg, Mn, Fe, or Cd), system and the highest conductivity of $3.4x10^{-5}$ $S \cdot cm^{-1}$ was obtained for $Li_{1.6}Mg_{1.2}Cl_4$ at 298 K.[30-32] However, these high Li^+ conducting electrolytes are not stable in a humid air condition because of the deliquescence.

Although oxide electrolytes are stable in a humid air, most investigators considered that high Li^+ ionic conducting materials cannot be obtained because of the high Li^+-O bonding energy. The highest conductivity in the oxide electrolyte was around $5x10^{-5}$ $S \cdot cm^{-1}$ at room temperature for the γ_{II}-Li_3PO_4 type electrolyte such as the Li_4GeO_4-Li_3VO_4 system.[33] A Li$^+$ super ionic conductor

(LISICON) with the $Li_{14}Zn(GeO_4)_4$ composition has also been designed and prepared by Hong.[34] However, the conductivity at room temperature was considerably low ($<10^{-6}$ $S \cdot cm^{-1}$). In the γ_{II}-Li_3PO_4 type structure, a tunnel size is too small for Li^+ to migrate because oxygen ions occupy the site to retain as a close-packed structure. Larger tunnel size is necessary for making Li^+ migration smoother. The NASICON structure possesses more suitable tunnel size for Na^+ ion than Li^+ ion. The NASICON skeleton is too large for Li^+ ion to migrate. The suitable tunnel size for Li^+ migration is expected to be obtained by reducing the lattice size of the NASICON-type structure. Furthermore, the electrical properties for these polycrystalline ceramic materials are influenced by the condition of the grain boundary such as sinterability and impurities existing at the boundaries. The control of the grain boundary becomes a key point to prepare a high ionic conducting polycrystalline electrolyte.

The present work deals with the NASICON-type ceramic Li^+ ionic conductors. The suitable lattice size for Li^+ migration and the condition of the grain boundary were investigated in order to obtain the high Li^+ conductivity even at room temperature. This thesis consists of the following six chapters.

General introduction was presented in chapter 1.

In chapter 2, the Li^+ solid electrolytes based on $LiTi_2(PO_4)_3$, i.e. the $Li_{1+x}M_xTi_{2-x}(PO_4)_3$ (M=Al, Cr, Ga, Fe, Sc, In, Lu, Y, or La) system and the $LiTi_2(PO_4)_3$ + y(Lithium compound) system were investigated. The conductivity enhancement with the partial Ti^{4+} site substitution for M^{3+} ion or the addition of lithium compounds in $LiTi_2(PO_4)_3$ were described, and the Li^+ ion conductive mechanism at the grain boundary were

mainly discussed.

In chapter 3, $LiM_xTi_{2-x}(PO_4)_3+yLi_2O$ (M=Ge,Sn,Hf,or Zr) system was investigated to determine the most suitable lattice size for a Li^+ migration through the NASICON-type structure. The Li_2O was added to obtain the high density samples. The relationship between the activation energy for bulk component and the lattice constant was described.

In chapter 4, the solid electrolytes based on $LiGe_2(PO_4)_3$ and $LiHf_2(PO_4)_3$ was investigated. The lattice size for $LiGe_2(PO_4)_3$ system is smaller than $LiTi_2(PO_4)_3$ system. The increase in lattice size for $LiGe_2(PO_4)_3$ by a larger M^{3+} ion substitution was tried to achieve higher conductivity. The lattice size for $LiHf_2(PO_4)_3$ system, on the contrary, is larger than $LiTi_2(PO_4)_3$ system. Phase transition and the M^{3+} ion substitution were mainly discussed for $LiHf_2(PO_4)_3$-based solid.

In chapter 5, the $Li_{3+x}Mg_xCr_{2-x}(PO_4)_3$ system was investigated. The lattice size is similar for $Li_3Cr_2(PO_4)_3$ to $LiTi_2(PO_4)_3$, if NASICON-type rombohedral structure is obtained. The electrical properties and the crystal structure were described.

In chapter 6, concluding remarks were presented.

The contents of this doctoral thesis are composed of the following papers.

List of Publications

(1) Ionic Conductivity of Lithium Titanium Phosphate ($Li_{1+x}M_xTi_{2-x}(PO_4)_3$, M=Al,Sc,Y, and La) Systems.
H.Aono, E.Sugimoto, Y.Sadaoka, N.Imanaka, and G.Adachi
J. Electrochem. Soc., **136**, 590 (1989).

(2) Ionic Conductivity of Solid Electrolytes Based on Lithium Titanium Phosphate Systems.
H.Aono, E.Sugimoto, Y.Sadaoka, N.Imanaka, and G.Adachi
J. Electrochem. Soc., **137**, 1023 (1990).

(3) Ionic Conductivity of $LiTi_2(PO_4)_3$ Mixed with Lithium Salts
H.Aono, E.Sugimoto, Y.Sadaoka, N.Imanaka, and G.Adachi
Chem. Lett., (1990) 331.

(4) Electrical Properties of Sintered Lithium Titanium Phsphate Ceramics ($Li_{1+x}M_xTi_{2-x}(PO_4)_3$, $M^{3+}=Al^{3+}$, Sc^{3+}, or Y^{3+})
H.Aono, E.Sugimoto, Y.Sadaoka, N.Imanaka, and G.Adachi
Chem. Lett., (1990) 1825.

(5) Electrical Properties and Sinterability of $LiTi_2(PO_4)_3$ Mixed with Lithium Salts (Li_3PO_4 or Li_3BO_3)
H.Aono, E.Sugimoto, Y.Sadaoka, N.Imanaka, and G.Adachi
Solid State Ionics, **47**, 257 (1991).

(6) DC Conductivity of $Li_{1.3}Al_{0.3}Ti_{1.7}(PO_4)_3$ Ceramic with Li Electrodes
H.Aono, E.Sugimoto, Y.Sadaoka, N.Imanaka, and G.Adachi
Chem. Lett., (1991) 1567.

(7) Electrical Properties and Sinterability for Lithium Germanium Phosphate $Li_{1+x}M_xGe_{2-x}(PO_4)_3$, M=Al,Cr,Ga,Fe,Sc, and In Systems.
H.Aono, E.Sugimoto, Y.Sadaoka, N.Imanaka, and G.Adachi
Bull. Chem. Soc. Jpn., **65**, 2200 (1992).

(8) The Electrical Properties for Ceramic Electrolytes of $LiM_xTi_{2-x}(PO_4)_3+yLi_2O$, M=Ge,Sn,Hf, and Zr Systems.
H.Aono, E.Sugimoto, Y.Sadaoka, N.Imanaka, and G.Adachi
J. Electrochem. Soc., **140**, 1827 (1993).

(9) Electrical Properties and Crystal Structure of Solid Electrolyte based on Lithium Hafnium Phosphate $LiHf_2(PO_4)_3$.
H.Aono, E.Sugimoto, Y.Sadaoka, N.Imanaka, and G.Adachi
Solid State Ionics, **62**, 309 (1993).

(10) Ionic Conductivity for $Li_{3+x}Mg_xCr_{2-x}(PO_4)_3$ System Composed of β-$Fe_2(SO_4)_3$ type Structure.
H.Aono, E.Sugimoto, Y.Sadaoka, N.Imanaka, and G.Adachi
Chem. Lett. (1993) 2033.

(11) High Li^+ Conducting Ceramic Electrolytes.
H.Aono, N.Imanaka, and G.Adachi
Acc. Chem. Res., in contribution.

Chapter 2

High Ionic Conductivity for $LiTi_2(PO_4)_3$-based Solid Electrolytes

2-1. Introduction

It is well known that NASICON (the $Na_{1+x}Zr_2P_{3-x}Si_xO_{12}$ system) is a fast Na^+ ionic conductor with a maximum conductivity at around x=2.0.[11,12] Although the end compound of $NaZr_2(PO_4)_3$ shows poor conductivity, the conductivity increases with x in the $Na_{1+x}Zr_2P_{3-x}Si_xO_{12}$ system. The enhancement of the conductivity with x occurs for the NASICON-type system because of the increase of mobile Na^+ ions and by a high densification of the sintered pellet. In addition, Na^+ ion easily migrates in the network structure, since the P^{5+} site substitution for a larger Si^{4+} ion suitably enlarges the tunnel size. However, the $Li_{1+x}Zr_2P_{3-x}Si_xO_{12}$ system, which is a Li^+ analogue of the $Na_{1+x}Zr_2P_{3-x}Si_xO_{12}$ system, exhibits a low ionic conductivity, because a Li^+ ion is too small in size to migrate freely in their three-dimensional network structures.

The ionic conductivity is greatly increased when Zr^{4+} in $LiZr_2(PO_4)_3$ is replaced by the smaller Ti^{4+} ion.[35] The tunnels in $LiTi_2(PO_4)_3$ are more suitable in size for the lithium ion migration. Furthermore, it has been reported for $LiTi_2(PO_4)_3$ increases appreciably if Ti^{4+} in the phosphate is partially substituted by M=Ga[36], Cr[37], Sc[35], or In[38-40] systems. However, the reasons for the conductivity enhancement by the substitution have not been made clear because the ionic radius of the substituted ions is very close to that of Ti^{4+} ion.

In this chapter, the $Li_{1+x}M_xTi_{2-x}(PO_4)_3$ system with various M^{3+} ions (M^{3+}; smaller Al^{3+} or larger Cr^{3+}, Ga^{3+}, Fe^{3+}, Sc^{3+}, In^{3+} Lu^{3+}, Y^{3+}, or La^{3+} ion compared with Ti^{4+} ion) was prepared and discussed the reasons for the conductivity enhancement by the M^{3+} substitution. Furthermore, the lithium salt (Li_3PO_4 or Li_3BO_3) was used as the binder to prepare a high-density pellet.

2-2. Experimental

—Materials—

For the preparation of the $Li_{1+x}M_xTi_{2-x}(PO_4)_3$ system, a stoichiometric mixture of Li_2CO_3 (99.99%), SiO_2 (99.999%), M_2O_3 (M=Al, Cr, Ga, Fe, Sc, In, Lu, Y, and La) (99.9% or 99.99%), TiO_2 (99.9%), and $(NH_4)_2HPO_4$ (extra pure grade), whose purities were at least reagent grade, was ground, and heated in a platinum crucible at 1173 K for 2 h. The resulting material was reground into fine powder using a ball-mill for 6 h by a wet process. The dried powder was reheated at 1173 K for 2 h and then ball-milled again for 12 h. The particle size of the dried powder was smaller than 1 μm, which was determined by a centrifugal particle size analyzer (Shimadzu SA-CP3). A suitable amount of 3% PVA solution was added to the powder as a binder and the mixture was pressed into pellets at the pressure of $1x10^8$ Pa. The pellets were sintered at 1073~1523 K for 2 h. The sintering temperature was chosen in such a way that high density (low porosity) pellets were obtained. Table 2-1 shows the sintering temperature (x=0.2~0.5) and the density of the pellets (x=0.3) for the $Li_{1+x}M_xTi_{2-x}(PO_4)_3$ systems. These sintered pellets were polished with 800 grade emery paper and gold was deposited by a vacuum

evaporation onto the both surfaces of the disc so as to obtain a good contact between the electrolyte and the electrode.

In the case of the $LiTi_2(PO_4)_3$ + y(lithium compound) systems, the starting materials of $LiTi_2(PO_4)_3$ was ground and reacted in the platinum crucible at 1173 K for 2 h. The prepared $LiTi_2(PO_4)_3$ powder was reground into a fine powder with a ball-mill for 6 h by a wet process. The mixture of $LiTi_2(PO_4)_3$ powder and the lithium salt (Li_3PO_4 or Li_3BO_3) was reheated at 1173 K for 2 h and then ball-milled again for 12 h by the same process. An extra pure grade of Li_3PO_4 was utilized. A stoichiometric mixture of Li_2CO_3 and H_3BO_3 (>99.5%) was added in the case of $LiTi_2(PO_4)_3$-Li_3BO_3 preparation. This mixture decomposes into Li_3BO_3 by a heat treatment. A suitable amount of 3% polyvinyl alcohol (PVA) solution was added to the powder, and the mixture was pressed into a pellet at a pressure of $1x10^8$ Pa. The pellets were sintered at 1073~1293 K for 2 h. The sintering temperature was chosen in such a way that the maximum conductivity was obtained.

Table 2-1. Sintering temperature for the $Li_{1+x}M_xTi_{2-x}(PO_4)_3$ systems.

M^{3+} ion	Sintering temp. (K)	Porosity x=0.3 (%)
Al	1253~1273	4.1
Cr	1463~1523	27.9
Ga	1173~1203	8.2
Fe	1323	4.8
Sc	1473~1483	2.0
In	1273	4.4
Lu	1173	1.7
Y	1173	0.5
La	1173	0.1

—Measurements—

A quantitative analysis of Li^+ in the sintered samples was carried out by an atomic absorption analysis. X-ray-diffraction analysis (Cu-Kα radiation) was conducted with a Rigaku Rotaflex. High-purity Si powder (99.99%) was used as an internal standard for the lattice constant determination. Electrical conductivity was measured by means of the complex-impedance method (100~1M Hz) with LCZ Meters 4276A and 4277A from Hewlett Packard Co. The pellet was heated up to 573K once in flowing dry N_2 before the electrical measurement to eliminate the adsorbed water. Porosity of the sintered pellets was determined by the Archimedes' method. Scanning electron micrographs for the surface of the samples were obtained with a JEOL JXA-733 X-ray microanalyzer.

2-3. Results and Discussion

2-3-1. NASICON structure

The NASICON-type network structure of $LiM_2(PO_4)_3$ (M=tetra-valent cation) is presented in Fig. 2-1. $LiM_2(PO_4)_3$ is composed of both MO_6 octahedra and PO_4 tetrahedra, which are linked by their corners to form a three dimensional network structure (space group $R\bar{3}c$).[41,42] Two types of lithium ion sites, A_1 and A_2, exist in the structure. The A_2 sites are not shown in the figure. A_1 sites are fully occupied by lithium ions, and A_2 sites are completely vacant for $LiM_2(PO_4)_3$. The A_2 sites are partially occupied by the tri-valent M^{3+} ion in the $Li_{1+x}M(III)_xTi_{2-x}(PO_4)_3$ system.

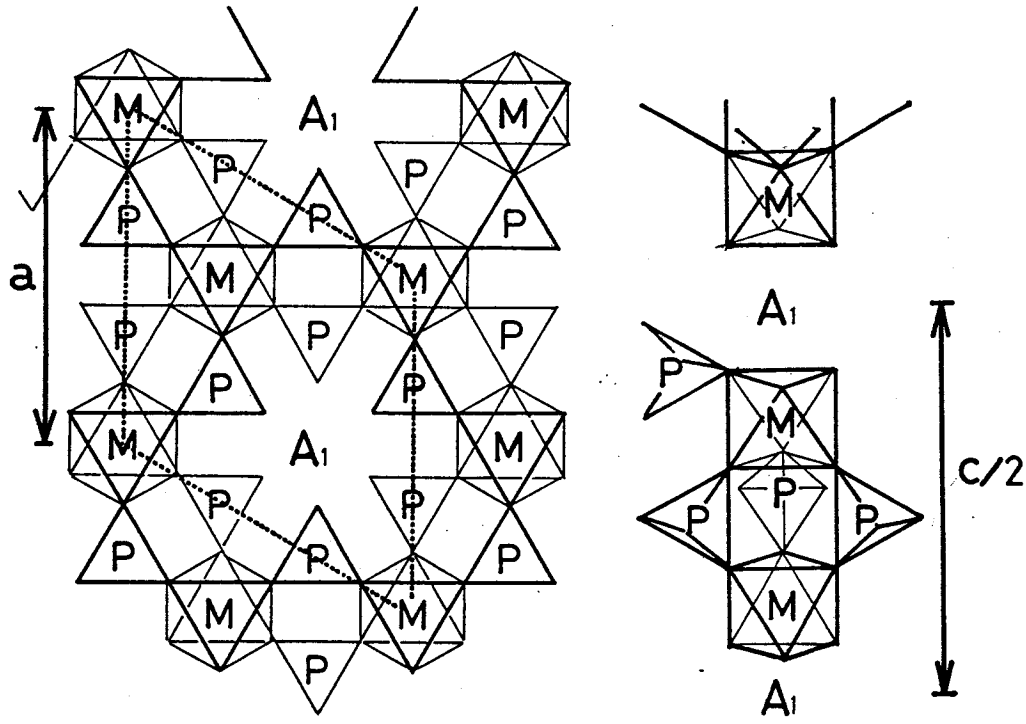

Fig. 2-1. NASICON-type structure of $LiM_2(PO_4)_3$, (M=tetra-valent cation, A_1= lithium ion site). A(2) site did not show to avoid a troublesome figure.

2-3-2. $Li_{1+x}M_xTi_{2-x}(PO_4)_3$, M=Al,Sc,Y,La,etc. system

—Phase—

Lattice constants versus x value for the $Li_{1+x}M_xTi_{2-x}(PO_4)_3$, (M=Al,Cr,Ga,Fe,Sc,In,Lu,Y, or La) systems are presented in Fig. 2-2. Limits of phase of the $Li_{1+x}M_xTi_{2-x}(PO_4)_3$ systems determined from powder X-ray analysis are plotted against the ionic radii[43] of M^{3+} and the x value in Fig. 2-3. Single (rhombohedral) and mixed ($LiTi_2(PO_4)_3$ + $Li_3M_2(PO_4)_3$) phase areas are also shown in the same figure. When Ti^{4+} sites in $LiTi_2(PO_4)_3$ were partially substituted by Al^{3+}, the lattice constants decreased linearly with the increase in Al^{3+} up to x=0.4 because the ionic radius of Al^{3+} was smaller than that of Ti^{4+} (Fig. 2-2). The single phase was formed up to x=0.3, while an unknown phase appeared for x>0.4

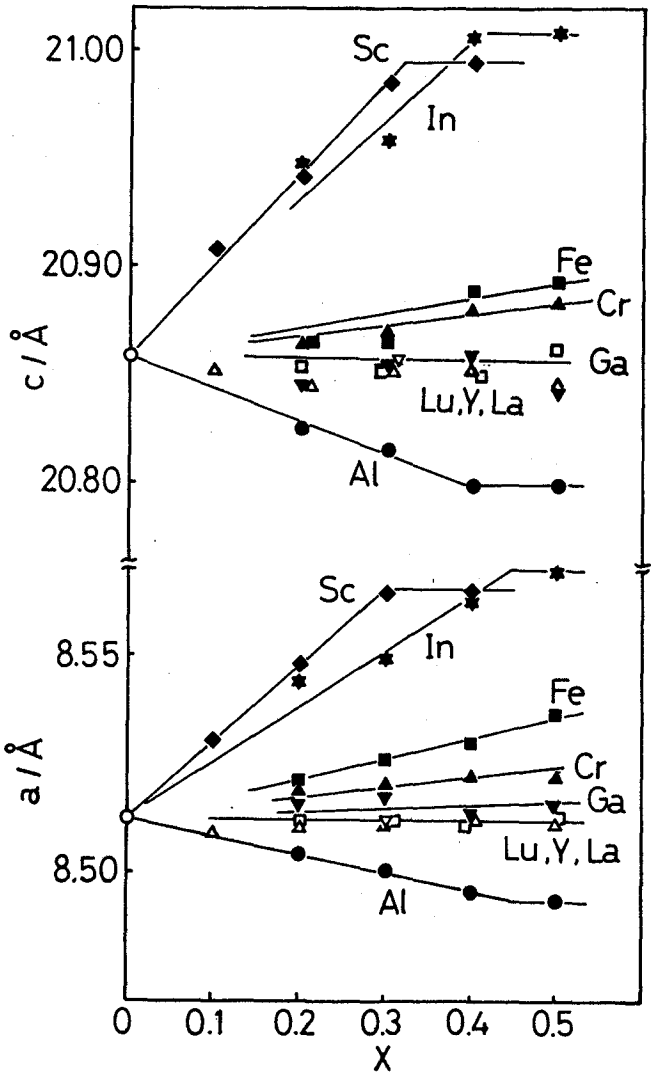

Fig. 2-2. Lattice constants (hexagonal unit) for the $Li_{1+x}M_xTi_{2-x}(PO_4)_3$ system; x=0(○), M=Al(●), Cr(▲), Ga(▼), Fe(■), Sc(◆), In(✱), Lu(▽), Y(△), La(□).

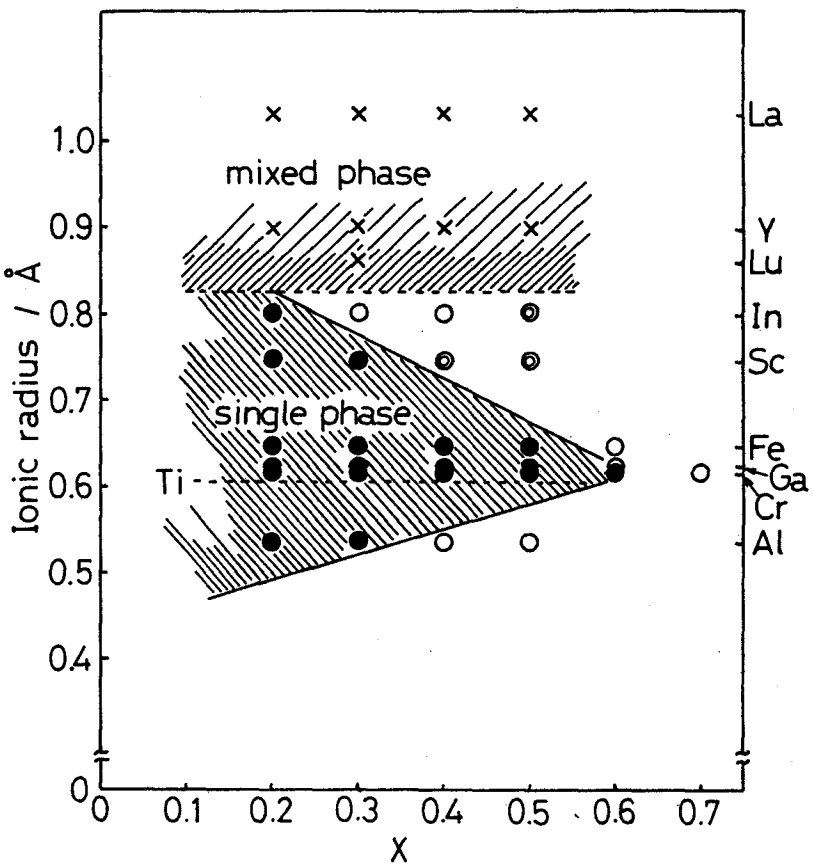

Fig. 2-3. Limits of phase of the $Li_{1+x}M_xTi_{2-x}(PO_4)_3$ systems determined from X-ray analysis are plotted against the ionic radii of M^{3+} and the x value.

Rhombohedral phase of $Li_{1+x}M_xTi_{2-x}(PO_4)_3$ (●)
Mixed phase of $LiTi_2(PO_4)_3$ and $Li_3M_2(PO_4)_3$ (X)
Monoclinic phase of the $Li_{1+x}M_xTi_{2-x}(PO_4)_3$ (◎)
$Li_{1+x}M_xTi_{2-x}(PO_4)_3$ phase and unknown phase (○)

(Fig. 2-3). The replaceable limit for an Al^{3+} ion was around x=0.4. In the substituted system for a slightly larger cation (Cr^{3+}, Ga^{3+}, or Fe^{3+}) than Ti^{4+}, the lattice constants slightly increased with the M^{3+} fraction and no second phase appeared for x<0.6. The M^{3+} (Cr^{3+}, Ga^{3+}, or Fe^{3+}) ion is easy to place at the Ti^{4+} site because its ionic radius is close to that of Ti^{4+}. In the sample of the substituted systems for larger Sc^{3+} or In^{3+}, the lattice constants increased linearly with increase of x in the $Li_{1+x}M_xTi_{2-x}(PO_4)_3$ systems. A monoclinic phase presented as a second phase by the excess substitution of Sc^{3+} (x>0.3) and In^{3+} (x>0.4) ions for Ti^{4+}. On the other hand, the lattice constants for Lu^{3+}, Y^{3+}, or La^{3+} analogous were the same as that for $LiTi_2(PO_4)_3$. The replacement of the Ti^{4+} site with Lu^{3+}, Y^{3+}, or La^{3+} did not occur because of their larger ionic radii, and this resulted in the mixed phases of $LiTi_2(PO_4)_3$ and $Li_3M_2(PO_4)_3$ (M=Lu, Y, or La). The relation between the lattice constants and the ionic radius of M^{3+} for $Li_{1.3}M(III)_{0.3}Ti_{1.7}(PO_4)_3$ (x=0.3) is presented in Fig. 2-4. Corresponding results of tetravalent substituted systems for $Li_{1.0}M(IV)_{0.3}Ti_{1.7}(PO_4)_3$ (M=Ge and Zr) were also obtained in this study, and are shown in the same figure. In the sample of Al^{3+},Cr^{3+},Ga^{3+},Fe^{3+}, or Sc^{3+} substituted systems, the lattice constants increased linearly with increasing ionic radius. The same results were also obtained for the tetravalent substituted systems. The lattice constants for the In^{3+} substitution deviated from the straight line in the figure, since In_2O_3, used as a starting material, is easily vaporized at elevated temperatures. The lattice constants for the trivalent (M=Lu,Y, or La) substituted system were equal to that for $LiTi_2(PO_4)_3$. From these results, the $Li_{1+x}M_xTi_{2-x}(PO_4)_3$ systems

are classified into two groups.

(1) Al^{3+}, Cr^{3+}, Ga^{3+}, Fe^{3+}, Sc^{3+}, or In^{3+} substituted systems: $Li_{1+x}M_xTi_{2-x}(PO_4)_3$ single phase.

(2) Lu^{3+},Y^{3+}, or La^{3+} systems : $LiTi_2(PO_4)_3$ + $Li_3M_2(PO_4)_3$ mixed phase.

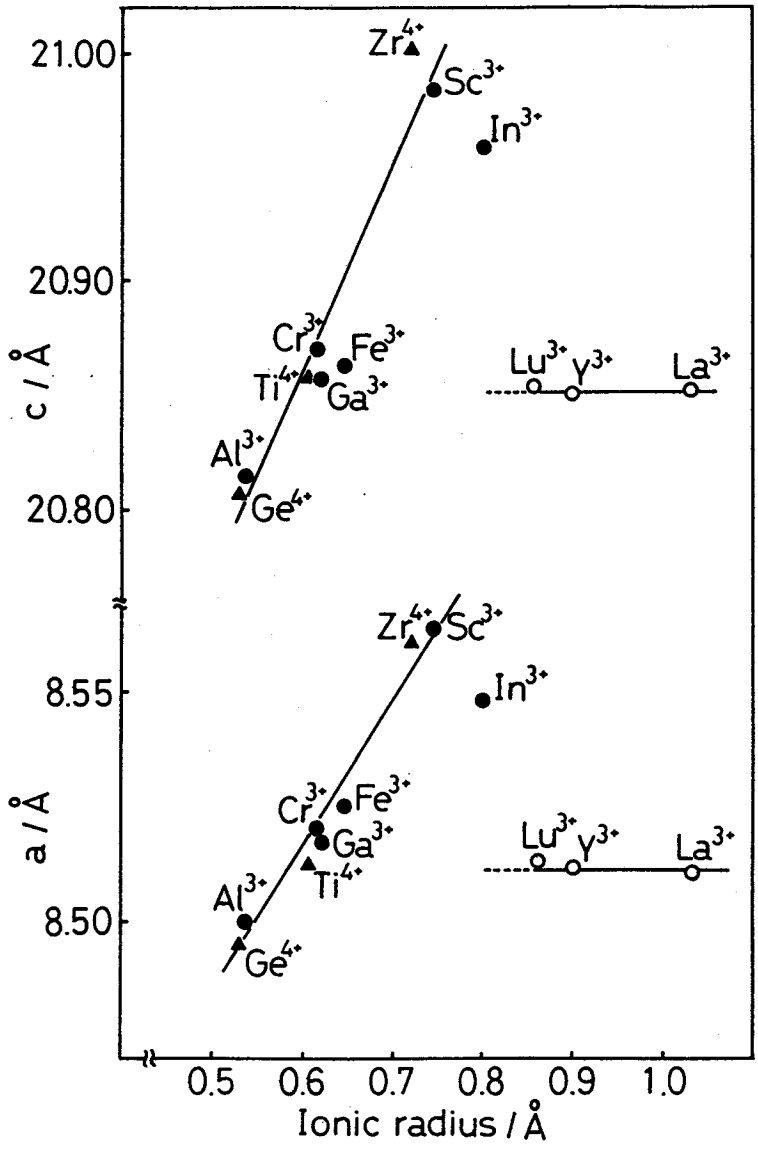

Fig. 2-4. Variation of the lattice constants vs. the ionic radius of the M^{3+} or M^{4+} ions.
$Li_{1.3}M_{0.3}Ti_{1.7}(PO_4)_3$ systems (single phase) (●)
$Li_{1.3}M_{0.3}Ti_{1.7}(PO_4)_3$ systems (mixed phase) (○)
$LiM_{0.3}Ti_{1.7}(PO_4)_3$ systems (▲)

—Conductivity and sinterability—

The relation between the porosity of the sintered pellets and the x value for the $Li_{1+x}M_xTi_{2-x}(PO_4)_3$ systems is shown in Fig. 2-5. $LiTi_2(PO_4)_3$ (x=0) could not be obtained as a dense pellet (porosity: 34%). Porosity decreased considerably by the M^{3+} substitution for all the systems examined. The porosity for Y^{3+} or La^{3+} mixed systems was particularly low. A second phase formed may fill pores of the sintered $LiTi_2(PO_4)_3$ phase. On the other hand, the porosity for the Cr^{3+} system is higher than that of the other systems.

Figure 2-6 presents the conductivity results with x in the $Li_{1+x}M_xTi_{2-x}(PO_4)_3$ systems at 298K. The conductivity was greatly enhanced by the M^{3+} substitution and the maximum conductivity was obtained at around x=0.3 for all the systems examined except for the Cr^{3+} substituted one. The conductivity for the sample of $Li_{1.3}M_{0.3}Ti_{1.7}(PO_4)_3$ (M=Al or Sc) showed the maximum value of $7x10^{-4}$ $S \cdot cm^{-1}$ at 298 K for all the M^{3+} substitution systems. For the Al^{3+},Cr^{3+},Ga^{3+},Fe^{3+},Sc^{3+}, or In^{3+} substituted system, the conductivity could not be correlated with the ionic radius of the M^{3+} ion. In other words, the conductivity did not depend on the deviation of the cell constants by the M^{3+} substitution. Astonishingly, the conductivity also greatly increased for the Lu^{3+}, Y^{3+}, or La^{3+} mixed phase group compare with the $LiTi_2(PO_4)_3$, although the Ti^{4+} site was not replaced by these ions. This conductivity enhancement for the mixed phase system indicates that the M^{3+} ion substitution and the Li^+ ion insertion into A(2) sites are not the main reason for the conductivity enhancement.

Figure 2-7 presents the temperature dependence of

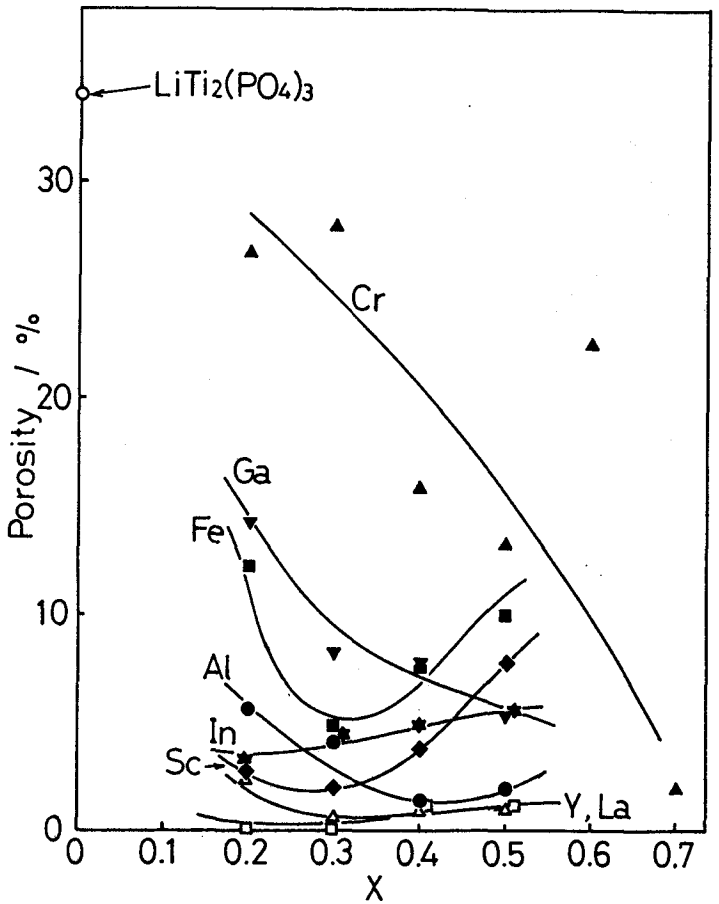

Fig. 2-5. Variation of the porosity for the $Li_{1+x}M_xTi_{2-x}(PO_4)_3$ systems, x=0(○), M=Al(●), Cr(▲), Ga(▼), Fe(■), Sc(◆), In(✱), Y(△), La(□).

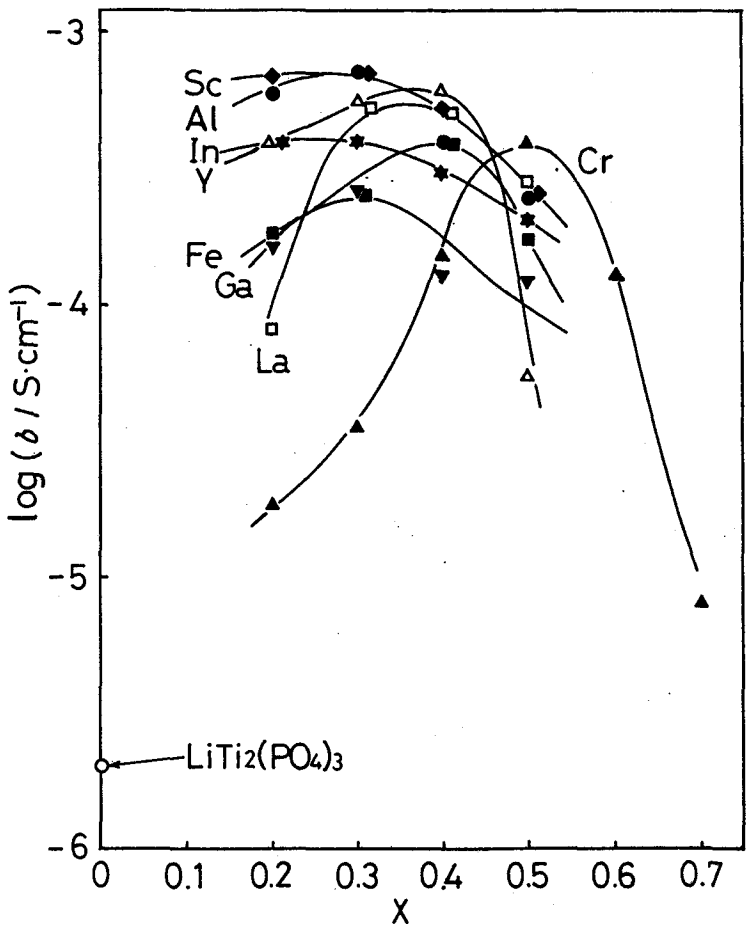

Fig. 2-6. Variation of the conductivity at 298 K for the $Li_{1+x}M_xTi_{2-x}(PO_4)_3$ systems, x=0(○), M=Al(●), Cr(▲), Ga(▼), Fe(■), Sc(◆), In(✱), Y(△), La(□).

conductivity for $Li_{1.3}Al_{0.3}Ti_{1.7}(PO_4)_3$ and $Li_{1.3}La_{0.3}Ti_{1.7}(PO_4)_3$. A gentle curve appeared over the entire temperature range studied, but no phase transition was observed from a DTA (differential thermal analysis) measurement. The activation energies at low and high (>500K) temperatures are about 0.35 eV and 0.20 eV, respectively.

Figure 2-8 shows the relationship between the conductivity at 298K and the porosity of the sintered pellets for single phase when dopant concentrations are x=0.2 and x=0.3, and mixed phase (x=0.3, x=0.4) in addition to the $LiTi_2(PO_4)_3$ phase. The conductivity increased with the decrease of the porosity. In other words, the conductivity greatly depended on the density of the sintered pellets. The conductivity for the group of the mixed phase systems (Lu^{3+}, Y^{3+}, or La^{3+}) was slightly smaller than that for the single phase ones (Al^{3+}, Cr^{3+}, Ga^{3+}, Fe^{3+}, Sc^{3+}, or In^{3+}). The mixed phase systems showed high conductivity and density in comparison with single phase $LiTi_2(PO_4)_3$. In the mixed phase system, the conductive phase on the lithium ion is the three dimensional network in $LiTi_2(PO_4)_3$, as the second phase of $Li_3M_2(PO_4)_3$ is a lower ionic conductor which was confirmed by our measurement in this study. The second phase is influential only on the density of the pellet. The main reason for the conductivity enhancement by the M^{3+} substitution is the increase of the sintered pellet density, which is very effective to the existence of the second phase.

—Electrical properties of bulk and grain boundary—

Figure 2-9 presents a typical complex impedance plot with gold blocking electrodes. The complex impedance method has the

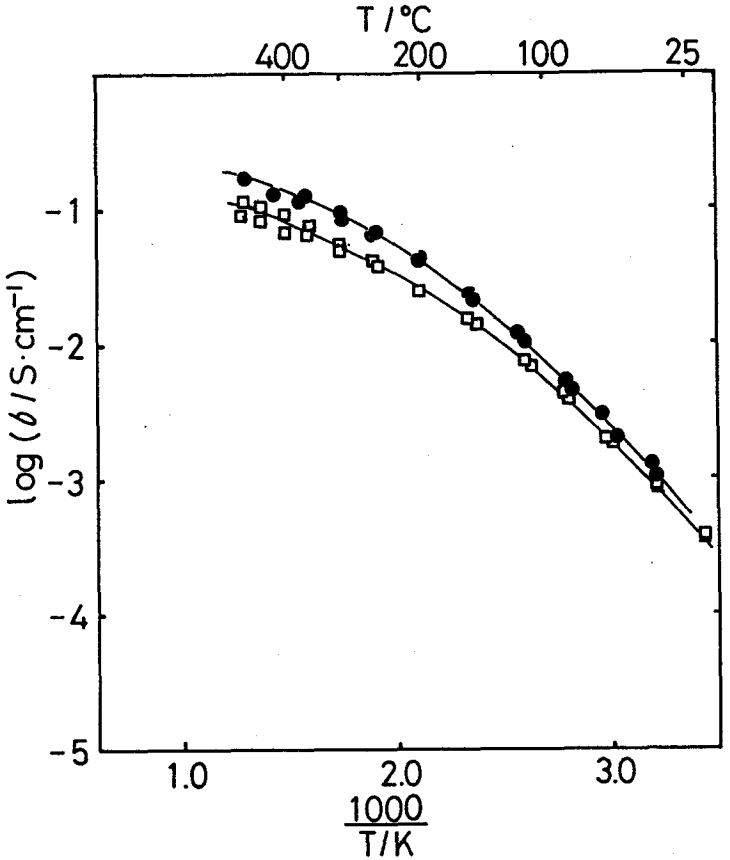

Fig. 2-7. The σ -1/T relation for the sample of $Li_{1+x}M_xTi_{2-x}(PO_4)_3$ system.
$Li_{1.3}Al_{0.3}Ti_{1.7}(PO_4)_3$(●)
$Li_{1.3}La_{0.3}Ti_{1.7}(PO_4)_3$(□)

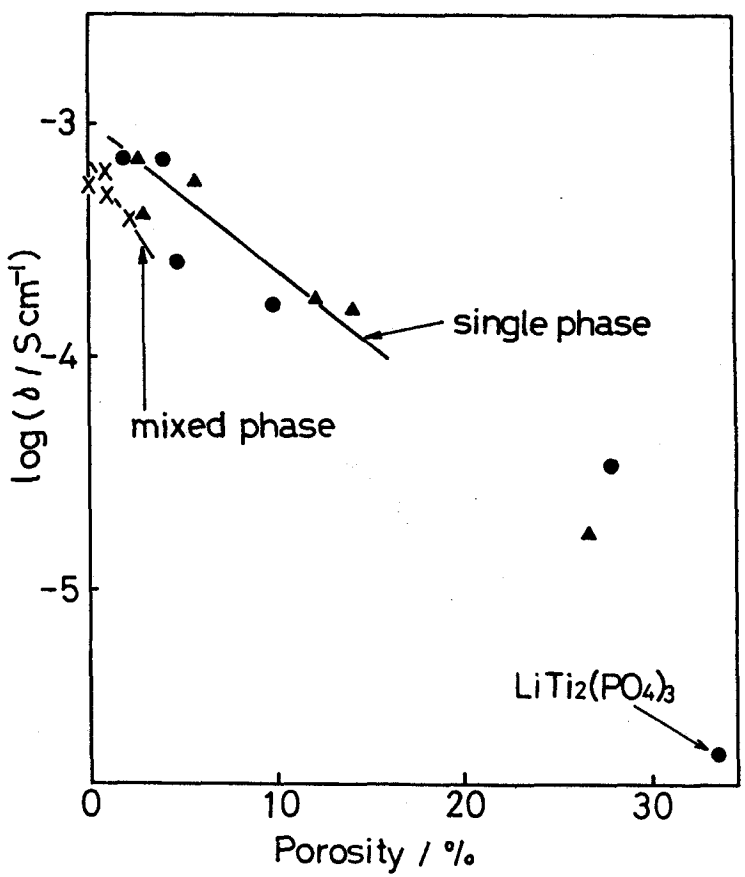

Fig. 2-8. The relationship between the conductivity at 298 K and the porosity of the sintered pellets. The sample of the single phase $Li_{1+x}M_xTi_{2-x}(PO_4)_3$ at x=0.2(▲) and x=0.3(●), Mixed phase $LiTi_2(PO_4)_3$+$Li_3M_2(PO_4)_3$ (X)

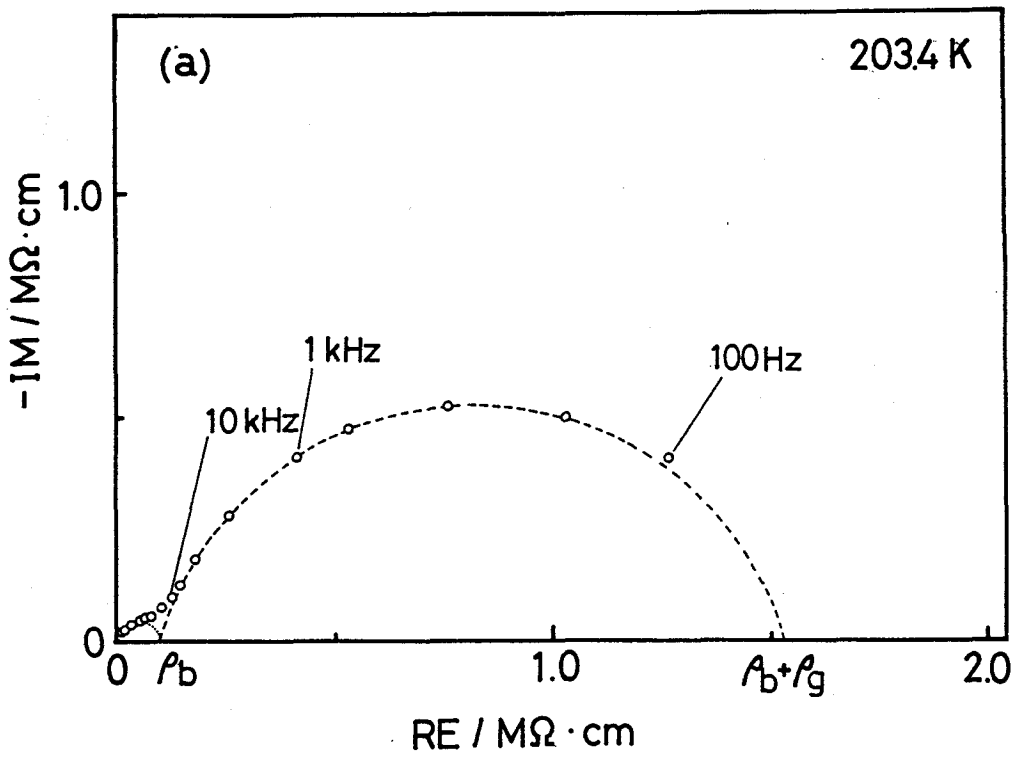

Fig. 2-9. Typical complex impedance plots at 203.4 K for $Li_{1.3}Al_{0.3}Ti_{1.7}(PO_4)_3$ sample.

advantage for determining both the bulk and the grain boundary resistance of ceramics separately.[45,46] The bulk resistance ρ_b was determined from the intersection point of the semicircle to the abscissa in a higher-frequency region. The total resistance $\rho_b+\rho_g$ was obtained from the analogous point of a lower-frequency region. In general, the relationship between conductivity and temperature is represented by the equation:

$$\sigma T=\sigma_0 \exp(-E_a/kT) \qquad [1]$$

where σ_0, is the pre-exponential factor, E_a is the activation energy for a Li^+ migration, and k is the Boltzmann constant. The σT-1/T relations of the bulk, the grain boundary, and the total (bulk and grain boundary) conductivities for the samples of $LiTi_2(PO_4)_3$ and $Li_{1.3}Al_{0.3}Ti_{1.7}(PO_4)_3$ are shown in Fig. 2-10. A straight relationship was obtained for the σT-1/T relation of

both the bulk and the grain boundary. The total conductivity at around room temperature was mainly controlled by that of the grain boundary component. At higher temperature above ca. 500 K, the total conductivity is expected to be controlled by that of bulk component. A gentle curve of the total conductivity at around 500 K is mainly ascribed to the difference in the slope of the line in the σT-1/T relation between the bulk and the grain boundary.

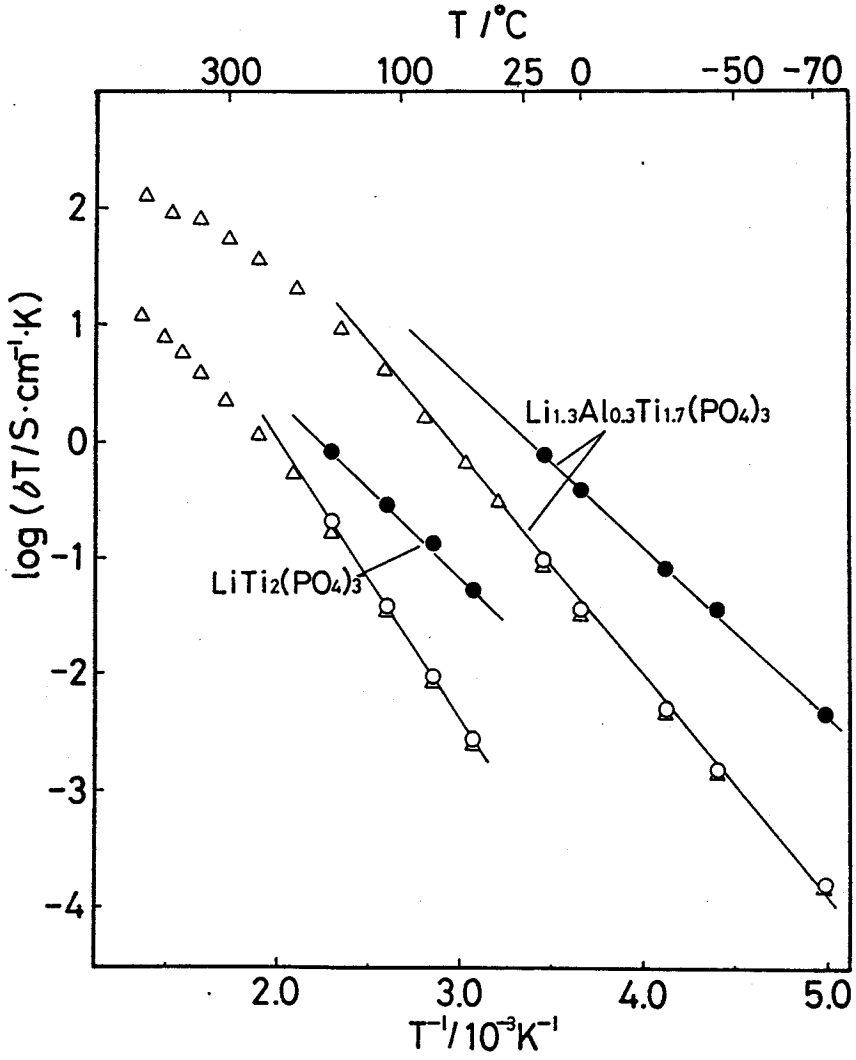

Fig. 2-10. The σT-1/T relation of the bulk component, the grain boundary and the total of them, for the samples of $LiTi_2(PO_4)_3$ and $Li_{1.3}Al_{0.3}Ti_{1.7}(PO_4)_3$.
bulk(●), grain boundary(○), total(△)

The conductivities of the bulk and the grain boundary at 298 K vs. x value for the $Li_{1+x}M_xTi_{2-x}(PO_4)_3$ (M=Al,Sc, and Y) systems are presented in Fig. 2-11. An analogue for the activation energies is also shown in Fig. 2-12. Although the activation energy of the bulk did not change with the increase in x value for all the systems examined, the bulk conductivity was considerably enhanced with the M^{3+} substitution. The change in a skeleton size by the M^{3+} substitution for the $Li_{1+x}M_xTi_{2-x}(PO_4)_3$ system hardly influence the Li^+ mobility since the conductivities and activation energies of the bulk with the smaller Al^{3+} substituted system were similar to those of larger Sc^{3+} substituted one. Furthermore, the Y^{3+} system, i.e. the mixed phase ($LiTi_2(PO_4)_3$ and $Li_3Y_2(PO_4)_3$) system also showed a high bulk conductivity. The conductive bulk phase in this system is only $LiTi_2(PO_4)_3$. The second phase, $Li_3Y_2(PO_4)_3$, acts as a binder for the dense pellet and do not influence to the bulk structure. The activation energy of the grain boundary component decreased by the M^{3+} addition. The sinterability also increased with the M^{3+} addition. For $LiTi_2(PO_4)_3$ (x=0) sample, the activation energy of the grain boundary showed high value with poor sinterability. The decrease in the activation energy at the grain boundary seems to be correlated with the difference in sinterability. As a result, the conductivity of the grain boundary is enhanced by two order of magnitude for all the systems with the M^{3+} substitution. The bulk conductivity enhancement might be influenced by the increase of the carrier Li^+ ion with the enhancement of the conductivity at the grain boundary.

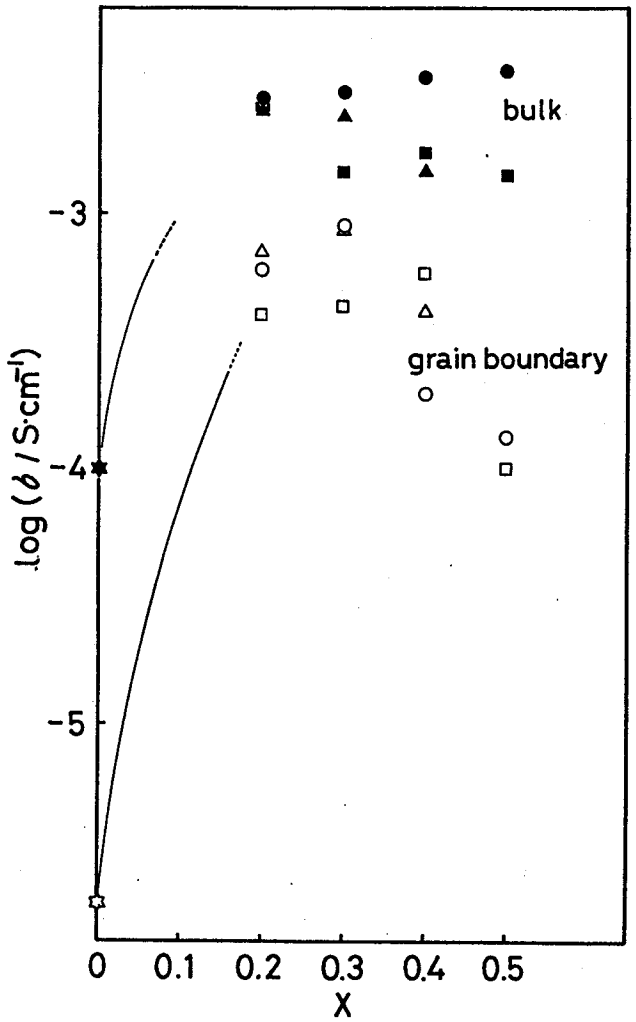

Fig. 2-11. The conductivities of the bulk and the grain boundary at 298 K in the $Li_{1+x}M_xTi_{2-x}(PO_4)_3$ system.
M=Al: bulk(●), grain boundary (○)
M=Sc: bulk(▲), grain boundary (△)
M=Y : bulk(■), grain boundary (□)

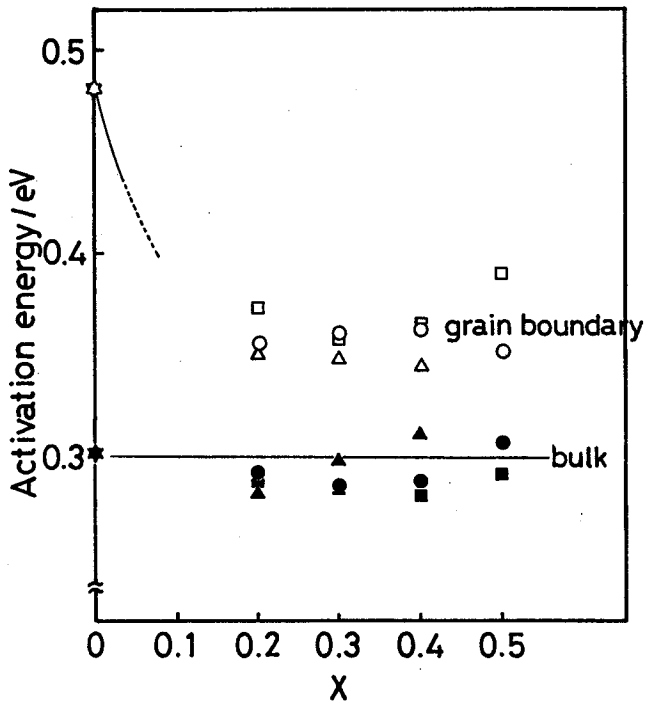

Fig. 2-12. The activation energies of the bulk and the grain boundary in the $Li_{1+x}M_xTi_{2-x}(PO_4)_3$ system.
M=Al: bulk(●), grain boundary (○)
M=Sc: bulk(▲), grain boundary (△)
M=Y : bulk(■), grain boundary (□)

2-3-3. $LiTi_2(PO_4)_3$ + y(Lithium compound) system

—Phases—

For $LiTi_2(PO_4)_3$ mixed with lithium salts, only the $LiTi_2(PO_4)_3$ phase was clearly confirmed by the X-ray diffraction analysis. No other peaks were found for all the sintered samples with lithium salts. The lattice constants for the $LiTi_2(PO_4)_3$ structure maintained the same value in spite of the lithium-salt addition, suggesting that the salts did not react with $LiTi_2(PO_4)_3$. The Li content determined by the atomic absorption analysis was found to remain a constant during the sintering process. These lithium salts would be melted during the sintering process, and it exists at grain boundaries as a glassy second phase.

—Sinterability—

Figure 2-13 shows the correlation between the porosity of the sintered pellets and the amount of the mixed lithium salt. A high-density pellet could not be obtained for $LiTi_2(PO_4)_3$ without lithium salts. The porosity decreased with the lithium salt addition.

Figure 2-14 presents the surface microstructure of the sintered pellets. $LiTi_2(PO_4)_3$ sintered at 1433 K (a) was quite porous. Its particle size is almost the same as that of the starting powder. For the sample sintered at 1533 K or higher (b), the particle grew greatly, and many cracks were observed. A durable pellet with a high mechanical strength could not be obtained in this sample. For the sample with Li_3PO_4 addition (c), grains are closely in contact with each other. Although the

particles grew with increasing sintering temperature, no cracks were observed in the sintered pellets (d). This sample is shown in higher magnification in (e). Astonishingly, most of the edges of the neighboring grains in (d and e) are parallel to each other. A remarkable epitaxial-like grain growth took place during sintering of the grains. The lithium salt seems to act as a flux for the grain growth rather than merely as a binder. The high sinterability leads to a high uniformity for each particle; that is to say, probably the three-dimensional grain network exactly matches with that of a neighboring grain. The surface of the sample with added Li_3BO_3 is continuously smooth (f). This might indicate Li_3BO_3 glass formation. A less porous sample was obtained with Li_3BO_3 addition. This result also suggests the easiness of glassy formation. The formed glassy phases may fill the pores. From these results, the lithium-salt addition is effective to improve the linkage between the grains.

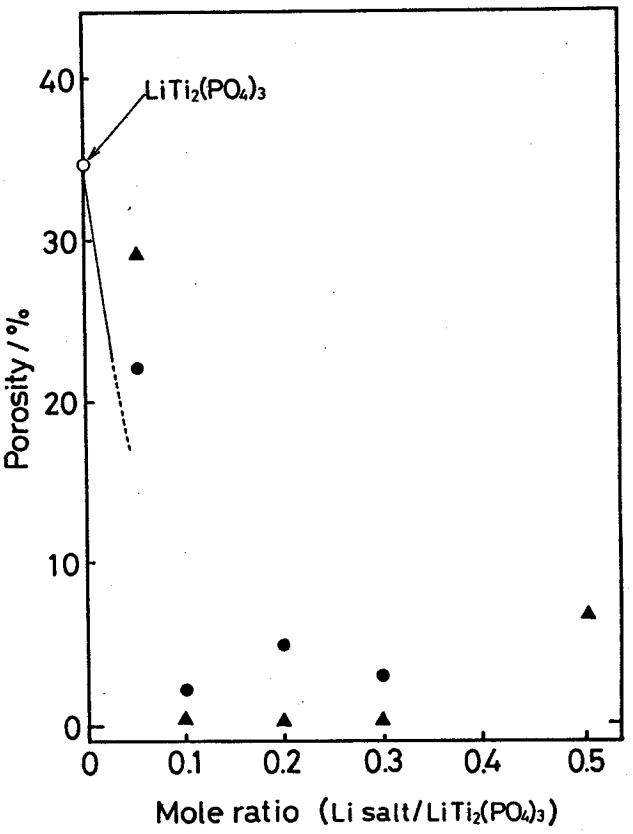

Fig. 2-13. The variation of the pellet porosity for $LiTi_2(PO_4)_3$ mixed with various lithium salts.
$LiTi_2(PO_4)_3$+yLi_3PO_4 system(●)
$LiTi_2(PO_4)_3$+yLi_3BO_3 system(▲)

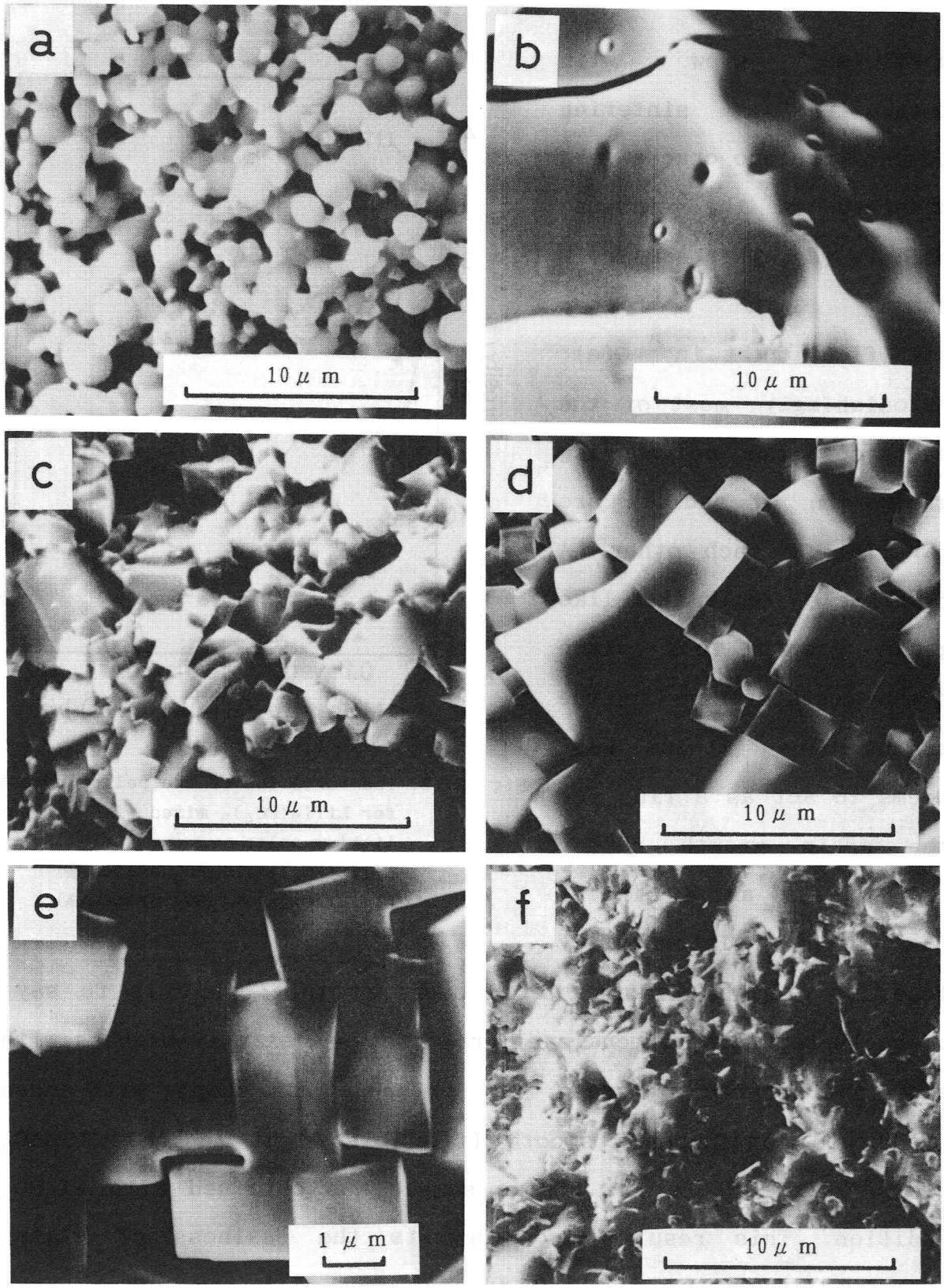

Fig. 2-14. The surface microstructure of the sintered pellets.
(a) $LiTi_2(PO_4)_3$ (sintered at 1433 K)
(b) $LiTi_2(PO_4)_3$ (sintered at 1533 K)
(c) $LiTi_2(PO_4)_3$+0.2Li_3PO_4 (sintered at 1073 K)
(d)(e) $LiTi_2(PO_4)_3$+0.2Li_3PO_4 system (sintered at 1173 K)
(f) $LiTi_2(PO_4)_3$+0.2Li_3BO_3 system(sintered at 1073 K)

—Conductivity—

The σT-1/T relation for the systems with lithium-salt addition is plotted in Fig. 2-15. The conductivity was greatly enhanced by the lithium salt addition. The activation energy for the Li^+ ionic conduction is also decreased by the salt addition. The curve for $LiTi_2(PO_4)_3$ is almost linear, while a gently curved relation appeared over the entire temperature range for the samples with lithium-salt additions. No thermal peak for a phase transition was detected on DTA curves. The relation between the total conductivity (bulk and grain boundary) at 298 K and the lithium-salt content is shown in Fig. 2-16. The conductivity is greatly enhanced by the salt addition. The conductivity decreased with the addition of excess lithium salts because of the low

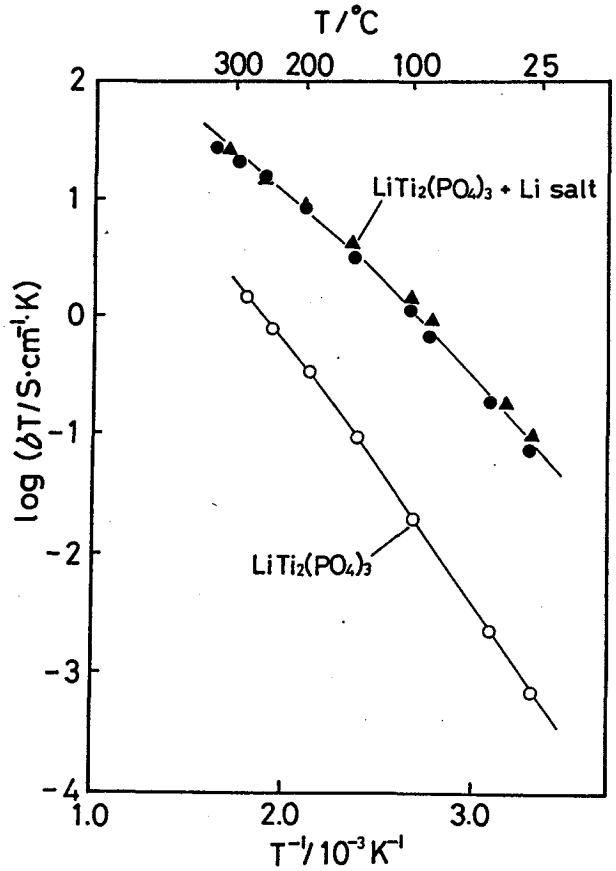

Fig. 2-15. The σT-1/T relation for the $LiTi_2(PO_4)_3$+y(lithium salt) system.
$LiTi_2(PO_4)_3$ (○)
$LiTi_2(PO_4)_3$+yLi_3PO_4 system(●)
$LiTi_2(PO_4)_3$+yLi_3BO_3 system(▲)

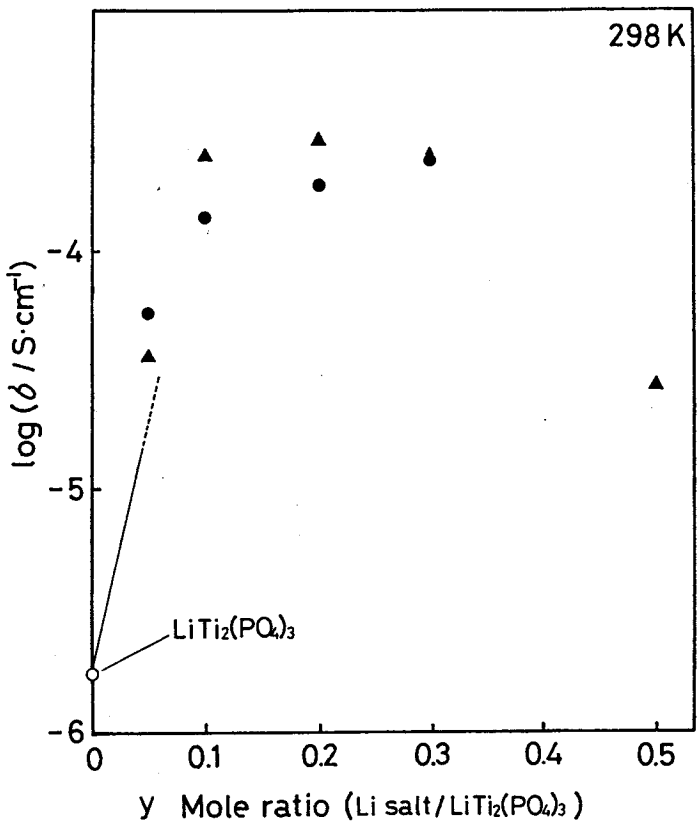

Fig. 2-16. Variation of the conductivity at 298 K for the lithium added systems.
$LiTi_2(PO_4)_3$ (○)
$LiTi_2(PO_4)_3$+yLi_3PO_4 system (●)
$LiTi_2(PO_4)_3$+yLi_3BO_3 system (▲)

conductivity of the salt. The maximum conductivity, i.e. 3.0×10^{-4} $S \cdot cm^{-1}$ is achieved for $LiTi_2(PO_4)_3$+0.2Li_3BO_3. The conductivity of the Li_3BO_3-added system showed a higher value compared with that of Li_3PO_4 system. This higher conductivity for the Li_3BO_3-added system may be correlated with its low porosity.

The conductivities of the bulk and the grain boundary could be estimated separately from the complex impedance plots. The temperature dependence of the conductivity for the bulk, the grain boundary, and the total conductivity for $LiTi_2(PO_4)_3$ and $LiTi_2(PO_4)_3$+0.2Li_3BO_3 are plotted in Fig. 2-17. It seems that the total conductivities are mainly controlled by the grain-boundary component for this system. Therefore, the condition of the grain-boundary such as sinterability influences the total conductivity.

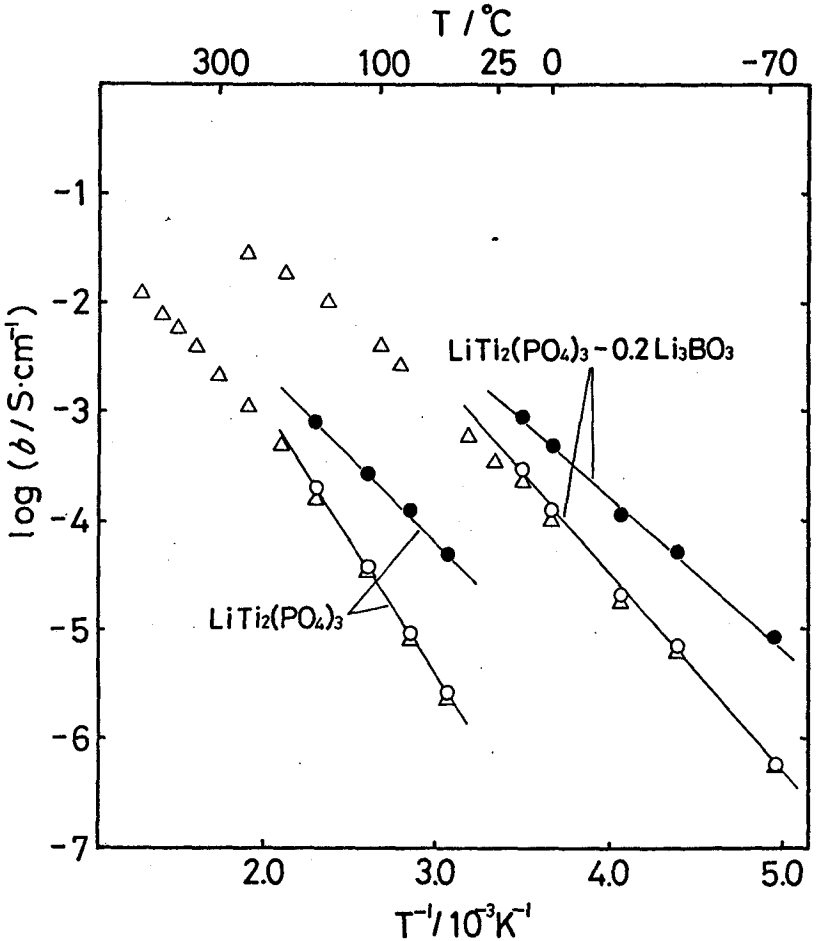

Fig. 2-17. The σT-1/T relation for $LiTi_2(PO_4)_3$ and $LiTi_2(PO_4)_3$+0.2Li_3BO_3.
bulk(●), grain boundary(○), total(△)

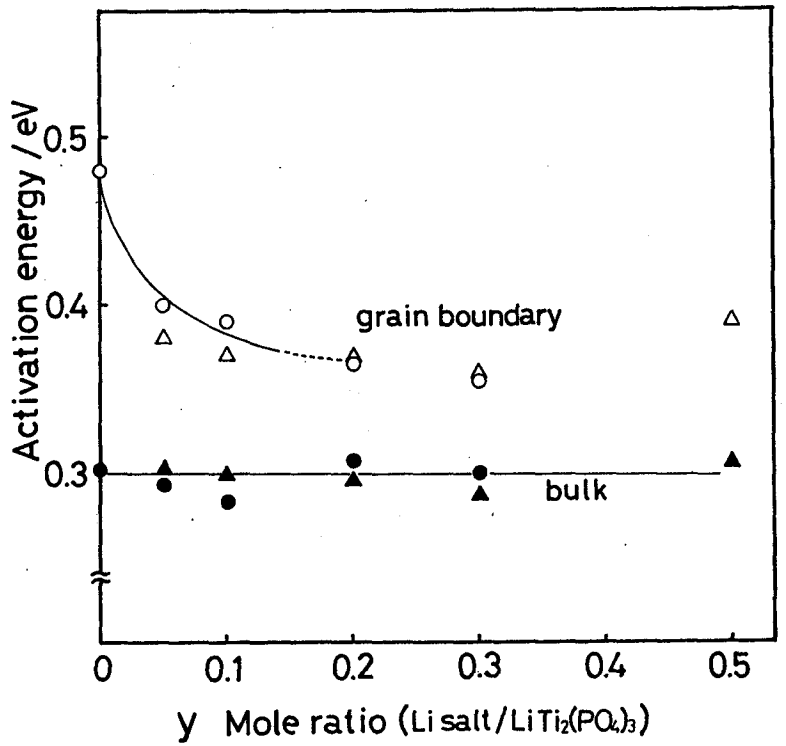

Fig. 2-18. The activation energies of the bulk and the grain boundary.
$LiTi_2(PO_4)_3$+yLi_3PO_4; bulk(●), grain boundary(○)
$LiTi_2(PO_4)_3$+yLi_3BO_3; bulk(▲), grain boundary(△)

The activation energies derived from the bulk and the grain boundary components of conductivity are shown in Fig. 2-18. The activation energy of the bulk component was constant. This indicates that the $LiTi_2(PO_4)_3$ bulk phase did not react with the lithium salt as mentioned previously. In the case of the grain boundary, the activation energy decreased with lithium-salt addition. Figure 2-19 shows the conductivities of the bulk and grain boundary at 298 K. The conductivity for the grain boundary is greatly enhanced by the salt addition. The decreases of the porosity and the activation energy at the grain boundary both effect appreciably the conductivity enhancement. The conductivity for the bulk component is enhanced by the lithium-salt addition, although its activation energy is hardly influenced.

To clarify the mechanism for the enhancement of the bulk conductivity by the salt addition, the sintering temperature was varied (823~1173 K) for the Li_3PO_4 and Li_3BO_3 mixed systems. The conductivity and the sinterability increased with increasing sintering temperature. Figure 2-20 shows the relation between the conductivities of the bulk and the grain boundary components at 298 K for these two systems. The same relation for the $LiTi_2(PO_4)_3$ sample is also shown in the same figure. The conductivities of the bulk component clearly depend on those of the grain boundary. For simplicity, it is assumed that the bulk component is linked in series with the grain boundary component. Lithium ions pass through the grain boundary and then come in the bulk part of the neighboring grain. The lithium ion migration in the grain boundary is a rate-determining step for the ion migration, which was already shown in Figure 2-17. The ion migration at the bulk is limited by that of the grain boundary.

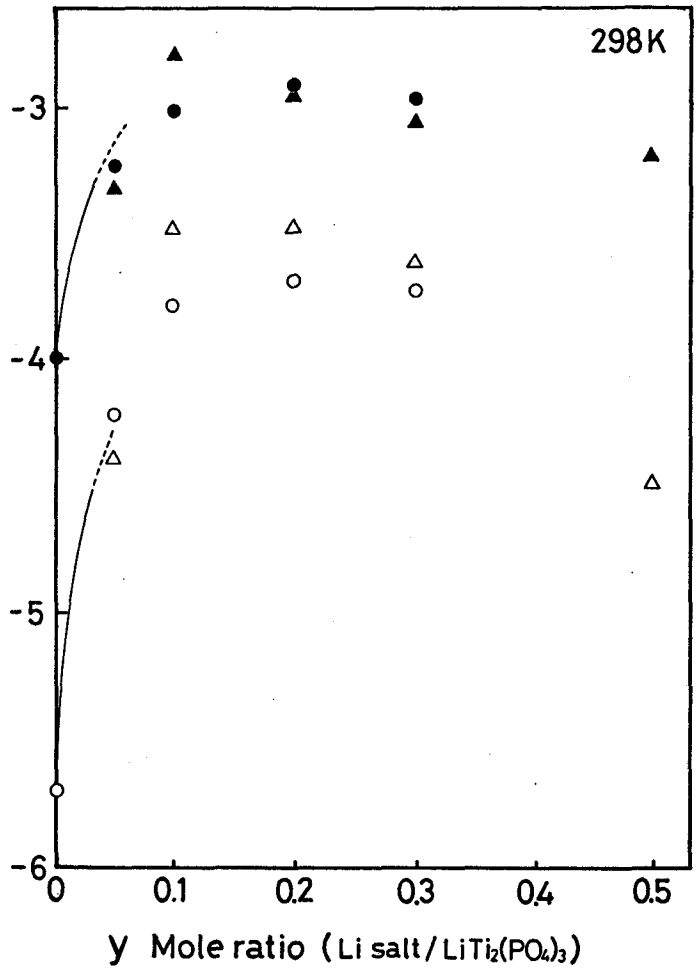

Fig. 2-19. The conductivities of the bulk and the grain boundary at 298 K.
$LiTi_2(PO_4)_3$+yLi_3PO_4; bulk(●), grain boundary(○)
$LiTi_2(PO_4)_3$+yLi_3BO_3; bulk(▲), grain boundary(△)

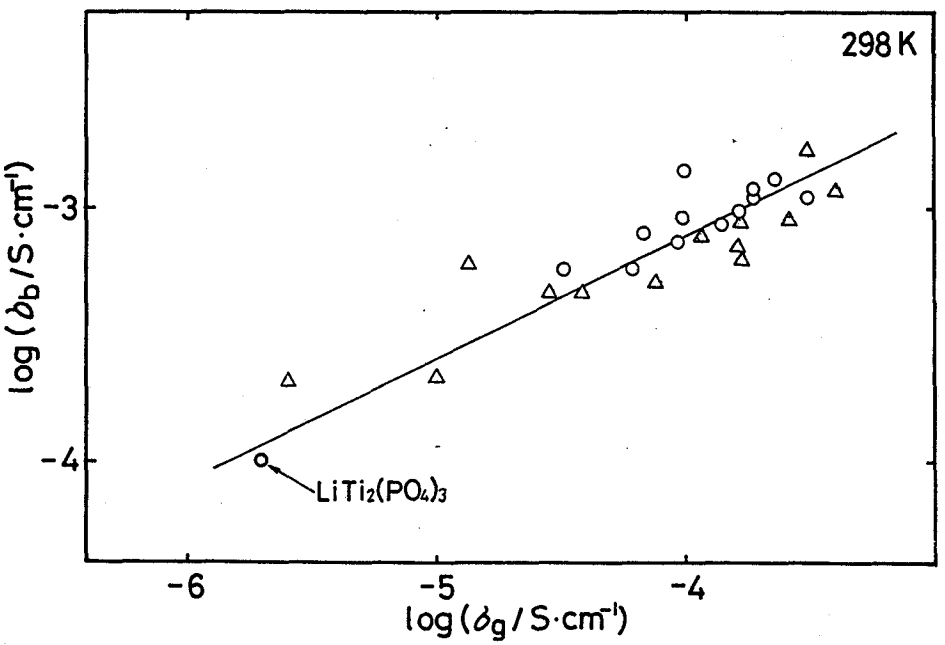

Fig. 2-20. Relationship between the conductivities of the bulk and the grain boundary components at 298 K.
$LiTi_2(PO_4)_3$+yLi_3PO_4 system(○)
$LiTi_2(PO_4)_3$+yLi_3BO_3 system(△)

Thus the bulk conductivity also increase when the ion migration of the grain boundary increases.

2-3-4. The necking model at grain boundary layer

—Sinterability—

Figure 2-21 presents the relationship between the porosity of the sintered pellets and the sintering temperature. For $LiTi_2(PO_4)_3$ itself, a high density pellet could not be prepared by sintering even at high temperature. On the other hand, high density pellets were obtained by the M^{3+} substitution or the coexistence of the lithium compound. Low porosity samples can be formed at around 900 K for the mixed phase group. A higher sintering temperature is necessary to lower the porosity of the single phase group. The sintering temperature for obtaining high density pellet is ca. 1270 K and ca. 1500 K for M=Al and M=Sc, respectively. In the single phase

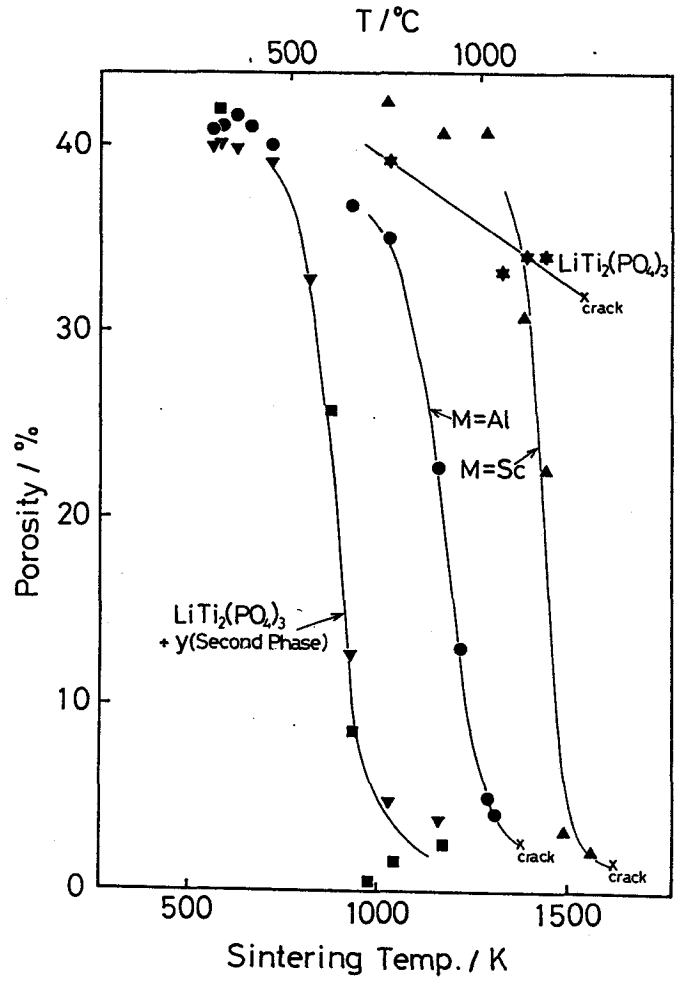

Fig. 2-21. Relationship between the porosity of the sintered pellet and the sintering temperature for $Li_{1.3}M_{0.3}Ti_{1.7}(PO_4)_3$ (M=Al or Sc) single phase system and $LiTi_2(PO_4)_3$+y(second phase) system.
$LiTi_2(PO_4)_3$ (✱)
$Li_{1.3}Al_{0.3}Ti_{1.7}(PO_4)_3$ (●)
$Li_{1.3}Sc_{0.3}Ti_{1.7}(PO_4)_3$ (▲)
$LiTi_2(PO_4)_3$+0.18$Li_3Y_2(PO_4)_3$ (■)
$LiTi_2(PO_4)_3$+0.2Li_3PO_4 (▼)

group, the variety of M^{3+} ion influences the sintering temperature to prepare the high density samples. These results indicate that the sintering process is different between the single phase group and the mixed phase group. For the single phase system, the sinterability of the grain itself is improved by the M^{3+} substitution. In the case of mixed phase system, the second phase would assist the sintering of $LiTi_2(PO_4)_3$.

—Effect of the lithium content—

Table 2-2 lists the electrical properties and the sinterability as a function of the lithium content for $LiTi_2(PO_4)_3$. The lithium content in $LiTi_2(PO_4)_3$ was adjusted by the Li_2CO_3 amount mixed as a starting material. A sample of 100% lithium content means $LiTi_2(PO_4)_3$ itself. The conductivity considerably decreased and the activation energy greatly increased by reducing the lithium content. A lithium deficient layer might be formed at the grain boundary and becomes as a barrier for a Li^+ ionic conduction. On the contrary, the conductivity was greatly enhanced by the increase in the lithium content. This enhancement resulted from the decrease in the porosity and the reduction in activation energy at the grain boundary. The high conductivity and the lower activation energy for a 140% lithium content sample in table 2-2 are very close to those of high conductive samples such as $Li_{1.3}M_{0.3}Ti_{1.7}(PO_4)_3$ (M=Al or Sc) and $LiTi_2(PO_4)_3$+0.$2Li_3PO_4$. The high conductive grain boundary is easily obtained by the excessive lithium content. As a result of it, the lithium content controls the characteristics of the total ionic conductivity of the $LiTi_2(PO_4)_3$ based solid electrolytes.

Table 2-2. The sintering temperature (S.T.), the porosity for the sintered pellet, the electrical properties at the grain boundary vs. the lithium content(%) of $LiTi_2(PO_4)_3$.

Lithium content(%)	S.T. (K)	Porosity (%)	Activation energy (eV)	$\sigma_{298K}(S \cdot cm^{-1})$
96	1393	36.8	0.91	$<10^{-10}$
98	1393	32.2	0.91	$<10^{-10}$
99	1393	33.4	0.52	1.5×10^{-7}
100	1393	34.0	0.48	2.0×10^{-6}
104	1393	33.1	0.47	6.6×10^{-6}
108	1393	13.8	0.36	2.3×10^{-5}
112	1343	14.0	0.38	1.7×10^{-5}
116	1343	12.0	0.37	4.3×10^{-5}
140	1073	4.1	0.36	6.4×10^{-4}

—The necking model at grain boundary layer—

For the bulk component, the activation energy for Li^+ migration is 0.30 eV, which is not influenced by the variation of a lattice size and a lithium insertion in the second site (A(2)) by the increase of lithium content in the $Li_{1+x}M_xTi_{2-x}(PO_4)_3$ system. From the present results, the electrical properties for the $LiTi_2(PO_4)_3$ based ceramic electrolytes are mainly controlled by the condition at the grain boundary.

The necking model for the grain boundary layer is illustrated in Fig. 2-22. In the case of $LiTi_2(PO_4)_3$, a grain boundary shows a high activation energy of 0.48 eV (Fig. 2-22 (a)). The sample obtained has a high porosity and a low conductivity. Furthermore, the conductivity was decreased by the deficiency in the lithium content. For a 2% lithium-poor $LiTi_2(PO_4)_3$ sample, the activation energy for Li^+ migration at

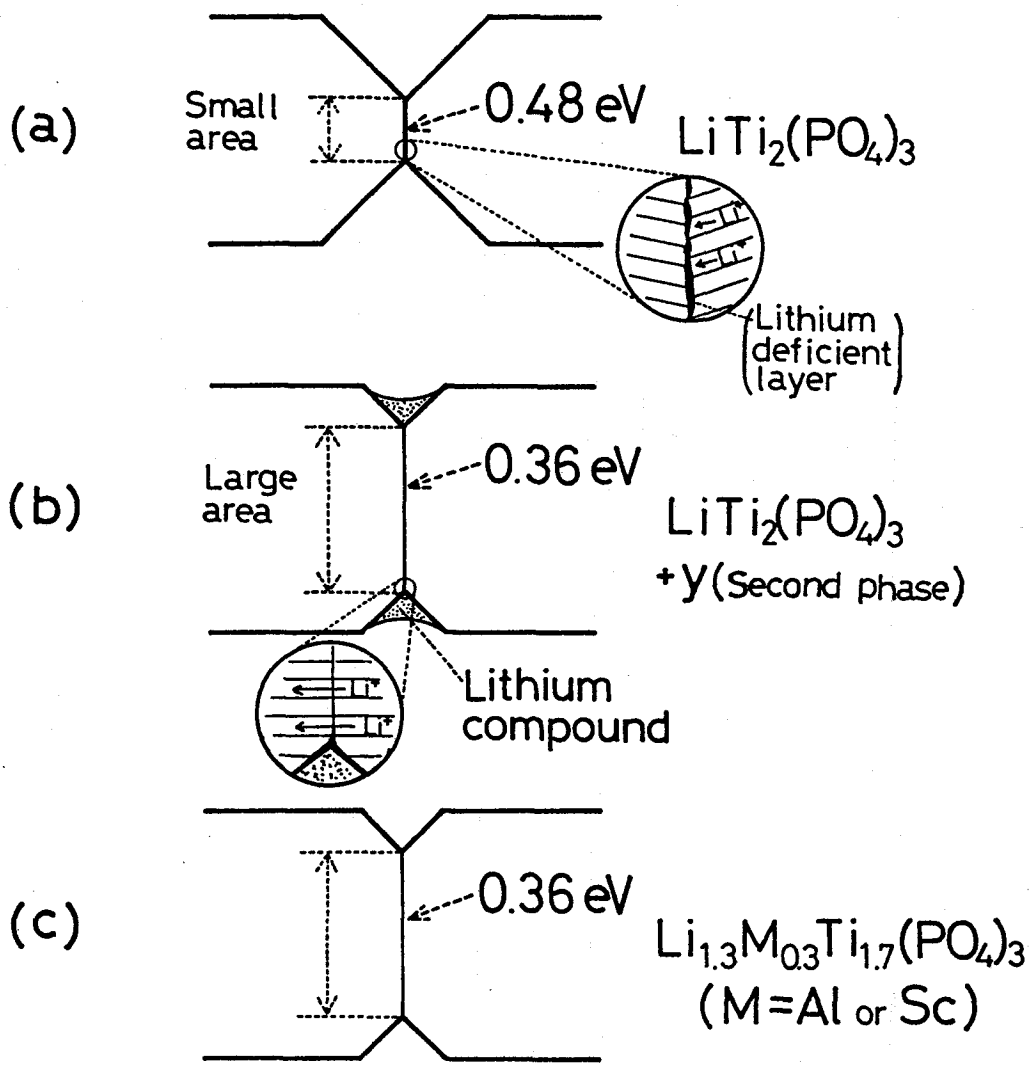

Fig. 2-22. Grain boundary layer necking model.
(a) $LiTi_2(PO_4)_3$
(b) $LiTi_2(PO_4)_3$+y(second phase) mixed phase system
(c) $Li_{1+x}M_xTi_{2-x}(PO_4)_3$ (M=Al, Sc) single phase system

the grain boundary greatly increases to above 0.90 eV. The lithium deficient layer would prevent the electrolyte from sintering and become a barrier for the Li^+ migration. For lithium-excessive samples of $LiTi_2(PO_4)_3$ + y(Lithium compound), a highly-conductive grain boundary layer, whose activation energy

densification was achieved by sintering (Fig. 2-22 (b)). We propose that the lithium compound acts as a flux to obtain a high density pellet. That is to say, the second lithium compound melted by the sintering process and recrystallized the necking between the grains. This assumption is supported by the fact that the sintering temperature for the mixed phase system was lower than that for the single phase system (Fig. 2-21) and the high uniformity among the grains is clearly obtained by the existence of the lithium compound (Fig. 2-14 (e)). As a result of the uniformity, the tunnel for the Li^+ migration comes to be connected by the recrystallization of the grain boundary. In addition, the lithium compound provides the excessive lithium content at the grain boundary, and avoid the formation of the lithium deficient layer.

For $Li_{1+x}M_xTi_{2-x}(PO_4)_3$ (M=Al or Sc) single phase systems (Fig. 2-22 (c)), the high densification occurred at higher sintering temperature compared with the mixed phase system. In this case, the grains sintered without the second phase. The high conductive grain boundary was formed by the solid diffusion during the sintering process. The lithium deficient layer is difficult to form, since lithium content in the $Li_{1+x}M_xTi_{2-x}(PO_4)_3$ systems was eventually increased by the M^{3+} substitution. Although the high densification for the single phase group is performed by the different process compared with the mixed phase group, both groups have a similar ion conductive layer at the grain boundary.

—The vitrification for $LiTi_2(PO_4)_3$—

The vitrification of the polycrystalline electrolyte has

also been attempted to get a solid with high conductivity. The vitreous form is composed of only bulk component and does not possess a low conductive grain boundary. The enhancement of the conductivity by the vitrification was reported for the polycrystalline electrolytes such as $LiNbO_3$ and the $AgI-Ag_2MoO_4$ system.[46-48] The glass samples of $LiTi_2(PO_4)_3$ and $Li_{1.3}Al_{0.3}Ti_{1.7}(PO_4)_3$ were obtained by a rapid quenching method.[49,50] However, the conductivities of them are appreciably lower than those of the polycrystalline electrolytes. The vitreous electrolyte does not hold a suitable tunnel size for Li^+ migration, since a rigid $[Ti_2(PO_4)_3]^-$ skeleton which is appropriate for Li^+ conduction, was considerably destroyed by the rapid quenching.

2-3-5. DC-conductivity with Li metal electrodes

The conductivities in this chapter have been determined by a complex impedance plot with Au blocking electrodes, but not with Li electrodes. In this section, DC conductivity for $Li_{1.3}Al_{0.3}Ti_{1.7}(PO_4)_3$ electrolyte was measured with Li or Li-Al alloy electrodes for the purpose of determining what carrier migrates and interfacial properties between the electrolyte and the electrodes.

The sintered pellet was cut into rod-shaped samples (14 mm, 7x2 mm) for the DC conductivity measurement. The DC conductivity was determined by a two probe method with a Potentiostats-Galvanostats HA-301 from Hokuto Denko Co. and an Electrometer TR-8652 from Advantest Co. Gold leads (dia. 0.05 mm) for the measurement were previously mounted to the sample with an Au

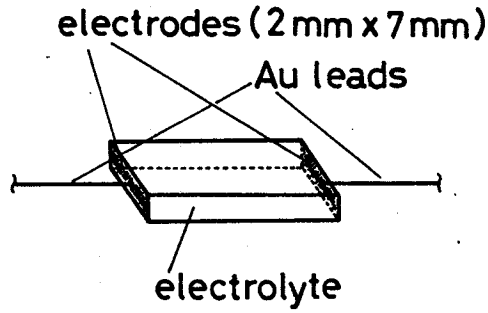

Fig. 2-23. The conductivity measurement.

paste (Fig. 2-23). The rod sample was settled in a vacuum evaporator (HUS-5, Tokyo Vacuum Machinery Co.) and one end of two Au leads was placed outside of the chamber. Li or Li-Al alloy electrodes were deposited by a vacuum evaporation ($<10^{-5}$ Torr) on both cross sections of the sample (Fig. 2-23). In order to prevent a short-circuit between the electrodes by the evaporated metal, the sample surface was beforehandly covered. The measurement of the DC conductivity was conducted in the vacuum evaporator ($<10^{-5}$ Torr) after the sample heated by the electrode evaporation was adequately cooled down to room temperature (ca. 1 h). A four probe method and a complex impedance method were also carried out for the determination of the conductivity.

The conductivity determined by the complex impedance method with an Au blocking electrodes is 1.2×10^{-3} S·cm at 298 K in this study. The DC conductivity variation vs. time at 298 K with the Li or Li-Al alloy electrodes by a two probe method is presented in Fig. 2-24. The result for the four probe method with the Li electrodes is also plotted in the same figure. The conductivity with the Li electrodes by the four probe did not change with the time span measured and is almost the same as that by the complex impedance method. This behavior indicates that lithium ions migrate in the sample. The DC conductivity by the two probe method kept constant value of about 3×10^{-4} S·cm^{-1} for 2 minutes

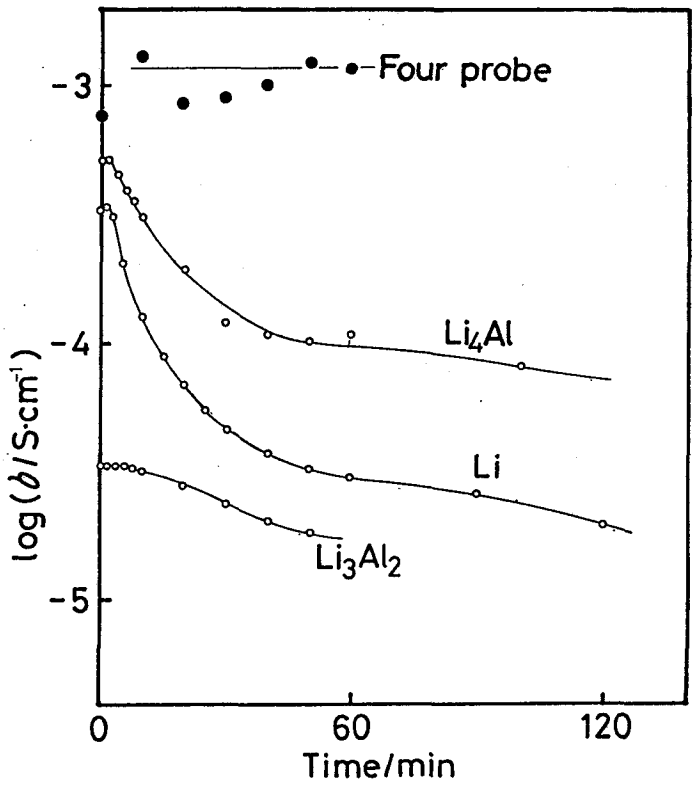

Fig. 2-24. The DC conductivity variation by the two probe method at 298 K with Li and Li-Al alloy electrodes under 0.07 mA/cm^2. (●):the conductivity by the four probe method with Li electrodes.

after the current flow, and the value is lower than the value of 1.2×10^{-3} S • cm^{-1} determined by the complex impedance method. However, the DC conductivity decreased with the further current flow.

Figure 2-25 presents the variation of the cole-cole plots with the Li electrodes. The complex impedance was measured after the DC current was applied for the determined time (0, 20, 40, 80, 180 min.). Before the DC application (0 min.), a smaller semicircle was observed. The DC resistance with Li electrodes and the AC resistance from the cole-cole plot with the blocking electrodes are also indicated on the abscissa. AC and DC resistances are close to the each intersected point of the semicircle to the abscissa. The DC resistance with the Li electrodes is a

total value for bulk, grain boundary, and the electrolyte-electrode interface. The AC resistance with blocking electrodes does not include the interface resistance. The semicircle presented in the figure is ascribed to the contact resistance between the electrodes and the electrolyte, and became progressively greater with the measuring time. The decrement of the DC conductivity using Li electrodes is mainly resulted from the increase in the contact resistance. The decreased DC conductivity did not return to its initial value when an applied potential was reversed. After the DC measurement, the white color for electrolyte surfaces changed to blue. This indicates that Ti^{4+} in $LiTi_2(PO_4)_3$ was reduced to Ti^{3+} by Li metal electrodes. $Li_{1+x}Ti_2(PO_4)_3$ phase would be formed by Li^+ ion insertion in the

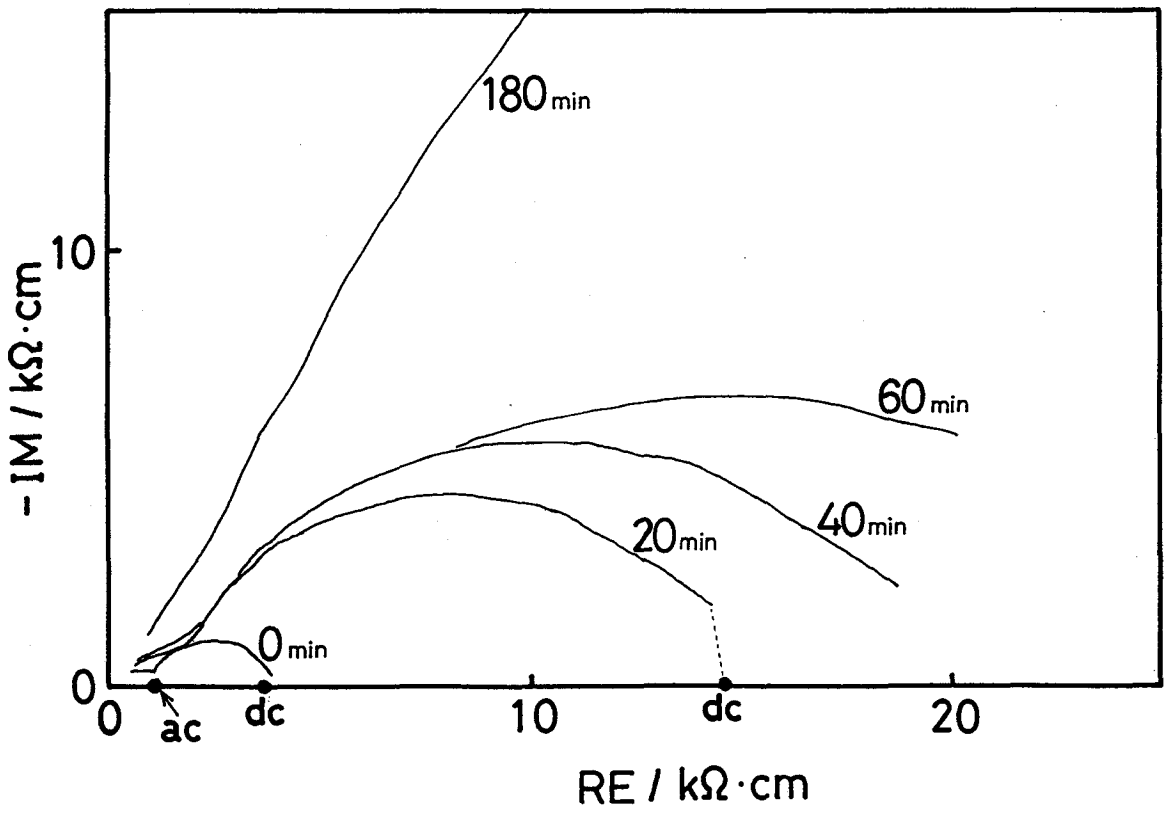

Fig. 2-25. The variation of the cole-cole plots at 298 K using Li electrodes.

$LiTi_2(PO_4)_3$ lattice.[51-53] The conductivity using the Li-Al alloy electrodes was higher than that of Li electrodes (Fig. 2-24). The initial conductivity with the Li_4Al alloy is $5x10^{-4}$ $S \cdot cm^{-1}$ at 298 K. This may be resulted from the easier lithium diffusion in the Li-Al alloy electrodes. Li_3Al_2, a lower Li content alloy gave a lower DC conductivity. A lithium-poor phase would be formed by Li migration on the anode for the lower Li content alloy.

2-4. Summary

$LiTi_2(PO_4)_3$ had poor ionic conductivity and showed high porosity in the sintered pellets. The partial substitution of Ti^{4+} site with M^{3+} in $LiTi_2(PO_4)_3$ was very effective for the enhancement of the conductivity. Mixing the lithium compound such as Li_3PO_4 or Li_3BO_3 with $LiTi_2(PO_4)_3$ is also successful in obtaining a high lithium ionic conductor. The conductivity enhancement by the M^{3+} ion substitution or the binder addition of the lithium salt resulted mainly from the high density of the sintered pellets and decrease the activation energy at grain boundaries. These two factors are clearly correlated with the increase in the total conductivity as well as that across the grain boundaries. The increase of the lithium content at the grain boundary is effective to the conductivity enhancement. The lower conductivity and the sinterability for $LiTi_2(PO_4)_3$ might be ascribed to the formation of the lithium deficient layer at the grain boundary. The excessive lithium content by the addition of the lithium compound with $LiTi_2(PO_4)_3$ leads to form the high conductive grain boundary and highly sintered electrolyte. The added lithium compound acts as a flux for the high density pellet

and the lithium deficient layer can not be formed at the grain boundary. On the other hand, the conductivity and the sinterability are also improved with the x value for the $Li_{1+x}M_xTi_{2-x}(PO_4)_3$ single phase system. In this case, the lithium deficient layer is difficult to form, because the lithium content is increased by the Ti substitution for M^{3+} ion. The Ti^{4+} site replacement in $LiTi_2(PO_4)_3$ with tri-valent cation or the addition of lithium compound to the NASICON-type phosphate electrolyte results in the formation of the high conductive grain boundary and the high dense sintered pellet, and contributes greatly to enhance the total conductivity of the electrolyte.

The maximum conductivity at 298K is $7x10^{-4}$ $S \cdot cm^{-1}$ for $Li_{1.3}M_{0.3}Ti_{1.7}(PO_4)_3$ (M=Al or Sc), which was almost equal to that of Li_3N. The lithium ionic conductors based on lithium titanium phosphate are proved to be excellent solid electrolytes for their high lithium ionic conductivity even at room temperature and a high stability in air. However, these $LiTi_2(PO_4)_3$-based electrolytes can not apply as a material for the lithium battery, because it contains the reducible Ti^{4+} ion by the contact of Li metal electrode.

Chapter 3

Effect of Lattice Size for NASICON-Type Li^+ Ionic Conductor, $LiM_xTi_{2-x}(PO_4)_3$+yLi_2O System (M=Ge, Sn, Hf, and Zr)

3-1. Introduction

$LiM_2(PO_4)_3$ for M=Ge[54], Ti[37-40], Sn, Hf, or Zr[55,56], is a NASICON-type lithium conducting solid electrolyte, whose lattice constant varies with the ionic radius of the M^{4+} cation. The tunnel size for Li^+ migration also changes with the variation of the lattice constant. Since it is important to determine the most suitable lattice size for Li^+ migration, the $LiZr_xTi_{2-x}(PO_4)_3$ system has been studied.[35,55,56] However, these discussions are restricted to the total (bulk plus grain boundary) conductivity of the electrolyte in those papers reported. The electrical properties of the bulk component should be discussed for the determination of the most suitable lattice size for a Li^+ migration, because the total conductivity is influenced by the sintering condition at the grains and the secondary phase appeared at grain boundaries. Since $LiM_xTi_{2-x}(PO_4)_3$ samples show a lower sinterability, their total conductivity should be mainly governed by the conductivity at grain boundaries.

In this chapter, the electrical properties of the bulk and the grain boundaries were examined in detail both for $LiM_2(PO_4)_3$+yLi_2O, M=Ge, Ti, Sn, Hf, and Zr systems and for $LiM_xTi_{2-x}(PO_4)_3$+0.2Li_2O, M=Ge, Sn, Hf, and Zr systems. Correlation between the electrical properties and the lattice constants was studied to determine the most suitable size for Li^+

migration in the NASICON-type structure.

3-2. Experimental

—Materials—

A stoichiometric mixture of Li_2CO_3 (99.99%), MO_2 (M=Ge, Ti, Sn, Hf, Zr) (99.9% or 99.99%), and $(NH_4)_2HPO_4$ (extra pure grade) was ground in an agate mortar and then heated at 1173 K for 2 h in a platinum crucible. The Li_2CO_3 and $(NH_4)_2HPO_4$ is decomposed into Li_2O and P_2O_5 by this heat treatment. The excess amount of Li_2O in $LiM_xTi_{2-x}(PO_4)_3+yLi_2O$ systems was controlled by that of Li_2CO_3 as a starting material. The resulting material was ground into a fine powder using a ball-mill for 6 h by a wet process with methanol. The weight ratio of methanol/sample is ca. 10. The dried powder was reheated at 1173 K for 2 h and then ball-milled again for 12 h. The mixture of the dried powder and a proper amount of 3% polyvinyl-alcohol solution as a binder was pressed into a pellet at a pressure of $1x10^8$ Pa. The pellets were sintered at 1073, 1173, or 1293 K in air. The surfaces of the sintered pellet were polished with an 800-grade emery paper and gold was deposited as electrodes by a sputtering method (Shimadzu IC-50). After the conductivity measurement was conducted for all the samples with different sintering temperature, the optimum sample was chosen in such a way that the highest conductivity was obtained at room temperature. A quantitative analysis of Li in the sintered sample was carried out by an atomic absorption analysis.

—Measurement—

The measurements for the conductivity, the porosity, and the X-ray diffraction analysis are same as those of described in chapter 2.

3-3. Results and Discussion

3-3-1. $LiM_2(PO_4)_3+yLi_2O$, M=Ge, Ti, Sn, Hf, or Zr system

—Phase—

For the $LiM_2(PO_4)_3+yLi_2O$ samples, only the $LiM_2(PO_4)_3$ phase was clearly confirmed by the X-ray powder diffraction analysis. The Li content was found to remain constant during the sintering process for every system, which was confirmed by the atomic absorption method. The Li_2O compound exists at grain boundaries as a glassy phase of Li_2O or lithium phosphate.

Lattice parameters are determined for the $LiM_2(PO_4)_3+yLi_2O$, M=Ge, Ti, Sn, Hf, and Zr systems. The lattice constant did not change with y for $LiM_2(PO_4)_3+yLi_2O$ systems, and these of $LiM_2(PO_4)_3$ (y=0) are presented in Table 3-1. This means that the A_2 sites are not occupied by Li^+ ions. The NASICON-type rhombohedral structure was obtained for $LiM_2(PO_4)_3$, M=Ge, Ti, and Hf systems and the lattice parameters depend on the ionic radius[43] of those M^{4+} ions. In the case of M=Hf system, the sintering temperature needs to be higher than ca. 1200 K to obtain a rhombohedral structure. The monoclinic phase was obtained for the samples sintered at below ca. 1200 K. On the other hand, monoclinic crystal formed for $LiM_2(PO_4)_3$, M=Sn and Zr series. For M=Sn samples, the monoclinic <—> rhombohedral

transition was observed at around 410 K from DSC (differential scanning calorimeter) measurement and by high temperature X-ray analysis.

Table 3-1. Lattice parameters (hexagonal unit) for $LiM_2(PO_4)_3$+yLi_2O, M=Ge, Ti, Sn, Hf, and Zr.

Sample	Ionic radius of M^{4+} (Å)	Lattice constant a(Å)	c(Å)	Cell volume Å^3	Phase
$LiGe_2(PO_4)_3$	0.540	8.287	20.475	1218	R
$LiTi_2(PO_4)_3$	0.605	8.512	20.858	1309	R
$LiSn_2(PO_4)_3$	0.690	-	-	-	M, R(>410K)
$LiHf_2(PO_4)_3$	0.710	8.824	22.04	1486	R
$LiZr_2(PO_4)_3$	0.720	-	-	-	(M)

R: Rhombohedral, M: Monoclinic

—Conductivity and sinterability—

The relationship between the porosity and y for the sintered ceramics in $LiM_2(PO_4)_3$+yLi_2O series is plotted in Fig. 3-1. A high density pellet can not be obtained for $LiM_2(PO_4)_3$ (y=0). The porosity decreased appreciably with increased y for all the systems examined. Li_2O addition is quite effective for obtaining a high density pellet.

Figure 3-2 shows the relationship between the total conductivity at 298 K and y for the $LiM_2(PO_4)_3$+yLi_2O, M=Ge, Ti, Sn, Hf, and Zr systems. The conductivity is greatly enhanced by the Li_2O addition for all of the $LiM_2(PO_4)_3$ samples, and a maximum conductivity was obtained at around y=0.2. The monoclinic systems of M=Sn or Zr show a lower conductivity because of their distorted structure. The conductivity decreased with the addition of excess Li_2O for y>0.3. The low conductivity for Li_2O or lithium phosphate influenced the ion migration at the grain boundary. Figure 3-3 shows a representative complex

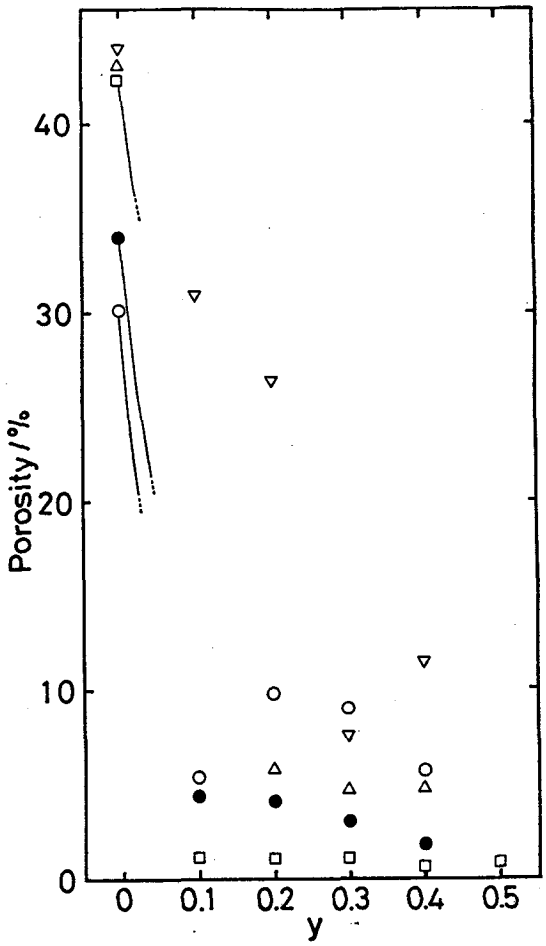

Fig. 3-1. Relationship between the porosity of the sintered pellets and y for $LiM_2(PO_4)_3+yLi_2O$, M=Ge(○), Ti(●), Sn(▽), Hf(△), and Zr(□).

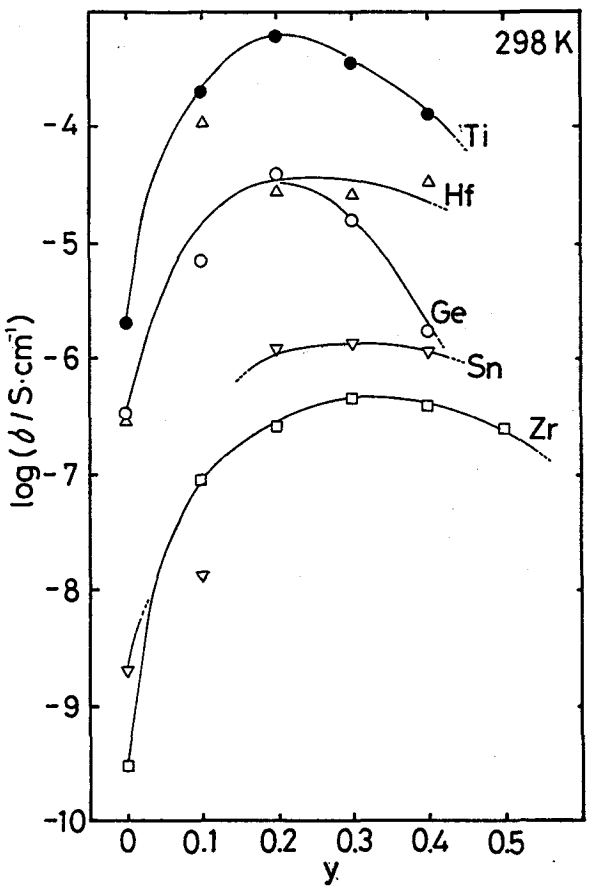

Fig. 3-2. Total conductivity at 298 K vs. y value for $LiM_2(PO_4)_3+yLi_2O$, M=Ge(○), Ti(●), Sn(▽), Hf(△), and Zr(□).

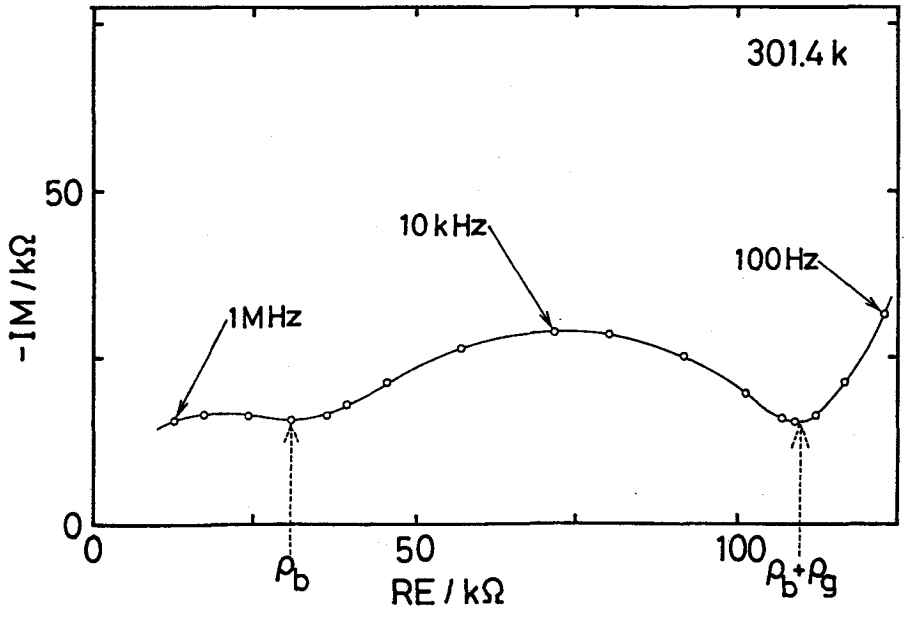

Fig. 3-3. Complex impedance plot (Cole-Cole Plot) for $LiGe_2(PO_4)_3+0.1Li_2O$ at 301.4 K.

impedance plot for $LiGe_2(PO_4)_3$+0.1Li_2O at 301.4 K. The bulk and the total (bulk plus grain boundary) resistances were determined from two semicircles as shown in the figure.[44,45] The bulk resistivity ρ_b and the total resistivity $\rho_b+\rho_g$ were determined from the intersected points of the semicircles to the abscissa in higher- and lower- frequency regions, respectively. Third large semicircle corresponding to the interfacial resistance between the Au electrode and the electrolyte was also observed in the lower frequency region. This semicircle is clearly observed when the temperature was increased.

Figure 3-4 plots the activation energy of bulk and grain boundaries components for $LiM_2(PO_4)_3$+yLi_2O, M=Ge(a), Ti(b), and Hf(c). For the M=Sn and Zr systems, the activation energy could not be determined, since the only one semicircle was observed in the complex impedance plots. The activation energy for the grain boundaries decreases with y for the systems of M=Ge(a), M=Ti(b), and M=Hf(c). The conductivity enhancement is attributed to the decrease in the activation energy at grain boundaries. The activation energy for the bulk component remains constant with the Li_2O addition for all the systems. The activation energy for the bulk component has been estimated to be ca. 0.38 eV for $LiGe_2(PO_4)_3$ and ca. 0.30 eV for $LiTi_2(PO_4)_3$. In the case of M=Hf system, the activation energy for bulk and grain boundaries could be determined for y=0, 0.1 and 0.2 samples because two semicircles were obtained only for these three samples. The activation energy of the bulk component estimated to be 0.42 eV for $LiHf_2(PO_4)_3$. The higher activation energy for Li^+ migration comes from the smaller lattice size in $LiGe_2(PO_4)_3$ and from the larger lattice size in $LiHf_2(PO_4)_3$ compared with that in

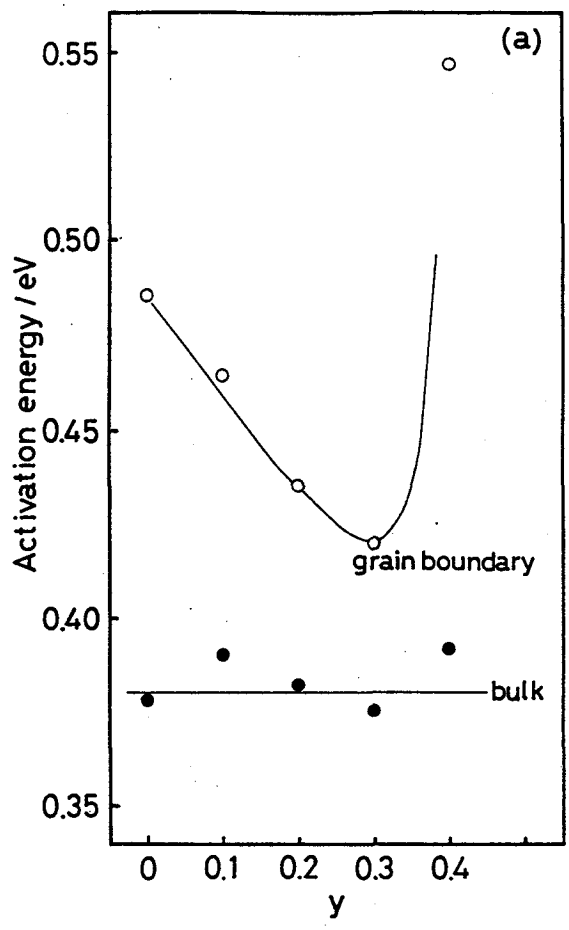

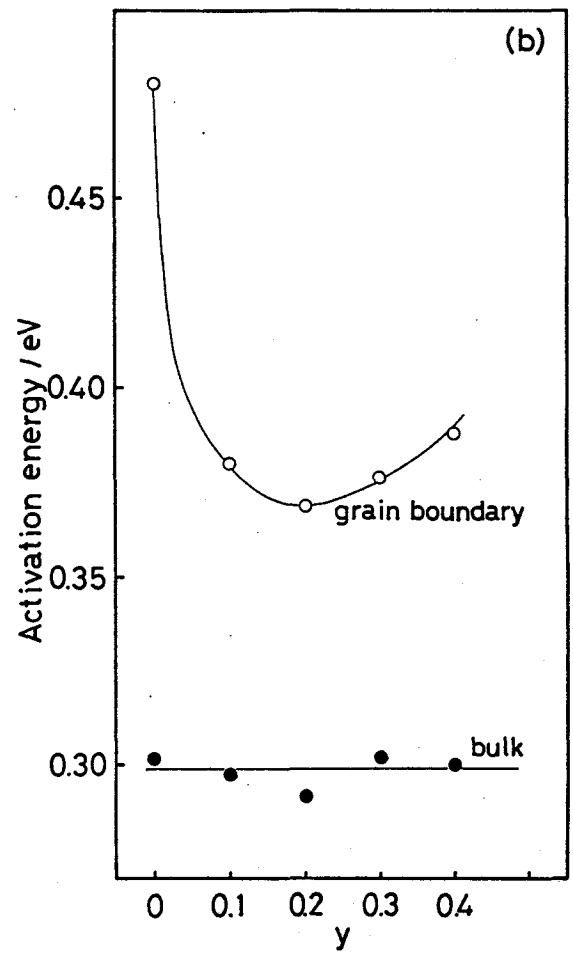

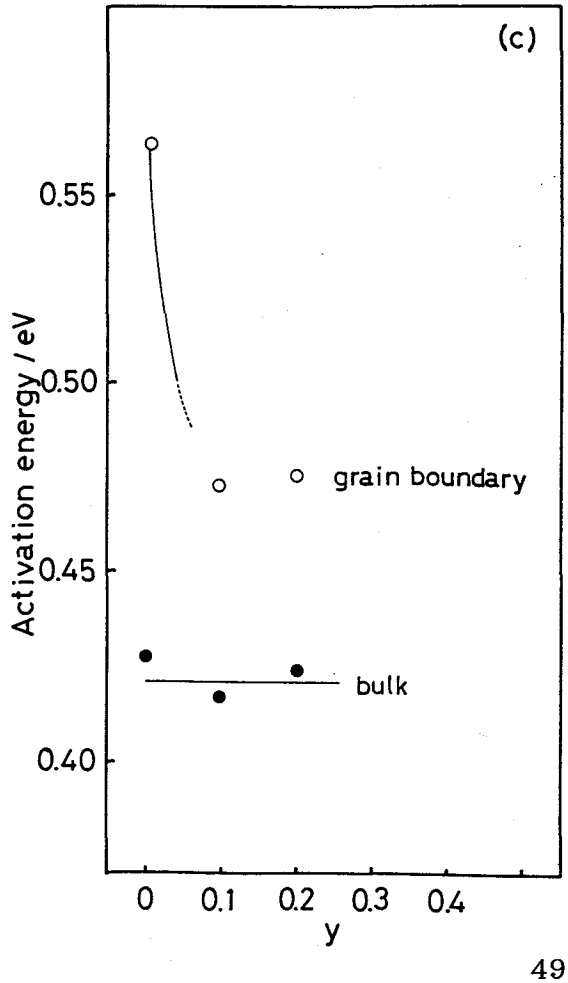

Fig. 3-4. Activation energy for the Li^+ migration at bulk and grain boundaries vs. y for the $LiM_2(PO_4)_3+yLi_2O$ system.
(a)$LiGe_2(PO_4)_3+yLi_2O$
(b)$LiTi_2(PO_4)_3+yLi_2O$
(c)$LiHf_2(PO_4)_3+yLi_2O$
bulk (●), grain boundaries (○)

$LiTi_2(PO_4)_3$.

Figure 3-5 presents the model for the sintering process. This process for $LiTi_2(PO_4)_3$-based electrolytes was already described in chapter 2. This model can apply for all the NASICON-type electrolytes. The added Li_2O acts as a flux at the grain boundaries. The lithium phosphate is formed at the grain boundaries during the heating process, and then the surface of grains are melted and recrystallized by the flux. The remaining flux fills pores in the sintered $LiM_2(PO_4)_3$ solid with a glassy phase. For $LiM_2(PO_4)_3$, a low lithium content at the grain boundaries lowered the sinterability. For the $LiM_2(PO_4)_2$+yLi_2O systems, the lithium compound addition in $LiM_2(PO_4)_3$ ceramics is effective to accelerate the sintering process and to enhance the conductivity at grain boundaries.

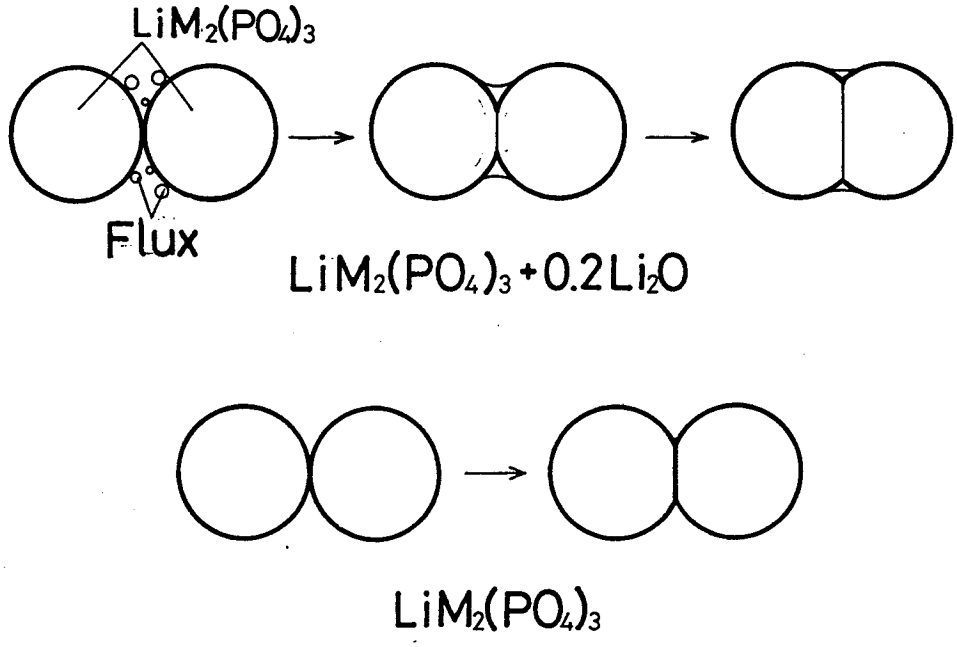

Fig. 3-5. Model for sintering process.

3-3-2. $LiM_xTi_{2-x}(PO_4)_3+0.2Li_2O$ M=Ge, Sn, Hf, and Zr systems

—Lattice parameters—

The relationship between the lattice size and electrical properties was investigated for the NASICON-type Li^+ ionic conductor. The Li_2O was fixed at y=0.2 for $LiM_xTi_{2-x}(PO_4)_3+yLi_2O$ systems. The porosity was lower than 10 % for all the y=0.2 pellets examined. Figure 3-6 shows the variation of the lattice

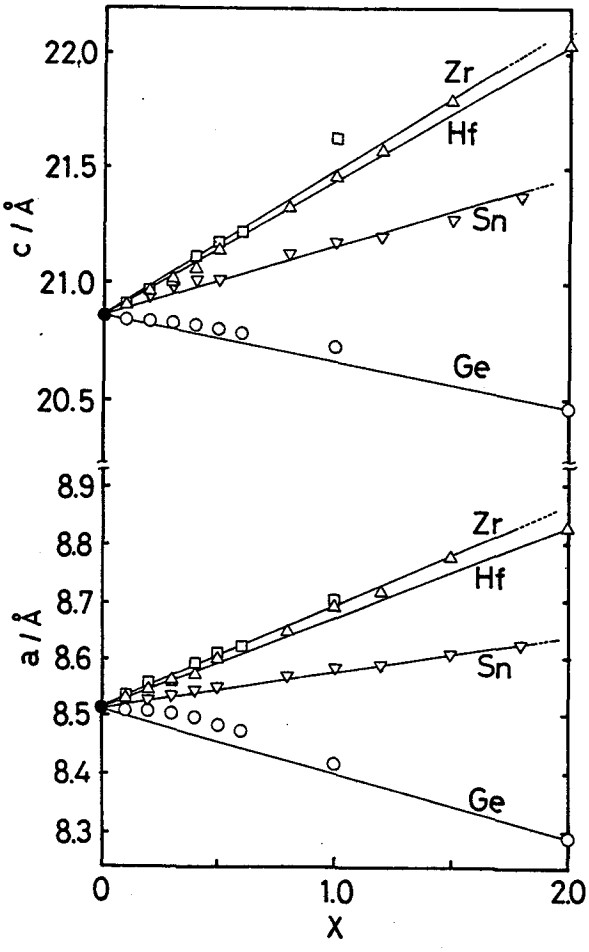

Fig. 3-6. Variation of the lattice constants (hexagonal unit) on x for $LiM_xTi_{2-x}(PO_4)_3+0.2Li_2O$, M=Ge(○), Sn(▽), Hf(△), and Zr(□).

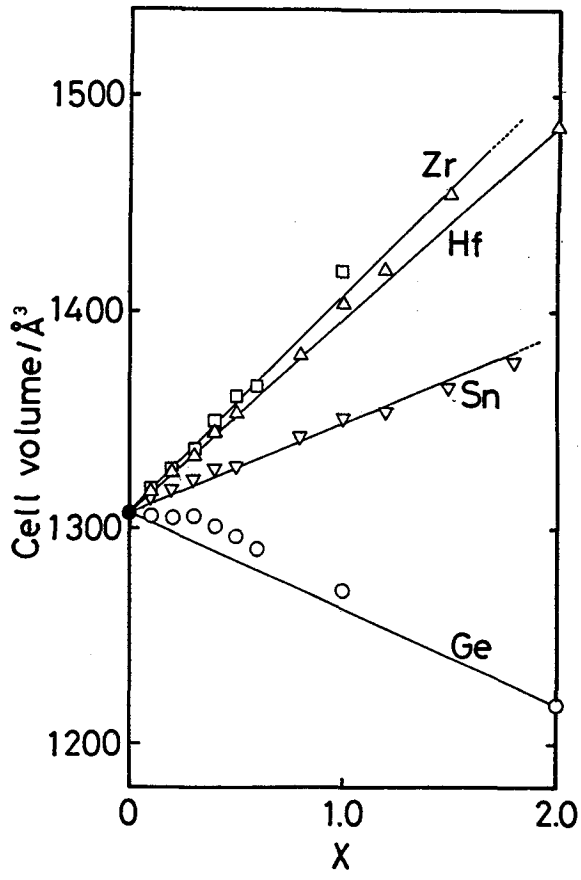

Fig. 3-7. Variation of the cell volume (hexagonal unit) on x for $LiM_xTi_{2-x}(PO_4)_3+0.2Li_2O$, M=Ge(○), Sn(▽), Hf(△), and Zr(□).

constants with x for $LiM_xTi_{2-x}(PO_4)_3$+0.2Li_2O M=Ge, Sn, Hf, and Zr hexagonal systems. The NASICON type structure was obtained for the samples except for $LiM_2(PO_4)_3$+0.2Li_2O, M=Sn or Zr. The lattice constants decreased when Ti^{4+} in $LiTi_2(PO_4)_3$ was substituted for the smaller Ge^{4+} ion. In the systems substituted with the larger Sn^{4+}, Hf^{4+}, or Zr^{4+}, the lattice constants increased with the M^{4+} amount. The cell volume calculated from the lattice constants, is also plotted as a function of x in Fig. 3-7. The variation of the cell volume with x is quite similar to that of the lattice constant for both a- and c-axes.

—The electrical properties vs. the cell volume—

Figure 3-8 presents the total conductivity at 298 K vs. x for $LiM_xTi_{2-x}(PO_4)_3$+yLi_2O, M=Ge, Sn, Hf, and Zr systems. The samples for x=0~0.5 (M=Ge, Sn, and Hf) showed almost a constant conductivity (about 5×10^{-4} $S \cdot cm^{-1}$). Further Ti^{4+} site substitution made the conductivity decrease. A higher conductivity is obtained when the ionic radius of the M^{4+} ion is close to that of Ti^{4+} ion. A maximum conductivity of 8×10^{-4} $S\cdot cm^{-1}$ was obtained for $LiGe_{0.2}Ti_{1.8}(PO_4)_3$+0.2$Li_2O$ at 298 K. The conductivity is considerably lower for the monoclinic samples of $LiM_2(PO_4)_3$+0.2Li_2O, M=Sn or Zr, which corresponds to the complete Ti^{4+} site replacement with Sn^{4+} or Zr^{4+}. Figure 3-9 shows the relationship between the total conductivity at 298 K and the cell volume for the samples with $R\bar{3}c$ structure. The maximum conductivity was obtained around 1310 $Å^3$. As mentioned above, the total conductivity is influenced by the sinterability and the existence of the secondary phase at the grain boundaries.

To confirm the correlation between the electrical properties

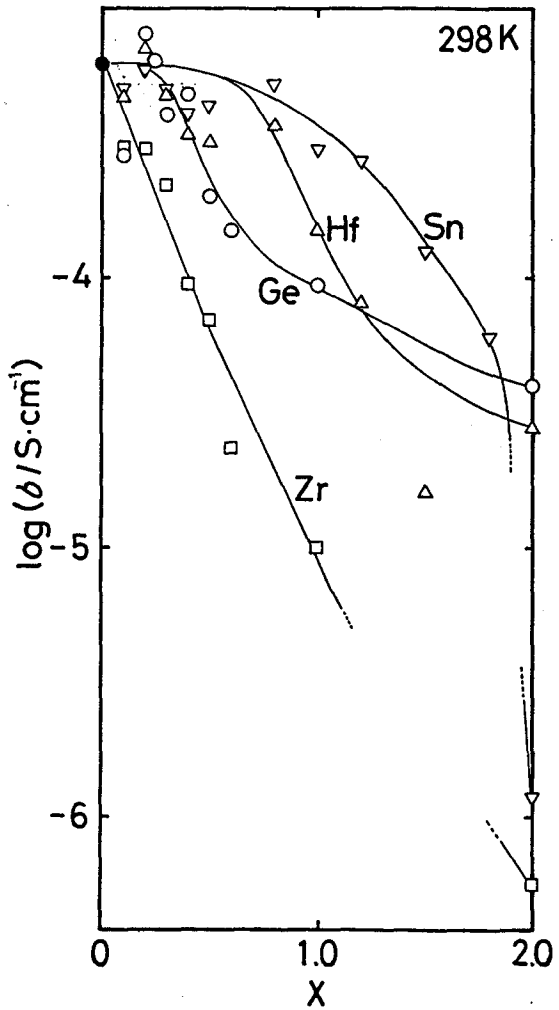

Fig. 3-8. Variation of the total conductivity at 298 K on x for $LiM_xTi_{2-x}(PO_4)_3+0.2Li_2O$, M=Ge(○), Sn(▽), Hf(△), and Zr(□).

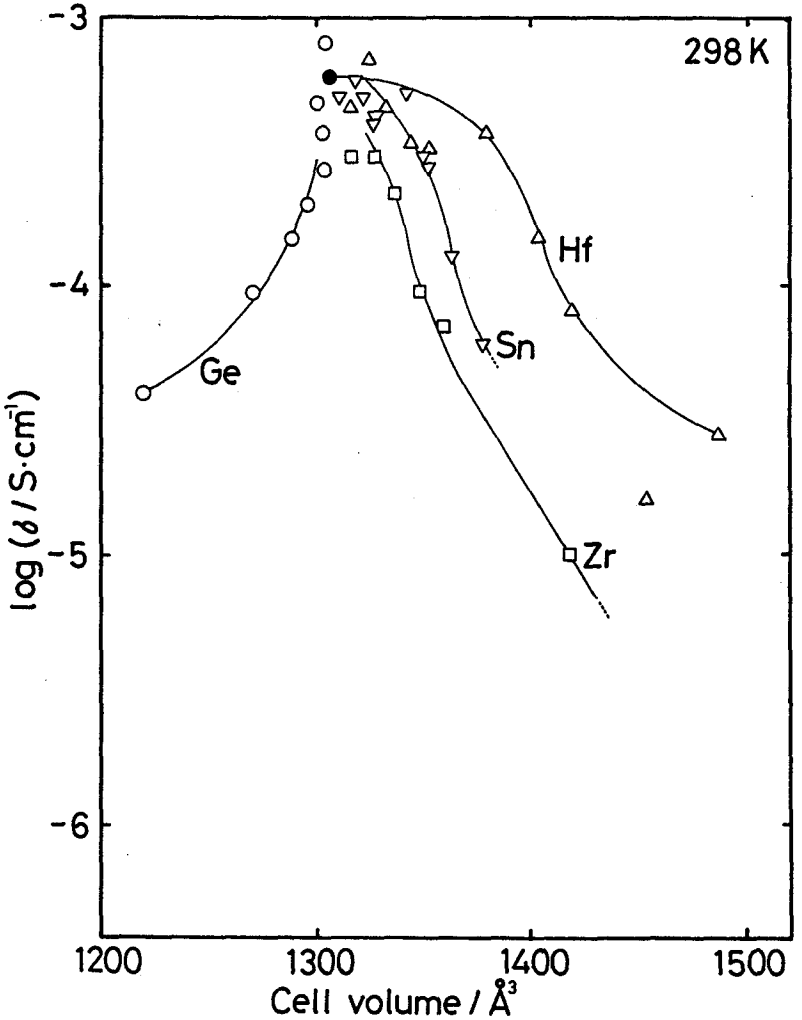

The. 3-9. Relationship between the total conductivity and the cell volume for $LiM_xTi_{2-x}(PO_4)_3+0.2Li_2O$, M=Ge(○), Sn(▽), Hf(△), and Zr(□).

of the bulk component and the cell volume, the activation energy for Li^+ migration in the bulk component was determined by the complex impedance method. Figure 3-10 shows the variation of the activation energy for the bulk component with x. The activation energy for x=0~0.5 is constant, i.e. 0.28~0.30 eV, and then increases with the further M^{4+} substitution. For several samples x>1.0 (M=Sn), 1.2<x<2.0 (M=Hf), and x>0.3 (M=Zr) in $LiM_xTi_{2-x}(PO_4)_3$+0.2Li_2O systems, the activation energy for the bulk component could not be determined because two semicircles in the complex impedance plots could not be clearly obtained.

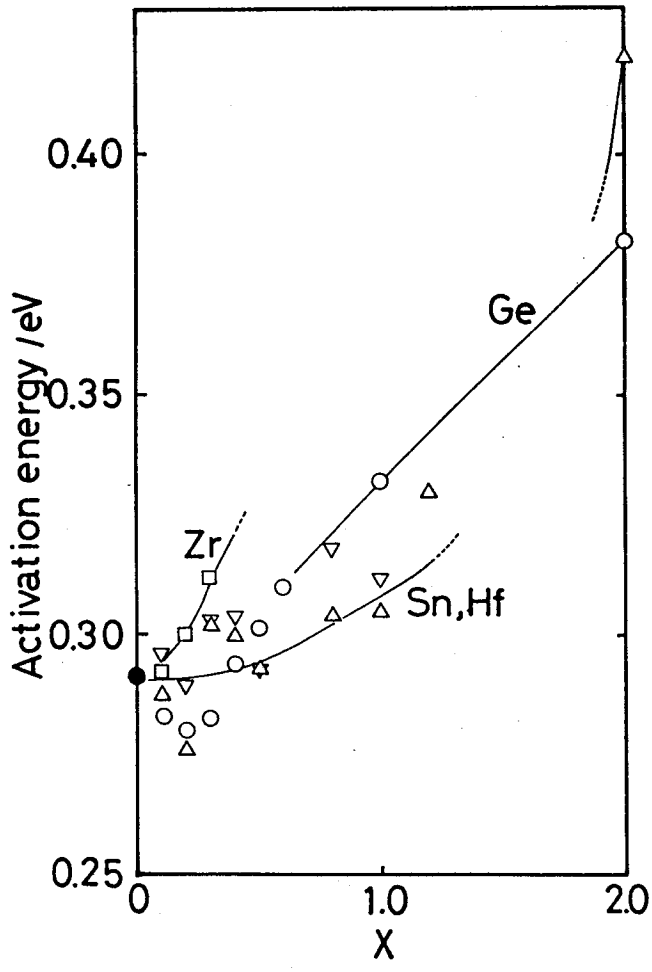

Fig. 3-10. Variation of the activation energy for the bulk component on x for $LiM_xTi_{2-x}(PO_4)_3$+0.2Li_2O, M=Ge(○), Sn(▽), Hf(△), and Zr(□).

The relationship between the activation energy for the bulk and the cell volume is presented in Fig. 3-11 The region of the lower activation energy is relatively wide from 1290 $Å^3$ to 1400 $Å^3$. A minimum activation energy is observed for the samples of the cell volume ca. 1310 $Å^3$ (lattice constants a=8.51 Å and c=20.86 Å). The activation energy for Li^+ migration increases when the cell volume is smaller or larger than 1310 $Å^3$. Li^+ ion is small ionic radius and has large Li^+-O bonding energy. We consider that Li^+ would shift toward edge from center in the tunnel when the lattice size is too large. This clearly indicates that $LiTi_2(PO_4)_3$ has the most suitable tunnel size for Li^+ migration with an activation energy of 0.28~0.30 eV.

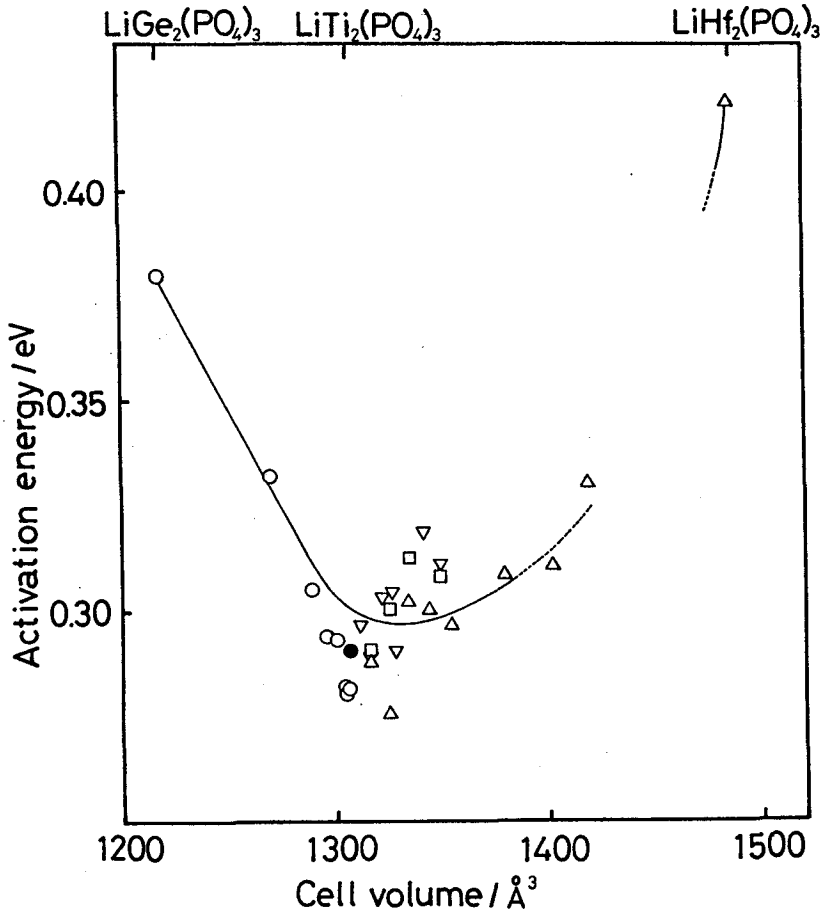

Fig. 3-11. Relationship between the activation energy for the bulk component and the cell volume for $LiM_xTi_{2-x}(PO_4)_3+0.2Li_2O$, M=Ge(○), Sn(▽), Hf(△), and Zr(□).

3-4. Summary

The conductivity and the sinterability increased with Li_2O addition in $LiM_xTi_{2-x}(PO_4)_3+yLi_2O$, M=Ge, Sn, Hf, and Zr systems. The excess Li_2O acts as a flux to obtain a highly conductive layer at the grain boundaries. A minimum activation energy for the bulk component for the NASICON-type Li^+ conductor is 0.28~0.30 eV with the cell volume of 1310 $Å^3$, which corresponds exactly to the lattice size of $LiTi_2(PO_4)_3$. The smaller and the larger lattice sizes compared to the size of $LiTi_2(PO_4)_3$ increases the activation energy appreciably. A maximum conductivity was obtained for the cell volume of ca. 1310 $Å^3$.

Chapter 4

The Electrical Properties for $LiGe_2(PO_4)_3$- and $LiHf_2(PO_4)_3$-based Solid Electrolytes

4-1. Introduction

In chapter 2, solid electrolytes based on $LiTi_2(PO_4)_3$, the $Li_{1+x}M_xTi_{2-x}(PO_4)_3$, M=Al, Sc, Y, or La, etc. system, or the $LiTi_2(PO_4)_3$+y(lithium salt) system, have presented to show high conductivity at room temperature. Although $LiTi_2(PO_4)_3$ shows poor conductivity, it could be greatly enhanced by M^{3+} substitution or the addition of a lithium salt, such as Li_3PO_4 or Li_3BO_3. $LiM_2(PO_4)_3$, where M^{4+} are Ge, Sn, Hf, and Zr, are the analogue electrolyte. However, the conductivity for these phosphates is lower compared with those for the $LiTi_2(PO_4)_3$ series. $LiTi_2(PO_4)_3$ is supposed to form the best host structure, since the tunnel size in the phosphate is suitable for Li^+ ion migration (chapter 3). A minimum activation energy of 0.28~0.30 eV for a bulk component was obtained for the Li^+ conductors based on $LiTi_2(PO_4)_3$. However, the $LiTi_2(PO_4)_3$-based electrolytes contain the reducible Ti^{4+} ion with the contact of Li metal electrode (see 2-3-5). These Ti-based materials can not apply to the electrolyte for the lithium battery.

$LiGe_2(PO_4)_3$ and $LiHf_2(PO_4)_3$ can expect to apply as the electrolyte for high energy density batteries because of the stability for Ge^{4+} and Hf^{4+} ions. For $LiSn_2(PO_4)_3$ and $LiZr_2(PO_4)_3$ series, the rhombohedral structure was distorted to monoclinic one at room temperature (chapter 3). The lattice constants for

$LiGe_2(PO_4)_3$ are smaller than those for $LiTi_2(PO_4)_3$. If the Ge^{4+} site is partially substituted by a larger M^{3+} ion, the tunnel size may be expected to approach that of $LiTi_2(PO_4)_3$. Although Li et al. have reported that the conductivity increases with the value of x for the $Li_{1+x}M_xGe_{2-x}(PO_4)_3$, $M^{3+}=Al^{3+}$ (0.535Å) and Cr^{3+} (0.615Å) systems,[54] whose ionic radii are close to that of Ge^{4+} (0.530Å), no other cation has been tried regarding substitution. On the other hand, up to now, the larger lattice size system of $LiHf_2(PO_4)_3$-based electrolytes has not been investigated.

In this chapter, the electrical properties and the crystal structure were examined for the NASICON-type solid electrolytes based on $LiGe_2(PO_4)_3$ and $LiHf_2(PO_4)_3$, i.e. the $Li_{1+x}M_xGe_{2-x}(PO_4)_3$ (M=Al, Cr, Ga, Fe, Sc, or In) system and the $Li_{1+x}M_xHf_{2-x}(PO_4)_3$ (M=Cr, Fe, Sc, In, Lu or Y) system.

4-2. Experimental

Li_2CO_3 (purity:99.99%), GeO_2 (99.999%), HfO_2 (99.9%), $(NH_4)_2HPO_4$ (extra pure grade), and M_2O_3 M=Al, Cr, Ga, Fe, Sc, In, Lu, Y (99.9% or 99.99%) were used as starting materials. The detail of the sample preparation and the measurements has been described in the chapter 3.

3-3. Results and discussion

3-3-1. $LiGe_2(PO_4)_3$-based electrolyte

—Phase—

Figure 4-1 shows the relationship between the ionic radius

of the M^{3+} ion and the cell volume for $Li_{1.5}M_{0.5}Ge_{1.5}(PO_4)_3$. The cell volume was estimated from the lattice constants obtained by the X-ray powder diffraction method. The broken line corresponds to the cell volume calculated based on the assumption that the M^{3+} ion completely substitutes the Ge^{4+} site. Figure 4-2 presents the X-ray diffraction patterns for samples of $Li_{1.5}M_{0.5}Ge_{1.5}(PO_4)_3$, M=Al, Cr, Ga, Fe, Sc, or In. The $LiGe_2(PO_4)_3$ pattern is also shown as a reference. For the Al^{3+} and Cr^{3+} systems, the cell volume is close to the calculated value; only the $R\bar{3}c$ phase has been confirmed by X-ray diffraction analyses. The Al^{3+} and Cr^{3+} ions easily substitute the Ge^{4+} site, since these M^{3+} ions are close to Ge^{4+} regarding the ionic radius. The tunnel size increases, if the Ge^{4+} site is

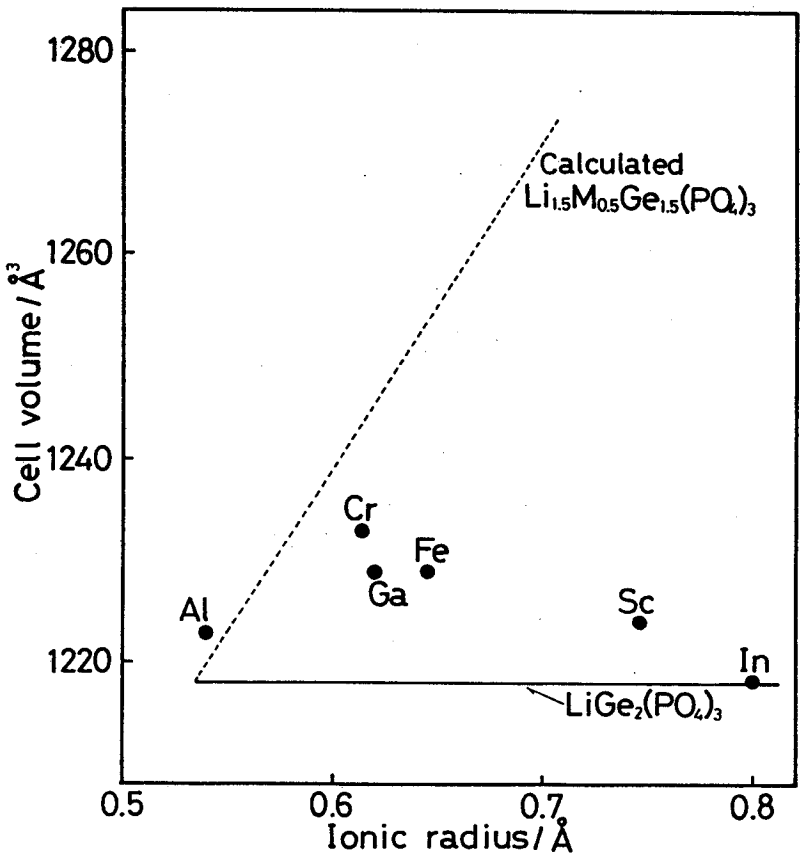

Fig. 4-1. Relationship between the M^{3+} ionic radius and the cell volume for $Li_{1.5}M_{0.5}Ge_{1.5}(PO_4)_3$.

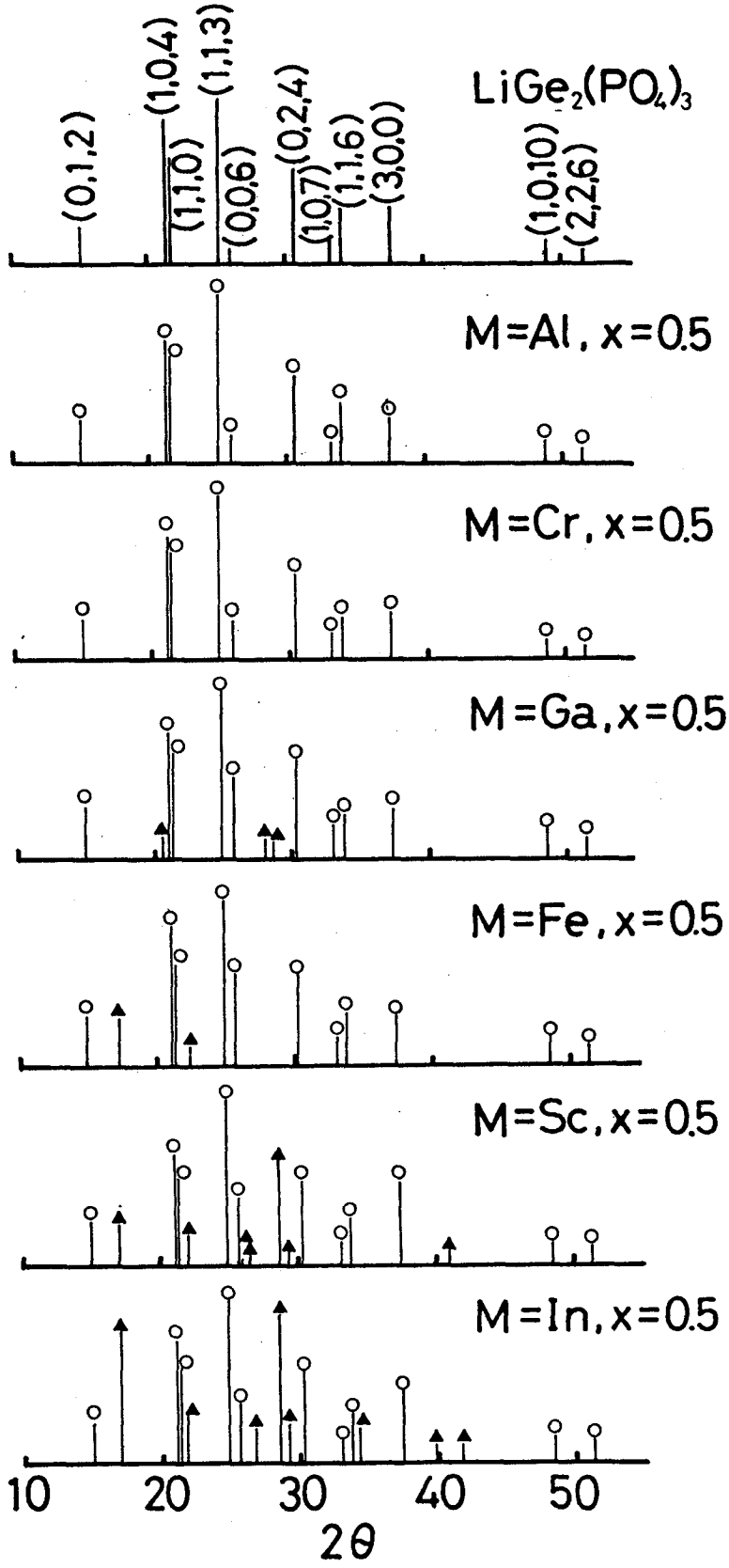

Fig. 4-2. X-ray diffraction patterns (Cu-Kα) for $LiGe_2(PO_4)_3$ and $Li_{1.5}M_{0.5}Ge_{1.5}(PO_4)_3$, M=Al, Cr, Ga, Fe, Sc, or In. NASICON-type phase (○), unknown phase (▲)

substituted by a larger M^{3+} ion. We expected that the cell volume would increase upon substitution of the Ge^{4+} site by larger M^{3+} ions, such as Fe^{3+} or Sc^{3+}. However, the obtained cell volume is lower than the calculated one. This cell volume did not increase if the sintering temperature is raised. The Ge^{4+} ion in $LiGe_2(PO_4)_3$ can not be easily substituted by a larger M^{3+} ion. The cell volume for the In^{3+} system is the same for that of $LiGe_2(PO_4)_3$. This indicates that no replacement occurs for the larger In^{3+} system. On the other hand, some unknown peaks were also observed for the Ga^{3+}, Fe^{3+}, Sc^{3+}, In^{3+} systems. The number of the unknown peaks and the intensity of these peaks increase with an enlargement in the ionic radius of the M^{3+} ion. The second phase would be obtained, since the replacement of the Ge^{4+} site is difficult for these larger M^{3+} ions. These unknown peaks were not assigned to the $Li_3M_2(PO_4)_3$ phase, M=Ga, Fe, Sc, In.

—Conductivity and sinterability—

Figure 4-3 shows the relationship between the conductivity and x for the $Li_{1+x}M_xGe_{2-x}(PO_4)_3$ systems at 298 K. The conductivity is greatly enhanced along with the increase in x for all of the systems examined. In particular, the conductivity for the Al^{3+} and Cr^{3+} systems is higher than that for the other systems. A maximum conductivity of 2.4×10^{-4} $S \cdot cm^{-1}$ was obtained for $Li_{1.5}Al_{0.5}Ge_{1.5}(PO_4)_3$, which is about one order of magnitude higher than that reported by Li et al.[54] In this study, the particle size of the ball-milled powders before sintering was smaller than 1 μm. However, the well-ground process was not described in the paper of by Li et al. The difference in the grinding process would influence both the conductivity and

sinterability. By substituting a larger M^{3+} ion, the conductivity became lower, compared with that for smaller M^{3+} (Al^{3+} or Cr^{3+}) systems. A poorly conductive second phase might be formed, which would block Li^{+} migration at the grain boundaries.

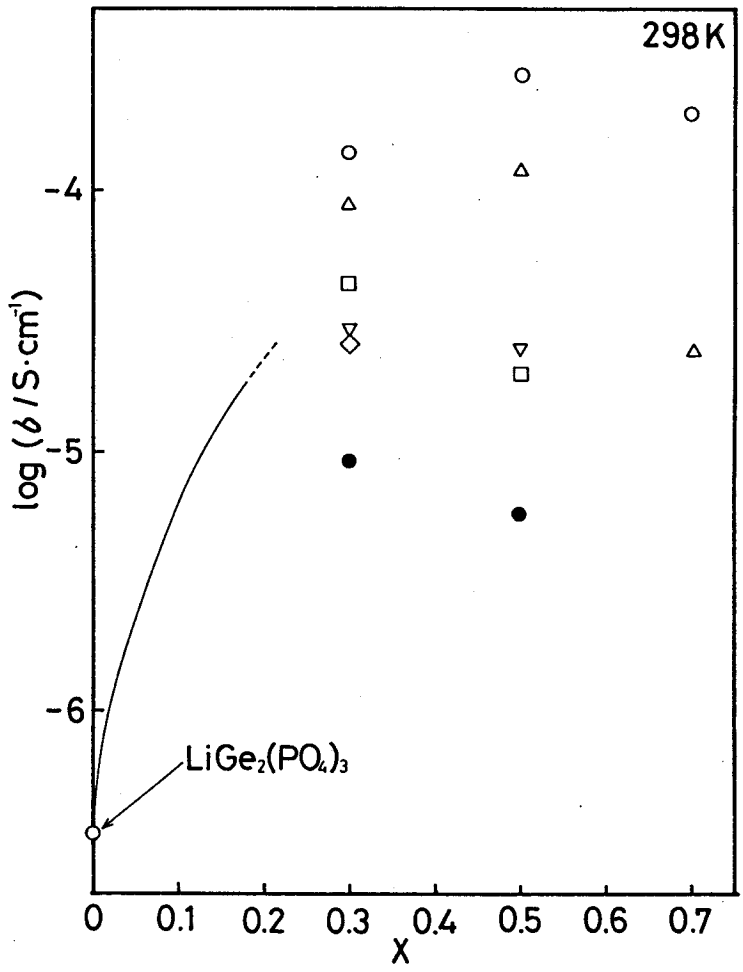

Fig. 4-3. Conductivity at 298 K vs. the x value for the $Li_{1+x}M_xGe_{2-x}(PO_4)_3$ system.
M=Al(○), Cr(△), Ga(□), Fe(▽), Sc(◇),or In(●)

Figure 4-4 shows a representive complex impedance plot of $Li_{1.5}Al_{0.5}Ge_{1.5}(PO_4)_3$. Two semicircles were observed. The bulk and the total resistances were determined from these semicircles, as is shown in the figure. From these results, the conductivity for the bulk and the grain boundary can be determined. Figure 4-5 gives the conductivity for the bulk and the grain boundary as

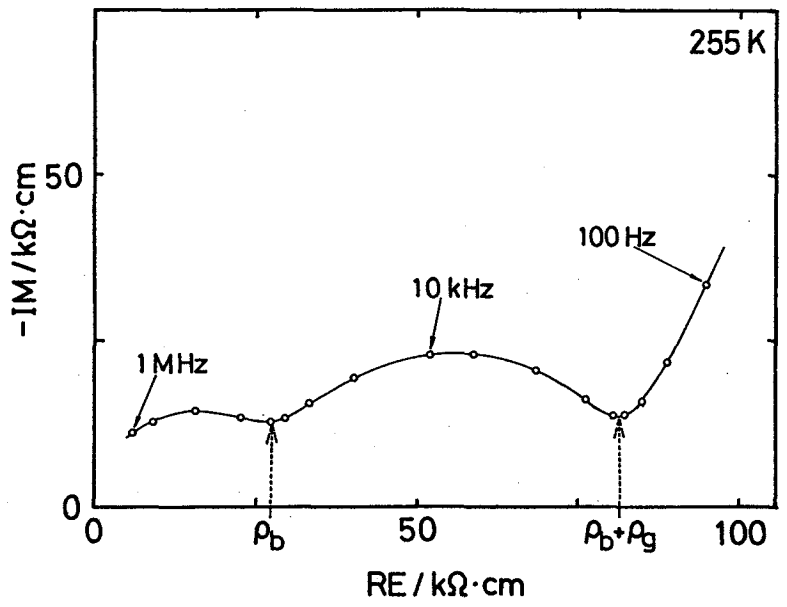

Fig. 4-4. Complex impedance plot for $Li_{1.5}Al_{0.5}Ge_{1.5}(PO_4)_3$ at 255 K.

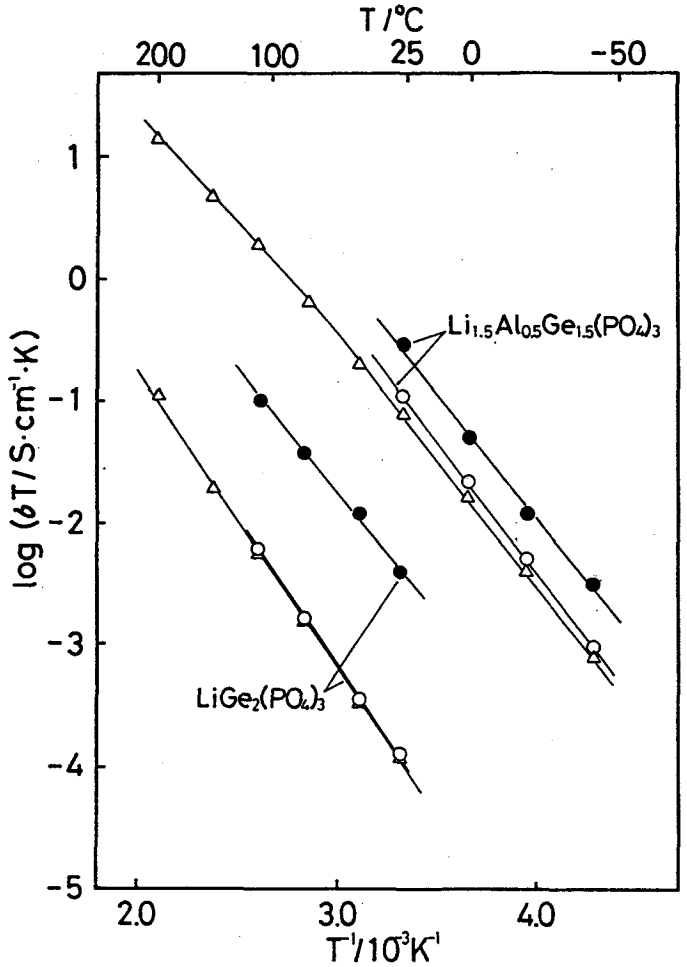

Fig. 4-5. Temperature dependencies of the conductivity for the bulk and the grain boundary for $LiGe_2(PO_4)_3$ and $Li_{1.5}Al_{0.5}Ge_{1.5}(PO_4)_3$.
bulk(●), grain boundary(○), total(△)

well as their total, for typical samples. The conductivity for the bulk is higher than that for the grain boundary. The total conductivity is almost the same as the grain boundary value. This means that the total conductivity is mainly determined by that of the grain boundaries.

The activation energies for Li^+ migration in the bulk and the grain boundary (estimated from Fig. 4-5) are presented in Fig. 4-6. The activation energy for the bulk and the grain boundary can not be determined for a higher x region, or for Sc^{3+} and In^{3+} substituted systems, since the two clear semicircles were not obtained on the complex impedance plane. Regarding the bulk component, the activation energy dose not change upon M^{3+} substitution. The change in the lattice size and lithium insertion in the A(2) site by M^{3+} substitution do not influence Li^+ conduction in the 3D network structure. The activation energy for Li^+ migration in bulk for the $LiGe_2(PO_4)_3$ structure is 0.38 eV, which agree with that in chapter 3. This is higher than that for the $LiTi_2(PO_4)_3$ structure of 0.30 eV. The cell volume for $LiTi_2(PO_4)_3$ is 1309 $Å^3$, which is larger than 1218~1230 $Å^3$ for the Ge-systems. The small lattice size for $LiGe_2(PO_4)_3$ makes the activation energy increase for Li^+ migration in the 3D network structure. The activation energy for the grain boundary decreases with an increase in x.

The dependence of the porosity of the sintered pellet on x is shown in Fig. 4-7. No treatment could produce a dense pellet for $LiGe_2(PO_4)_3$, itself. The porosity decreased with an increase in x for all of the systems examined. This tendency is consistent with the conductivity enhancement shown in Fig. 4-3. The conductivity also increased for the In^{3+} system, though the ion

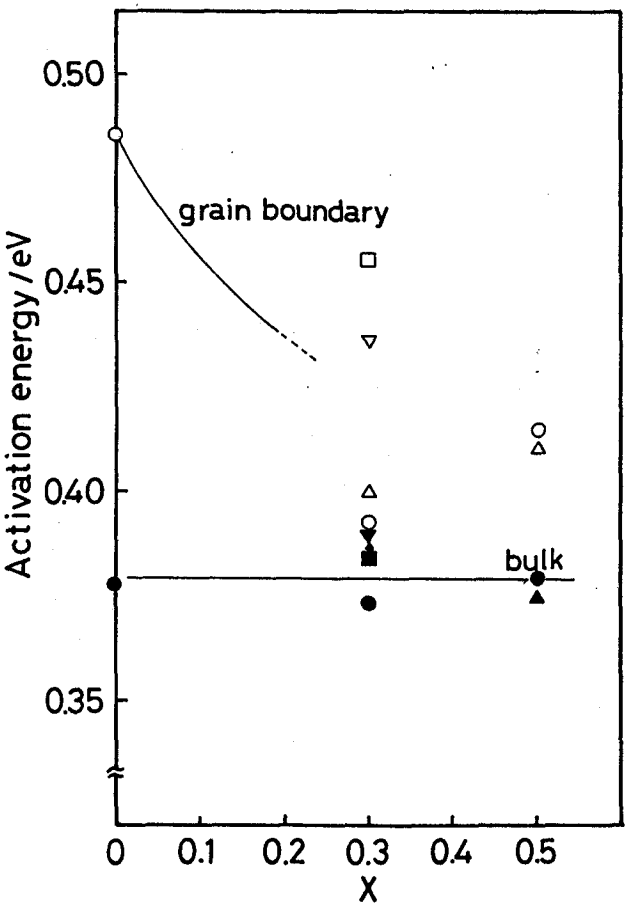

Fig. 4-6. Activation energy for the bulk and the grain boundary in the $Li_{1+x}M_xGe_{2-x}(PO_4)_3$ system.
M=Al: bulk(●), grain boundary(○)
M=Cr: bulk(▲), grain boundary(△)
M=Ga: bulk(■), grain boundary(□)
M=Fe: bulk(▼), grain boundary(▽)

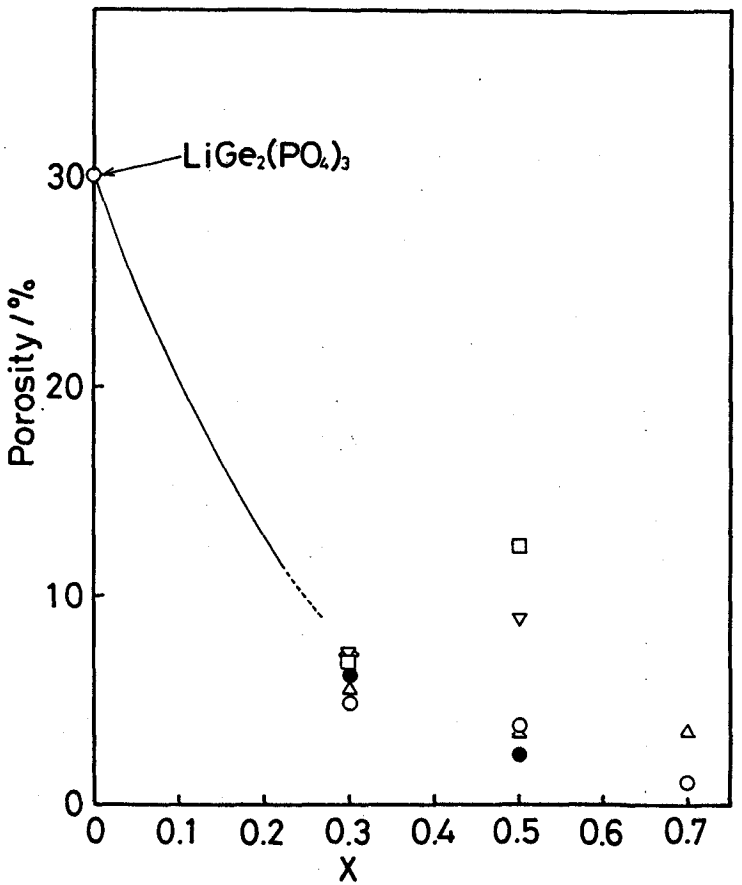

Fig. 4-7. Variation of the porosity for the $Li_{1+x}M_xGe_{2-x}(PO_4)_3$ system.
M=Al(○), Cr(△), Ga(□), Fe(▽), Sc(◇), or In(●)

could not be replaced with the Ge^{4+} site. One of the reasons for the conductivity enhancement is ascribed to an increase in densification. Although the porosity at x=0.3 was almost the same for all of the M^{3+} substitution systems, the total conductivity tends to decrease with an increase in the ionic radius of the M^{3+} ion. For the larger M^{3+} substitution samples, the activation energy for the grain boundary shows a higher value in Fig. 4-6. This indicates that the conductivity depends on the activation energy for the grain boundary. In chapter 2, the reason for the conductivity enhancement with an x increase for the Ti-system of $Li_{1+x}M_xTi_{2-x}(PO_4)_3$, has been attributed to an increase in the sinterability, as well as to a decrease in the activation energy for the grain boundary. For the Ge-system, the same explanation holds for the conductivity enhancement. The Li^+ ion conduction of the grain boundary is assimilated to that of the bulk structure by high sinterability for the x increased samples.

4-3-2. $LiHf_2(PO_4)_3$-based electrolyte

—Phase—

The sintering process should be conducted at high temperature to obtain the rhombohedral structure in the case of the solid electrolyte based on $LiHf_2(PO_4)_3$. Figure 4-8 presents the X-ray diffraction patterns for the sample of $LiHf_2(PO_4)_3$ sintered at 1393 K and 1493 K. The X-ray pattern for the sample sintered at 1493 K is the same as that for the NASICON-type $R\bar{3}c$ structure. However, the sample sintered at 1393 K is identical with the β-$Fe_2(SO_4)_3$-type monoclinic phase ($P2_1/n$).[57-59]

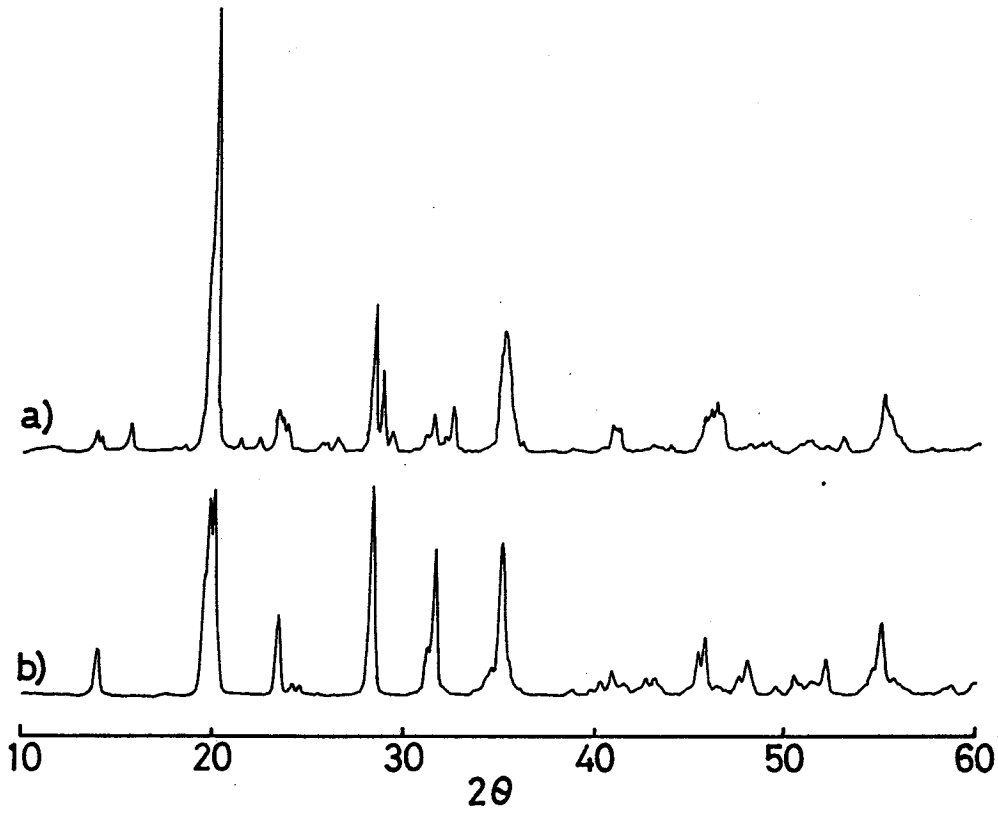

Fig. 4-8. The X-ray diffraction patterns (Cu-Kα) for $LiHf_2(PO_4)_3$ sintered at (a)1393 K and (b)1493 K.

—$LiHf_2(PO_4)_3$+yLi_2O system—

This system was partially shown in chapter 3. The relationship between the sintering temperature and the porosity of the sintered pellet is shown in Fig. 4-9. The high density pellet could not be obtained for $LiHf_2(PO_4)_3$ even if the sintering temperature raised to 1593 K. On the other hand, high density pellet can be obtained for the samples with Li_2O addition. Li_2O acts as a flux to form a high density sample. The effect of the Li_2O addition has been already described in chapter 2 and 3. The porosity greatly decreased by the sintering at around 1173 K, and then increased by the elevation of the sintered temperature for all the Li_2O added samples.

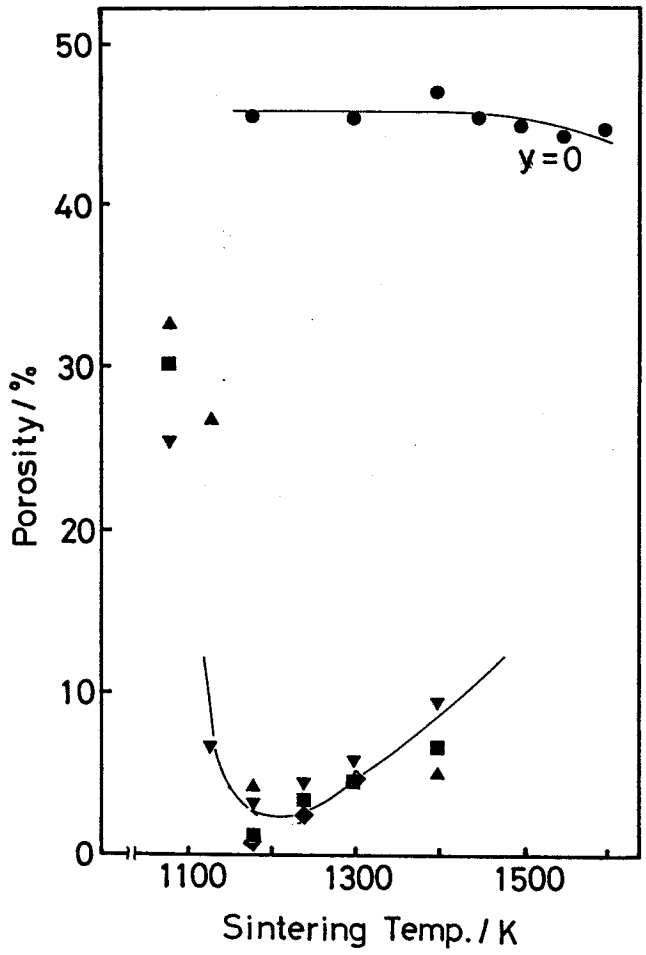

Fig. 4-9. Relationship between the porosity and the sintered temperature for the $LiHf_2(PO_4)_3$+yLi_2O system. y=0(●), 0.1(▲), 0.2(▼), 0.3(■), 0.4(◆)

Figure 4-10 shows the surface microstructure of the sintered $LiHf_2(PO_4)_3$+0.3Li_2O samples. The grains are closely contacted with one another for the sample heated at 1173 K (a). The particle size was smaller than 1 μm, which is almost the same as that of the ball-milled powder. The surface of the sintered sample is very smooth. No other peaks without those of $LiHf_2(PO_4)_3$ can be detected from the X-ray diffraction patterns for all the samples of the $LiHf_2(PO_4)_3$+yLi_2O system. In addition, the lithium atom did not evaporate by the heating process, which was confirmed by an atomic absorption measurement. The added Li_2O

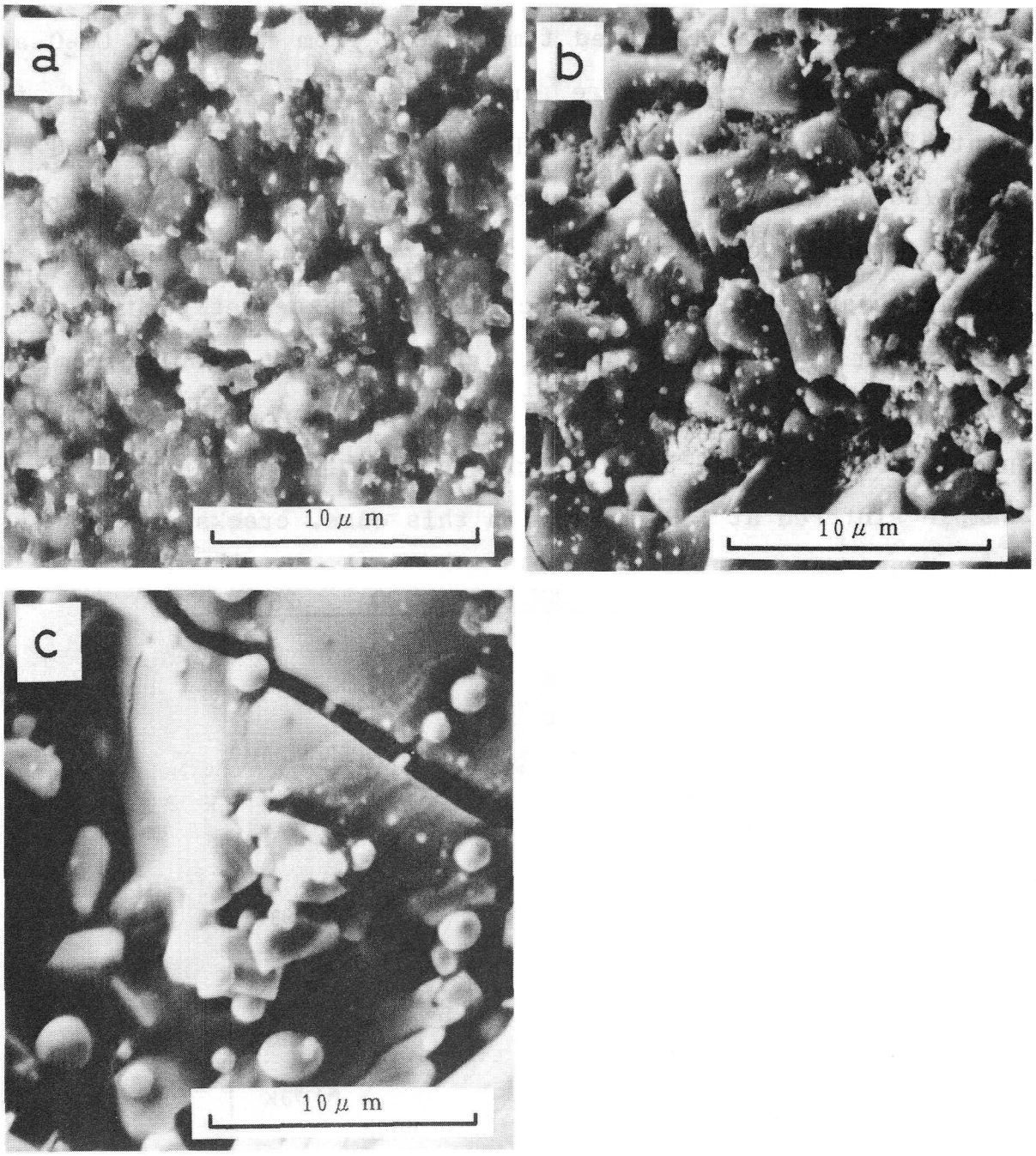

Fig. 4-10. Surface microstructure for $LiHf_2(PO_4)_3$+0.3Li_2O sintered at (a)1173 K, (b)1293 K, and (c)1393 K.

would exist as a glassy phase at grain boundaries. However, Li_2O itself has a high melting point. The glassy lithium phosphate would be formed at elevated temperature from the added Li_2O and phosphate. The grain size grew with the elevation of the sintering temperature (b). The fine granules appeared on $LiHf_2(PO_4)_3$ grains. The granules would be the lithium phosphate or Li_2O which acts as a flux. Some pores observed between the particles appeared (b). The increase in the pellet porosity with the sintering temperature (in Fig. 4-9) might result from the fact that the pore size at the grain boundary increase with the particle growth. The particle growth greatly accelerated for the sample sintered at 1393 K (c). In this case, cracks are observed in the grains.

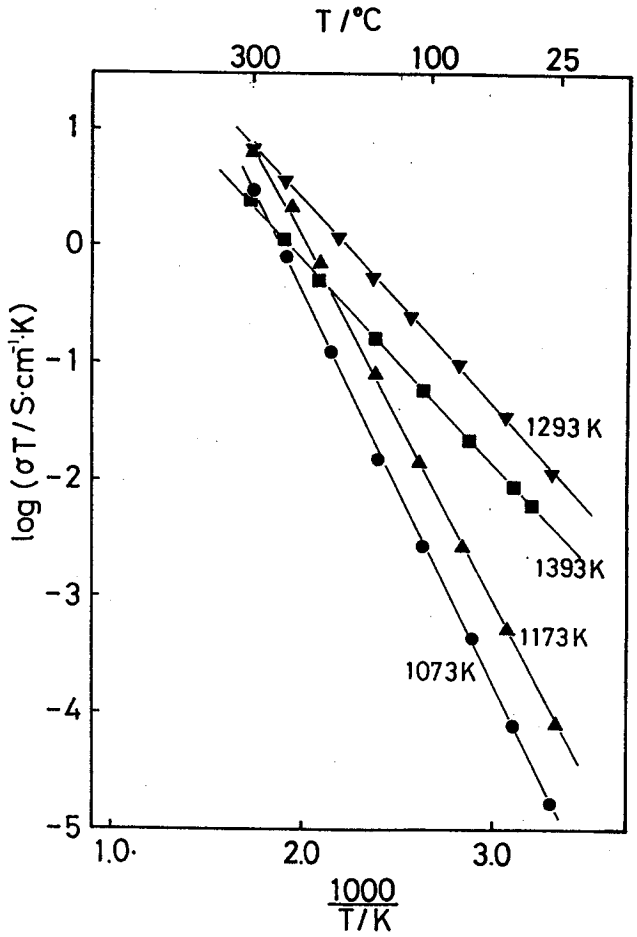

Fig. 4-11. The σT-1/T relation for $LiHf_2(PO_4)_3$+0.3Li_2O samples.

Figure 4-11 presents the temperature dependence of the total (bulk plus grain boundary) conductivity for $LiHf_2(PO_4)_3$+0.3Li_2O sample. The conductivity greatly enhanced for the samples sintered at above 1293 K. The β-$Fe_2(SO_4)_3$-type ($P2_1/n$) monoclinic phase was formed for the samples sintered at lower than 1293 K. The slope of the σT-1/T relation decreased by the formation of the NASICON-type structure. It seems that the Li^+ ion does not easily migrate in the monoclinic phase. Figure 4-12 shows the relationship between the activation energy for the total conductivity and the sintering temperature. The activation energy was determined in the temperature range from room temperature to 400 K. The activation energy abruptly decreased with the sintering temperature for all the samples. The decrease

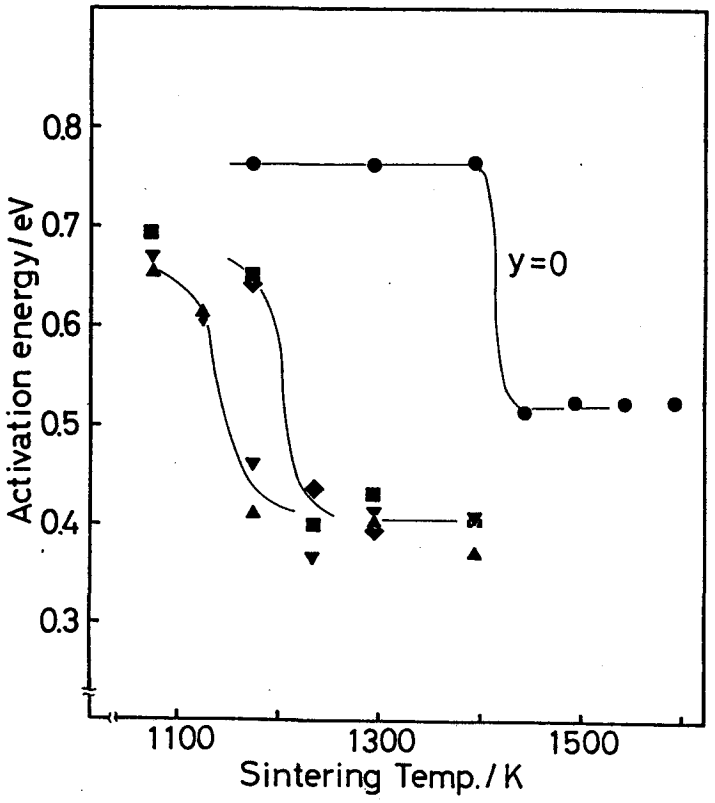

Fig. 4-12. Relationship between the activation energy and the sintered temperature for the $LiHf_2(PO_4)_3$+yLi_2O system. y=0(●), 0.1(▲), 0.2(▼), 0.3(■), 0.4(◆)

in the activation energies is attributed to the $P2_1/n$ -> $R\bar{3}c$ phase transition. Although the samples calcined at 1173 K during the preparing process, $R\bar{3}c$ phase could not be formed for all the calcined powder. The obtained rhombohedral phase did not revert to the monoclinic phase by cooling. The phase transition temperature is about 1423 K for $LiHf_2(PO_4)_3$ y=0, and the temperature decreased with the Li_2O addition. The transition temperature for Li_2O added samples is close to that of the high densification (in Fig. 4-9). The decrease of the transition temperature might be influenced by the high sinterability. Figure 4-13 shows the total conductivity at 298 K for $LiTi_2(PO_4)_3$+yLi_2O system. The conductivity considerably increased with the sintering temperature. It is considered that the conductivity was enhanced by both the formation of the NASICON-type phase and the decrease in the porosity. Although the porosity decreased for the monoclinic samples of y=0.3 and 0.4 sintered at 1173 K, the conductivity enhancement with high densification is smaller than that with the formation of NASICON-type phase. The conductivity enhancement mainly occurred by the formation of the NASICON-type phase. The conductivity also greatly enhanced by the Li_2O addition. For Li_2O added samples, a maximum conductivity was obtained for the samples sintered at ca. 1293 K. The conductivity decreased for the samples sintered above 1293 K. The particle growth might affect the decrease of the conductivity (see Fig. 4-10). The maximum conductivity is 1.1×10^{-4} $S \cdot cm^{-1}$ for $LiHf_2(PO_4)_3$+0.1Li_2O sintered at 1293 K.

Table 4-1 shows the activation energy for Li^+ conduction of the bulk and the grain boundary for the $LiHf_2(PO_4)_3$+yLi_2O (rhombohedral) system. The activation energy for y=0.1, 0.2 was

determined in the temperature range between 223 K and room temperature. The activation energy at the grain boundary decreased by the Li_2O addition. The enhancement of the

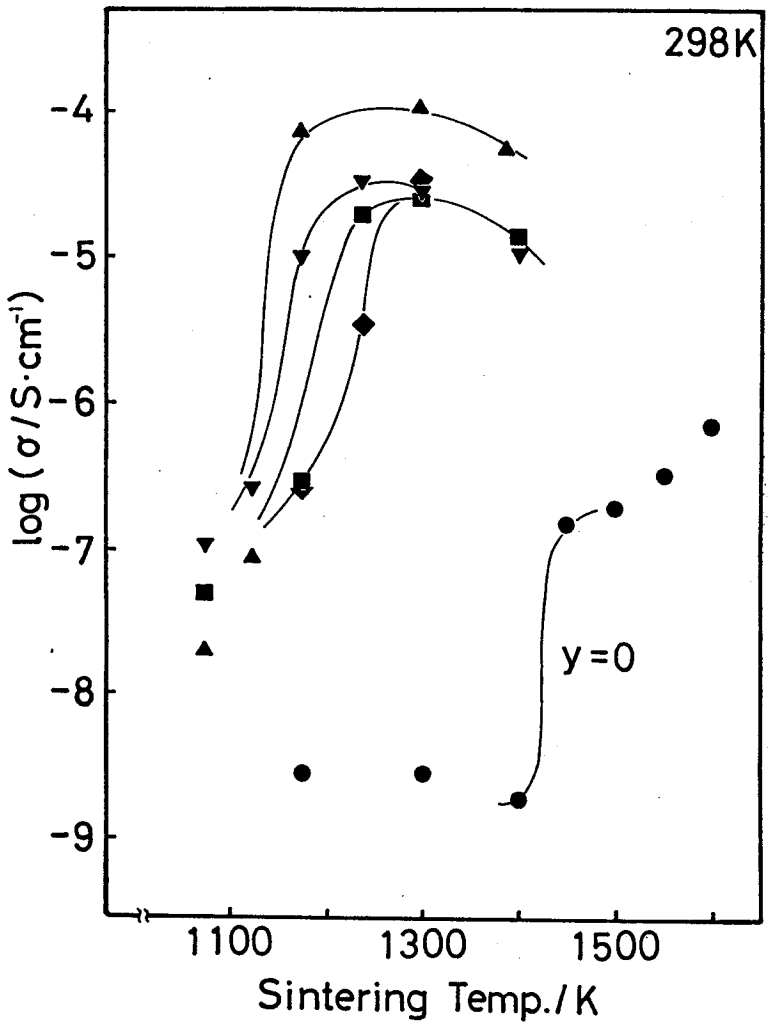

Fig. 4-13. Relationship between the total conductivity at 298 K and the sintered temperature for the $LiHf_2(PO_4)_3$+yLi_2O system. y=0(●), 0.1(▲), 0.2(▼), 0.3(■), 0.4(◆)

Table 4-1. The activation energy of the bulk and the grain boundary for $LiHf_2(PO_4)_3$+yLi_2O system.

Sample	Bulk (eV)	Grain boundary(eV)
$LiHf_2(PO_4)_3$	0.43	0.56
$LiHf_2(PO_4)_3$+0.1Li_2O	0.42	0.47
$LiHf_2(PO_4)_3$+0.2Li_2O	0.42	0.48

conductivity by the Li_2O addition is attributed to the decrease in the activation energy at the grain boundary and the high densification. On the other hand, the activation energy for bulk component remains constant (ca. 0.42 eV) for $LiHf_2(PO_4)_3$ network structure. This value is higher than 0.30 eV of $LiTi_2(PO_4)_3$ system (Cell volume: 1309 $Å^3$), because the lattice size for Li^+ migration in $LiHf_2(PO_4)_3$ (Cell volume: 1486 $Å^3$) is larger than that in $LiTi_2(PO_4)_3$. The tunnel size for the 3D structure of $LiHf_2(PO_4)_3$ is too large for Li^+ migration.

—$Li_{1+x}M_xHf_{2-x}(PO_4)_3$ (M=Cr,Fe,Sc,In,Lu, or Y) system—

In these systems, the samples were sintered at above 1293 K, and the sintering temperature was chosen in such a way that a maximum conductivity was obtained. The NASICON-type structure was formed for all the samples examined. A small amount of $P2_1/n$ monoclinic phase remained as a secondary phase for some samples. Figure 4-14 presents the variation of lattice constants as a function of x for $Li_{1+x}M_xHf_{2-x}(PO_4)_3$ (M=Cr, Fe, Sc, In, Lu, or Y) systems. The rhombohedral phase distorted into monoclinic (space group C2/c) phase by the M^{3+} substitution for all the samples with x=0.5. The lattice constant of a-axis increased with the replacement of Hf^{4+} ion for larger M^{3+} ions (Sc^{3+}, In^{3+}, Lu^{3+}, or Y^{3+}) and that decreased by smaller cations (Cr^{3+} or Fe^{3+}). However, c-parameter decreased for all the $Li_{1+x}M_xHf_{2-x}(PO_4)_3$ systems examined. It is not clear why c parameter decreased by the M^{3+} ion substitution. The decrease of c-axis has also been reported for Zr^{4+}-systems of NASICON[11,12] and $Na_{1+x}M_xZr_{2-x}(PO_4)_3$ (M=Cr,In,Yb).[60] On the other hand, for Ti^{4+}-system of $Li_{1+x}M_xTi_{2-x}(PO_4)_3$ (M=Al,Cr,Sc,etc.) in chapter 2, the lattice constant of c

axis was clearly increased by larger M^{3+} ion substitution. The HfO_6 and ZrO_6 octahedra in rhombohedral skeleton would be easy to distort because of a larger ionic radius for Hf^{4+} and Zr^{4+} ions. The oxygen coordination of HfO_6 may be shifted by the M^{3+} substitution or Li^+ insertion into A_2 sites.

The relationship between the porosity of the sintered pellet and x for the $Li_{1+x}M_xHf_{2-x}(PO_4)_3$ system is shown in Fig. 4-15. The high density pellets could be obtained by the x increase except for M=Cr system. The sintering temperature above 1393 K is necessary to obtain the high density samples for all the systems examined. Figure 4-16 presents the relationship between the total

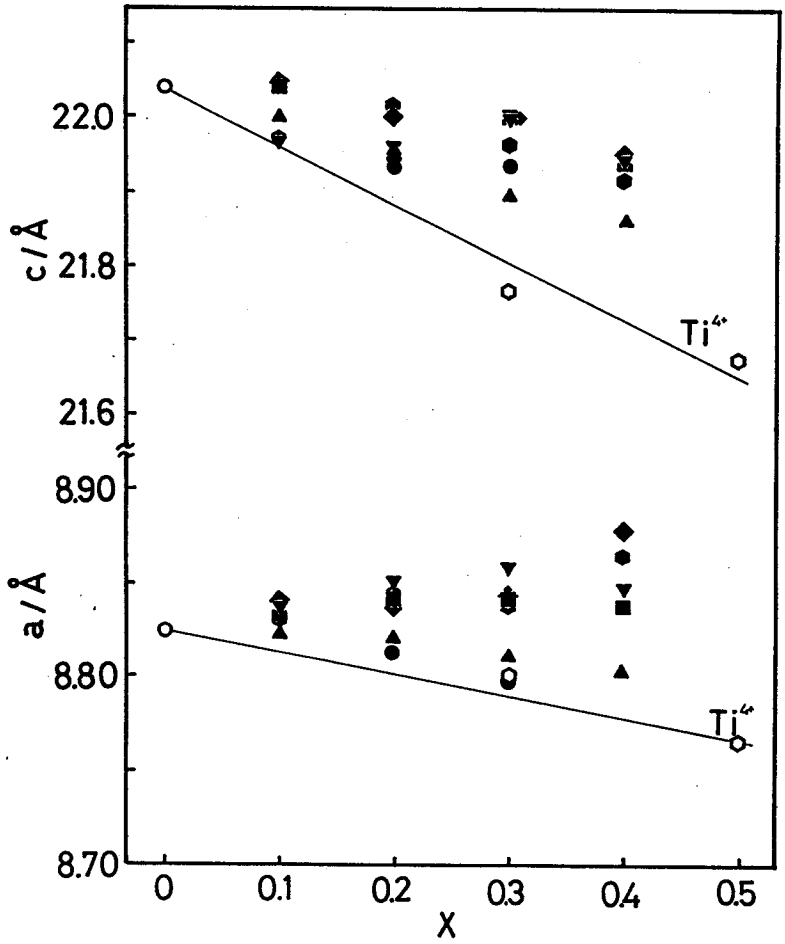

Fig. 4-14. Variation of the lattice constants on x for the $Li_{1+x}M_xHf_{2-x}(PO_4)_3$ system.
M=Cr(●), Fe(▲), Sc(▼), In(■), Lu(◆),or Y(⬢)

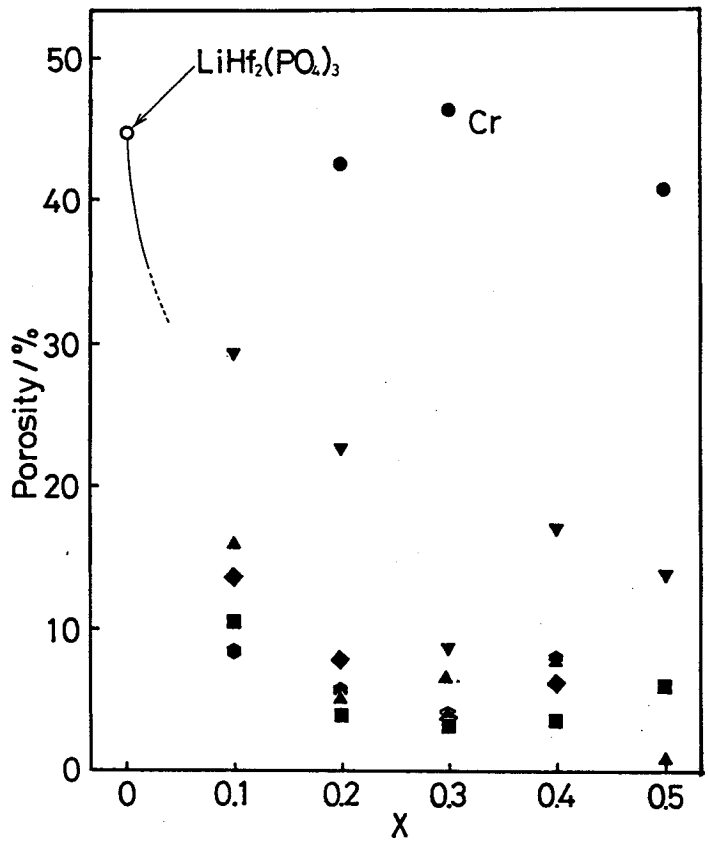

Fig. 4-15. Relationship between the porosity for the sintered pellet and x value for the $Li_{1+x}M_xHf_{2-x}(PO_4)_3$ system. M=Cr(●), Fe(▲), Sc(▼), In(■), Lu(◆),or Y(⬢)

conductivity at 298 K and x value for the $Li_{1+x}M_xHf_{2-x}(PO_4)_3$ system. The conductivity increased greatly with x except for M=Cr system. A maximum conductivity was obtained for x=0.2 or 0.3, and the value was $1.7x10^{-4}$ $S \cdot cm^{-4}$ for the sample of $Li_{1.2}Fe_{0.2}Hf_{1.8}(PO_4)_3$. For M=Cr system, the conductivity and the sinterability did not increase with x. A very small amount of $Li_3Cr_2(PO_4)_3$ was formed as a secondary phase, which was confirmed by the X-ray measurement. However, $Li_3Cr_2(PO_4)_3$ is a very stable phosphate and has a high melting point.[61] The second phase might not act as a flux for a high density sample. Table 4-2 shows the activation energy of the bulk component for the $Li_{1+x}M_xHf_{2-x}(PO_4)_3$ system. The activation energy could not be determined for

the other samples, since the two minimum points on the cole-cole plot could not be clearly obtained. The activation energy for bulk component is also ca. 0.42 eV, which agreed with that of $LiHf_2(PO_4)_3$+yLi_2O system. The partial M^{3+} ion substitution and the Li^+ occupation at A_2 site did not influence the activation energy for Li^+ migration in the NASICON-type structure. For $LiHf_2(PO_4)_3$-based electrolytes, the conductivity enhancement is also ascribed to the decrease of the conductivity with the high densification.

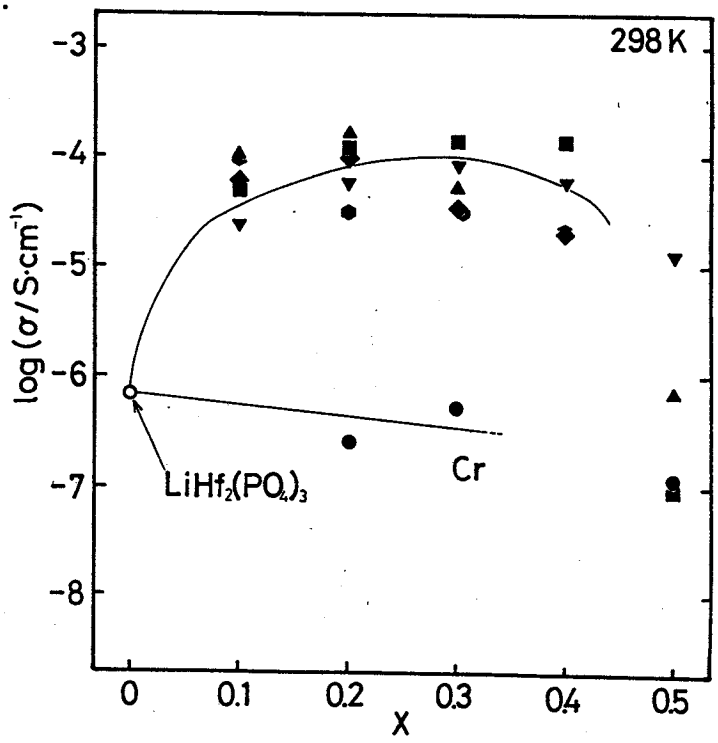

Fig. 4-16. Conductivity at 298 K vs. the x value for the $Li_{1+x}M_xHf_{2-x}(PO_4)_3$ system.
M=Cr(●), Fe(▲), Sc(▼), In(■), Lu(◆),or Y(⬢)

Table 4-2. The activation energy of the bulk component for the $Li_{1+x}M_xHf_{2-x}(PO_4)_3$ system.

Sample	Bulk(eV)
$Li_{1.3}Fe_{0.3}Hf_{1.7}(PO_4)_3$	0.42
$Li_{1.3}Sc_{0.3}Hf_{1.7}(PO_4)_3$	0.42
$Li_{1.2}In_{0.2}Hf_{1.8}(PO_4)_3$	0.41
$Li_{1.3}In_{0.3}Hf_{1.7}(PO_4)_3$	0.43

4-4. Summary

The electrical properties and the crystal structure were studied for the ceramic electrolytes based on $LiGe_2(PO_4)_3$ and $LiHf_2(PO_4)_3$. The cell volume obtained experimentally is lower than the calculated one for $Li_{1+x}M_xGe_{2-x}(PO_4)_3$, M=$Ga^{3+}$, Fe^{3+}, Sc^{3+}, and In^{3+} because these larger M^{3+} ions can not easily substitute the Ge^{4+} ions. The Al^{3+} or Cr^{3+} ion could substitute the Ge^{4+} site more easily, owing to the closer ionic radius. In the case of $LiHf_2(PO_4)_3$-based electrolytes, The phase transition from $P2_1/n$ phase to NASICON-type $R\bar{3}c$ structure was observed at above 1173 K. The M^{3+} ion easily substitute the Hf^{4+} ions for all the $Li_{1+x}M_xHf_{2-x}(PO_4)_3$, M=$Cr^{3+}$, Fe^{3+}, Sc^{3+}, In^{3+}, Lu^{3+}, and Y^{3+} systems.

The conductivity is enhanced with an increase in x for all of the $Li_{1+x}M_xGe_{2-x}(PO_4)_3$ systems and the $Li_{1+x}M_xHf_{2-x}(PO_4)_3$ systems. The M^{3+} substitution did not affect the activation energy of bulk component for both the systems. The conductivity was greatly enhanced by the addition of the lithium compound and partial substitution of M^{4+} site by M^{3+} ion because of the high densification and the decrease in the activation energy at the grain boundary. The maximum conductivity of 2.4×10^{-4} $S\cdot cm^{-1}$ and 1.7×10^{-4} $S\cdot cm^{-1}$ at 298 K was obtained for $LiGe_2(PO_4)_3$-based and $LiHf_2(PO_4)_3$-based electrolytes, respectively. These conductivity obtained is smaller than 7.0×10^{-4} $S\cdot cm^{-1}$ of $LiTi_2(PO_4)_3$-based electrolytes in chapter 2. However, these electrolytes are superior for the application such as battery and gas sensors, since the tetra-valent Hf^{4+} cation is more stable toward a lithium metal and reductive gases than Ti^{4+} ion.

Chapter 5

Electrical Properties and Crystal Structure for $Li_3Cr_2(PO_4)_3$-based Solid Electrolyte

5-1. Introduction

In chapter 2~4, NASICON-type Li^+ ion conductive electrolytes have been reported to show a high conductivity even at room temperature. The solid electrolytes based on $LiTi_2(PO_4)_3$ (Cell volume ca. 1309 $Å^3$) show a maximum conductivity and a minimum activation energy for Li^+ migration. $LiTi_2(PO_4)_3$-based solid electrolytes have the most suitable lattice size for Li^+ migration. F.d'Yvoire et al. reported that the NASICON-type structure was obtained by quenching $Li_3Cr_2(PO_4)_3$ from 1703 K to room temperature.[61] The cell volume of the NASICON-type $Li_3Cr_2(PO_4)_3$ reported is 1316 $Å^3$, which is very close to that of $LiTi_2(PO_4)_3$. This indicates that $Li_3Cr_2(PO_4)_3$-based compound has the possibility for the high conductivity. Furthermore, the conductivity enhancement can be also expected by the increase in mobile lithium ions, if the Cr^{3+} site is substituted for a divalent Mg^{2+} ion in $Li_3Cr_2(PO_4)_3$.

In this chapter, the electrical properties and the crystal structure were examined for the polycrystalline $Li_{3+x}Mg_xCr_{2-x}(PO_4)_3$ system.

5-2. Experimantal

Li_2CO_3 (purity:99.99%), MgO (99.9%) Cr_2O_3 (99.9%), and

$(NH_4)_2HPO_4$ (extra pure grade) were used as starting materials. The detail of the sample preparation and the measurements have been described in chapter 3.

5-3. Results and Discussion

—Phase—

For $Li_3Cr_2(PO_4)_3$, β-$Fe_2(SO_4)_3$ type ($P2_1/n$) phase was formed when the sintering was conducted at the temperature lower than 1473 K. Monoclinic phase (C/2c) was obtained for the samples sintered above 1473 K. However, cracks appeared in the $Li_3Cr_2(PO_4)_3$ pellets by the phase transition from $P2_1/n$ to C/2c. In the case of the $Li_{3+x}Mg_xCr_{2-x}(PO_4)_3$ system (x>0), β-$Fe_2(SO_4)_3$ type $P2_1/n$ phase was formed when the sintering is conducted above 1473 K. We tried to obtain the NASICON-type rhombohedral ($R\bar{3}c$) phase by quenching the molten samples by pressing them between two iron plates. However only the $P2_1/n$ monoclinic phase was

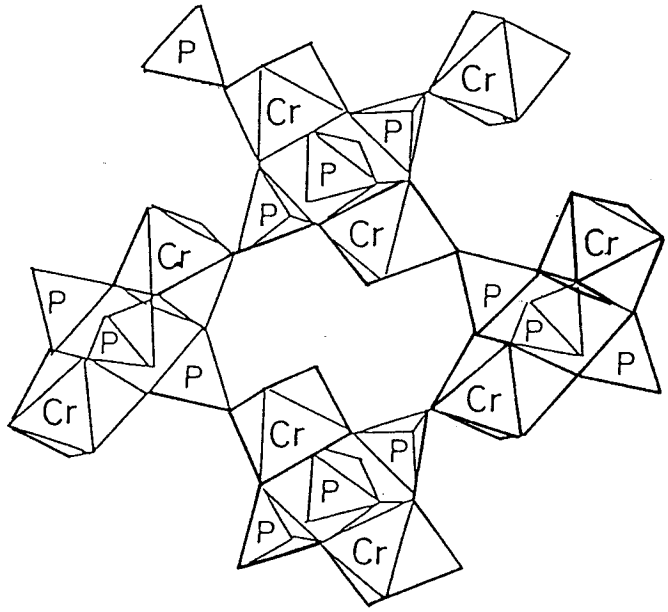

Fig. 5-1. β-$Fe_2(PO_4)_3$-type structure for $Li_3Cr_2(PO_4)_3$.

formed by the quenching for the samples of x>0. We could not succeed in obtaining the NASICON-type $Li_3Cr_2(PO_4)_3$-based electrolyte. The electrical properties were determined for the sintered samples of the β-$Fe_2(SO_4)_3$ type mono-clinic ($P2_1/n$) phase (Fig. 5-1).

We presumed that the lattice constants increase with x value, because the ionic radius of Mg^{2+} (0.720 Å) ion is larger than that of Cr^{3+} (0.615 Å) ion.[12] However, the lattice constants did not increase. The $Li_5Mg_2(PO_4)_3$ phase was observed as a second phase when Mg^{2+} is mixed with $Li_3Cr_2(PO_4)_3$. In the present $Li_{3+x}Mg_xCr_{2-x}(PO_4)_3$ system, the Mg^{2+} ions could not substitute the Cr^{3+} sites at all, and resulted in the mixed phase of $Li_3Cr_2(PO_4)_3$ and $Li_5Mg_2(PO_4)_3$. The $Li_{3+x}Mg_xCr_{2-x}(PO_4)_3$ system should be described as $(1-y)Li_3Cr_2(PO_4)_3$-$yLi_5Mg_2(PO_4)_3$ system ($y=x/2$).

—Electrical properties and sinterability—

The total conductivity (bulk plus grain boundary) at 298 K and the porosity of the sintered pellet for the $(1-y)Li_3Cr_2(PO_4)_3$-$yLi_5Mg_2(PO_4)_3$ system are plotted in Fig. 5-2. The conductivity was greatly enhanced with the y increase, and a maximum conductivity of 4.6×10^{-5} $S\cdot cm^{-1}$ was obtained for y=0.2. Although the high density pellet could not be obtained for $Li_3Cr_2(PO_4)_3$ (y=0), the porosity decreased by increasing y. The second phase of $Li_5Mg_2(PO_4)_3$ would contribute to obtain high density pellets. $Li_5Mg_2(PO_4)_3$ (y=1.0) itself shows a low conductivity, which was made clear in this study. The conductivity decreased for the system above y=0.2. The lithium migration was blocked by the excessive formation of the low

conductive $Li_5Mg_2(PO_4)_3$ phase.

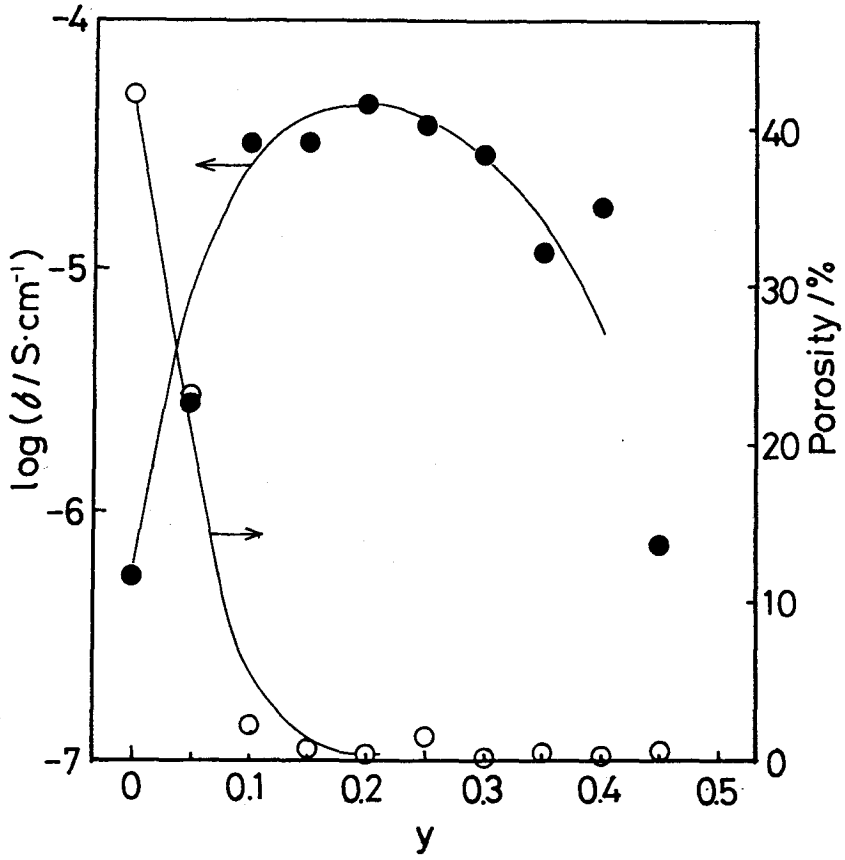

Fig. 5-2. The conductivity at 298 K and the porosity of the sintered pellet of the $(1-y)Li_3Cr_2(PO_4)_3$-$yLi_5Mg_2(PO_4)_3$ system. conductivity(●), porosity(○)

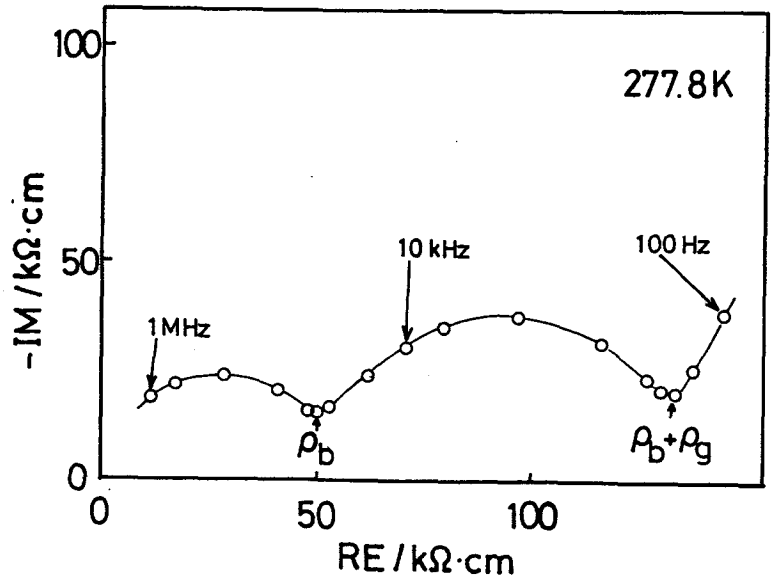

Fig. 5-3. Cole-cole plot for the sample of $0.8Li_3Cr_2(PO_4)_3$-$0.2Li_5Mg_2(PO_4)_3$ at 277.8 K.

Figure 5-3 presents the cole-cole plot for the $0.8Li_3Cr_2(PO_4)_3$-$0.2Li_5Mg_2(PO_4)_3$ sample at 277.8 K. Two semicircles are ascribed to the resistance for the bulk and the grain boundary components. By the cole-cole plot method, the conductivities for the bulk and the grain boundary were separately estimated. The activation energies of the conductivity of the bulk and the grain boundary components are shown in Fig. 5-4. The activation energy for the bulk component is constant. The activation energy for Li^+ migration in $Li_3Cr_2(PO_4)_3$

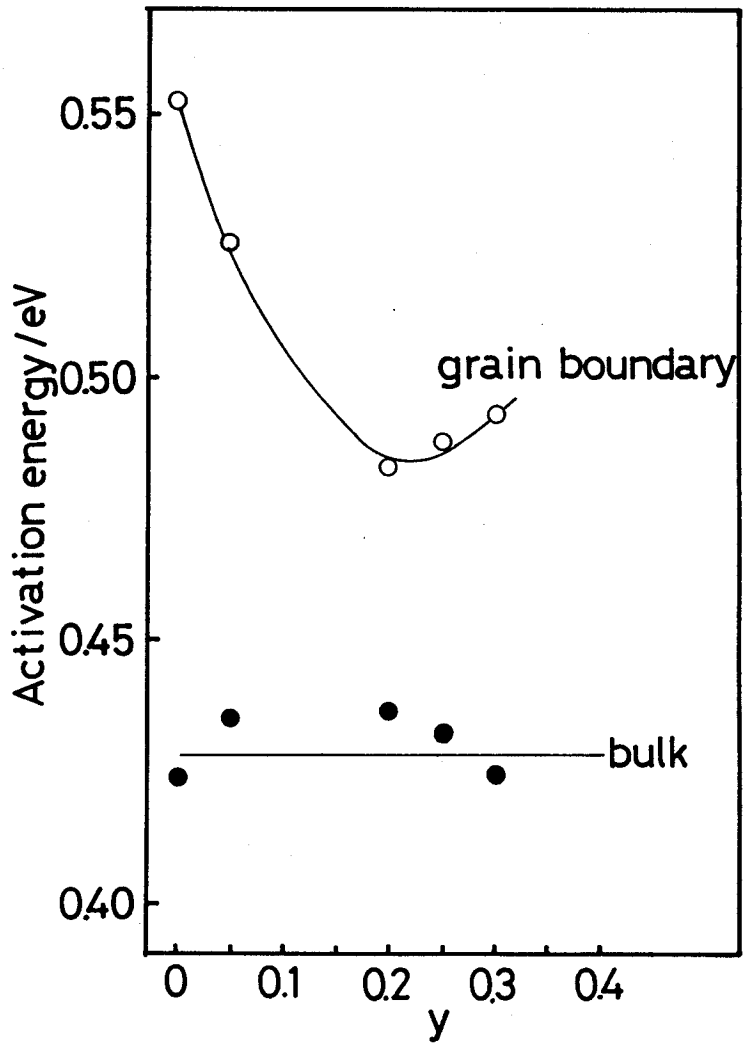

Fig. 5-4. The activation energy for the bulk and the grain boundary for the $(1-y)Li_3Cr_2(PO_4)_3$-$yLi_5Mg_2(PO_4)_3$ system. bulk(●), grain boundary(○)

bulk was determined to be 0.43 eV. The addition of $Li_5Mg_2(PO_4)_3$ phase in $Li_3Cr_2(PO_4)_3$ did not influence the activation energy for the bulk component. The activation energy for the grain boundary decreased by the increase in y value. This indicates that the total conductivity enhancement (in Fig. 5-2) resulted from the decrease in the activation energy of the Li^+ ion conduction at the grain boundary with the high densification.

5-4. Summary

$Li_3Cr_2(PO_4)_3$-based ceramics were investigated to obtain a high Li^+ ionic conductor at room temperature. The $0.8Li_3Cr_2(PO_4)_3$-$0.2Li_5Mg_2(PO_4)_3$ sample shows a maximum conductivity of 4.6×10^{-5} $S\cdot cm^{-1}$ at 298 K. This conductivity was about one order of magnitude lower than that of the NASICON-type Li^+ ion conductors reported in this thesis. However, the obtained conductivity is considerable high in the oxide-based electrolytes. The β-$Fe_2(PO_4)_3$ type electrolyte would be another candidate for the promising high Li^+ conducting material.

Chapter 6

Concluding Remarks

In the work of this thesis, NASICON-type Li^+ ionic conductors are investigated to obtain the high conductivity at room temperature. The main results and conclusions obtained in this study are summarized as follows.

1. $LiTi_2(PO_4)_3$ has the most suitable tunnel size for the Li^+ migration in the NASICON-type tunnel structure, and whose activation energy is ca. 0.30 eV. The activation energy was increased to 0.38 eV for the small lattice size of $LiGe_2(PO_4)_3$. In the case of large lattice size of $LiHf_2(PO_4)_3$, the activation energy was also increased to 0.42 eV. The electrical properties for the bulk for NASICON-type $LiM_2(PO_4)_3$ ($M=Ge^{4+}$, Ti^{4+}, or Hf^{4+}) hardly changed by the partial M^{4+} substitution for M^{3+} cation and by the partial Li^+ ions insertion in second A(2) lithium sites.

2. The conductivity for the NASICON-type ceramic electrolyte was mainly controlled by that of the grain boundary component at around room temperature. The total conductivity greatly increased with the preparation of the high conductivity grain boundary. The sinterability was increased and the activation energy for the grain boundary was decreased by the M^{4+} substitution for M^{3+} ion or by the addition of the lithium compound for $LiM_2(PO_4)_3$. The reason for the conductivity enhancement with the M^{3+} substitution is attributed to the high sinterability and the decrease of the activation energy at the grain boundary.

3. The excellent conductivity of $7x10^{-4}\sim1x10^{-3}$ $S\cdot cm^{-1}$ at room temperature was obtained for the $LiTi_2(PO_4)_3$-based solid

electrolytes. This conductivity is almost the same as that of Li_3N single crystal, and is higher by one order of magnitude than the reported maximum value as the oxide solid electrolytes. The carrier ion for the $LiTi_2(PO_4)_3$-based electrolyte is Li^+ ion, which was confirmed by the DC conductivity measurement with the Li metal electrodes. However, the Ti^{4+} in $LiTi_2(PO_4)_3$ easily reduced to Ti^{3+} with the contact of Li metal. This shows that the $LiTi_2(PO_4)_3$-based material can not apply as an electrolyte of the lithium battery.

4. $LiGe_2(PO_4)_3$-based and $LiHf_2(PO_4)_3$-based electrolytes, whose materials do not contain the reducible Ti^{4+}, were investigated. The conductivity was greatly enhanced with the M^{4+} (M=Ge and Hf) substitution for the M^{3+} ion or the addition of the lithium compound. The high conductivity of $1x10^{-4}$~$3x10^{-4}$ $S \cdot cm^{-1}$ at room temperature was obtained for both the systems. These materials are promising electrolytes for the high energy density lithium batteries.

5. The $Li_3Cr_2(PO_4)_3$-based electrolytes were investigated to obtain the NASICON-type structure. However, the NASICON-type structure could not obtain in this study, and only β-$Fe_2(SO_4)_3$ type structure was obtained. The activation energy for a Li^+ ion migration is 0.43 eV for this β-$Fe_2(SO_4)_3$ type structure, and the maximum conductivity is $4.6x10^{-5}$ $S \cdot cm^{-1}$ at room temperature. This conductivity is about one order of magnitude lower than that of the NASICON-type Li^+ ion conductors reported in this study. However, the obtained conductivity is considerable high in the oxide-based electrolytes. The β-$Fe_2(SO_4)_3$ type electrolyte would be another candidate for the promising high Li^+ conducting material.

References

(1) W.Nernst, Z.Electrochem, **6**, 41 (1899).

(2) C.Wagner, Naturwissenschaften, **31**, 265 (1943).

(3) C.Tubandt, Z.anorg,allgem.chem., **115**, 105 (1921).

(4) C.Tubandt and H.Reinhold, Z.Electrochem., **29**, 313 (1923).

(5) L.W.Strock, Z.Phys.Chem., **B31**, 132 (1935).

(6) B.Reuter and K.Hardel, Natuwiss., **48**, 161 (1961).

(7) B.B.Owens and A.G.Argue, Science, **157**, 308 (1967).

(8) T.Takahashi, S.Ikeda and O.Yamamoto, J.Electrochem.Soc., **119**, 477 (1972).

(9) N.Weber and J.T.Kummer, Proc.Ann.Pawer Sources Conf., **21**, 37 (1967).

(10) M.S.Whittingham and R.A.Huggins, J.Chem.Phys., **54**, 414 (1971).

(11) J.B.Goodenough, H.Y-P.Hong, and J.A.Kafalas, Mater. Res. Bull., **11**, 203 (1976).

(12) H.Y-P.Hong, Mater. Res. Bull., **11**, 173 (1976).

(13) M.Itoh, E,Sugimoto, and Z.Kouzuka, Trans. Jpn. Inst. Met., **25**, 504 (1984).

(14) T.Maruyama, Y.Saito, Y.Matsumoto, and Y.Yano, Solid State Ionics, **17**, 281 (1985).

(15) N.Imanaka, Y.Yamaguchi, G.Adachi, and J.Shiokawa, J. Electrochem. Soc., **134**, 725 (1987).

(16) S.Yao, Y.Shimizu, N.Miura, and N.Yamazoe, Chem. Lett., 587 (1992).

(17) T.Maruyama, S.Sasaki, and Y.Saito, Solid State Ionics, **23**, 107 (1987).

(18) N.Imanaka, T.Kawasato, and G.Adachi, Chem. Lett., 497 (1990).

(19) N.Imanaka, T.Kawasato, and G.Adachi, Chem. Lett. 13, (1991).

(20) N.Miura, S.Yao, Y.Shimizu, and N.Yamazoe, J. Electrochem. Soc., **139**, 1384 (1992).

(21) A.Pelloux, J.P.Quessada, J.Fouletier, P.Fabry, and M.Kleitz, Solid State Ionics, **1**, 343 (1980).

(22) A.Pelloux, P.Fabry, and P.Durante, Sensors and Actuators, **7**, 245 (1985).

(23) H.Aono, E.Sugimoto, Y.Mori, and Y.Okajima, Chem. Lett.,

1039, (1993).
(24) U.v.Alpen, A.Rabenau, and G.H.Talat, Appl. Phys. Lett., **30**, 621 (1977).
(25) B.A.Boukamp and R.A.Huggins, Mater. Res. Bull., **13**, 23 (1978).
(26) R.Mercier, J.P.Malugani, B.Fahys and A.Saida, Solid State Ionics, **5**, 663 (1981).
(27) H.Wada, M.Menetrier, A.Levasseur, and P.Hagenmuller, Mater. Res. Bull., **18**, 189 (1983).
(28) J.H.Kennedy, S.Sahami, S.W.Shea, and Z.Zhang, Solid State Ionics, **18/19**, 368 (1985).
(29) S.Kondo, K.Takada, and Y.Yamamoto, Solid State Ionics, **53-56**, 1183 (1992).
(30) R.Kanno, Y.Takeda, K.Takada, and O.Yamamoto, J. Electrochem. Soc., **131**, 469 (1984).
(31) R.Kanno, Y.Takeda, O.Yamamoto, C.Cros, W.Gang, and P.Hagenmuller, Solid State Ionics, **20**, 99 (1986).
(32) R.Kanno, Y.Takeda, A.Takahashi, and O.Yamamoto, J. Solid State Chem., **72**, 363 (1988).
(33) A.R.Rodger, J.Kuwano, and A.R.West, Solid State Ionics, **15**, 185 (1985).
(34) H.Y.-P. Hong, Mater. Res. Bull., **13**, 117 (1978).
(35) M. A. Subramanian, R. Subramanian, and A. Crearfield, Solid State Ionics, **18/19**, 562 (1986).
(36) L.Zu-xiang, Y.Hui-jun, L.Shi-chun, and T.Shun-Bao, Solid State Ionics, **18/19**, 549 (1986).
(37) L.Zu-xiang, Y.Hui-jun, L.Shi-chun, and T.Shun-Bao, Solid State Ionics, **31**, 91 (1988).
(38) L.Shi-chun and L.Zu-Xiang, Solid State Ionics, **9/10**, 835 (1983).
(39) S.Hamdoune and D.Tranqui, Solid State Ionics, **18/19**, 587 (1986).
(40) D.Tran qui, S.Hamdoune, J.L.Soubeyroux, and E.Prince, J. Solid State Chem., **72**, 309 (1988).
(41) B.E.Taylor, A.D.English, and T.Berzins, Mater. Res. Bull., **12**, 171 (1977).
(42) L.Hagman and P.Kierkegaard, Acta Chem. Scand., **22**, 1822 (1968).

(43) R.D.Shannon, Acta Cryst., **A32**, 751 (1976).
(44) K.S.Cole and R.H.Cole, J. Chem. Phys., **9**, 341 (1949).
(45) P.G.Bruce and A.R.West, J.Electrochem.Soc., **130**, 662 (1983).
(46) A.M.Glass, K.Nassau, and T.J.Negran, J. App. Phys., **49**, 4808 (1978).
(47) T.Minami, H.Nambu, and M.Tanaka, J. Am. Ceram. Soc., **60**, 467 (1977).
(48) T.Minami and M. Tanaka, J. Non. Crystalline Solids, **38/39**, 289 (1980).
(49) N.Machida, K.Fujii, and T.Minami, Chem. Lett., 367 (1991).
(50) N.Imanaka, T.Shimizu, and G.Adachi, Solid State Ionics, **62** (1993) 167.
(51) U.V.Varadaraju, K.A.Thomas, B.Sivasankar, and G.V.S.Rao, J. Chem. Soc., Chem. Commun. 814 (1987).
(52) C.Delmas, A.Nadiri, and J.L.Soubeyroux, Solid State Ionics, **28-30**, 419 (1988).
(53) S.Wang and S.Hwu, J. Solid State Chem., **90**, 377 (1991).
(54) Shi-chun Li, Jian-yi Cai, Zu-xiang Lin, Solid State Ionics, **28-31**, 1265 (1988).
(55) D.Petit, Ph.Colomban, G.Collin, and J.P.Boilot, Mater. Res. Bull., **21**, 365-371 (1986).
(56) M.Casciola, U.Costantino, I.G.Krogh Andersen, and E.Krogh Andersen, Solid State Ionics, **37**, 281 (1990).
(57) Y.K.Naganovsky and S.E.Sigaryov, Solid State Communications, **83**, 149 (1922).
(58) Y.K.Naganovsky and S.E.Sigaryov, Solid State Ionics, **50**, 1 (1922).
(59) K.Nomura, S.Ikeda, K.Ito, and H.Einaga, Solid State Ioncis, **61**, 293 (1993).
(60) C.Delmas, R.Olazcuaga, G.Le Felm, and P.Hagenmuller, Mat. Res. Bull., **16**, 285 (1981).
(61) F. d'Yvoire, M.Pintard-Screpel, E.Bretey, and M. de la Rochere, Solid State Ionics, **9/10**, 851 (1983).

Acknowledgment

The author is greatly indebted to Professor Dr. Gin-ya Adachi at the Department of Applied Chemistry, Faculty of Engineering, Osaka University for his continuous guidance and encouragement throughout this work.

The author is also indebted to Professor Dr. Hiroshi Yoneyama and Professor Dr. Kouichi Niihara for their valuable comments and kind suggestions. The author would like to express his sincere thanks to Dr. Nobuhito Imanaka for his helpful discussion in the preparation of the manuscript.

The author would like to express his grateful acknowledgment to Professor Dr. Eisuke Sugimoto at Department of Industrial Chemistry, Niihama National College of Technology, and Associate Professor Dr. Yoshihiko Sadaoka at Department of Applied Chemistry, Ehime University for their helpful discussion and encouragement.

Thanks are given to all the members of Adachi Laboratory and for their help and valuable suggestions.

Finally, the author wishes to thank all his friends, his parents, his wife and his baby for their continuous and hearty encouragement.